EMBEDDED SENSING TEXTILES FOR CORROSION DETECTION

Tonoy Chowdhury, B.S., M.S.

Dissertation Prepared for the Degree of

DOCTOR OF PHILOSOPHY

UNIVERSITY OF NORTH TEXAS

August 2021

APPROVED:

Nandika A. D’Souza, Major Professor
Sheldon Q. Shi, Committee Member
Narendra B. Dahotre, Committee Member
Seifollah Nasrazadani, Committee Member
Ifana Mahbub, Committee Member
Anusha Chilukuri, Committee Member
Kuruvilla John, Chair of the Department of Mechanical Engineering
Hanchen Huang, Dean of the College of Engineering
Victor Prybutok, Dean of the Toulouse Graduate School

Chowdhury, Tonoy. *Embedded Sensing Textiles for Corrosion Detection*. Doctor of Philosophy (Mechanical Engineering), August 2021, 128 pp., 15 tables, 43 figures, numbered chapter references.

Corrosion in underground and submerged steel pipes is a global problem. Coatings serve as an impermeable barrier or a sacrificial element to the transport of corrosive fluids. When this barrier fails, corrosion in the metal initiates. There is a critical need for sensors at the metal/coating interface as an early alert system. Current options utilize metal sensors, leading to accelerating corrosion. In this dissertation, a non-conductive sensor textile as a viable solution was investigated. For this purpose, non-woven zinc (II) oxide-polyvinylidene fluoride (ZnO-PVDF) nanocomposite fiber textiles were prepared in a range of weight fractions (1%, 3%, and 5% ZnO) and placed at the coating/steel interface. Electrochemical impedance spectroscopy (EIS) testing was performed during the immersion of the coated samples to validate the effectiveness of the sensor textile. In the second part of this dissertation, an accelerated thermal cyclic method has been applied to determine sensor's reliability in detecting corrosion under actual service condition. The results suggested that the coating is capable of detecting corrosion under harsh conditions. Moreover, the addition of ZnO decreases the error in sensor textile and improved coating's barrier property. In the next phase, experiments were conducted to detect the type of corrosion (pitting or uniform) underneath the protective coating as it has profound effect on overall performance and durability of the steel pipe. The data suggested that the pitting corrosion drew a lot of current, hence its resistance was significantly low which was tacked by the sensor accurately whereas the uniformly corroded specimens showed almost identical results which portrayed the sensor's ability to detect pitting corrosion.

Copyright 2021

by

Tonoy Chowdhury

ACKNOWLEDGEMENTS

I am highly grateful to my parents Mr. Akhimal Chowdhury and Mrs. Baby Chowdhury for their love and the sacrifices that they made so that I could be where I am today. I would also like to thank my brother Tanmoy Chowdhury and sister Tapati Chowdhury along with other relatives and friends for their continuous support throughout my UNT career.

I express my heartiest gratitude to my wife Priyanka Biswas, without whom the journey could not be finished so smoothly. Thanks for believing in me and staying by my side in this entire adventure.

I especially thank my adviser Dr. Nandika D’Souza for her continuous support, encouragement, and guidance during this research. Thanks to my advisory committee members Dr. Sheldon Q. Shi, Dr. Narendra Dahotre, Seifollah Nasrazadani, Dr. Anusha Chilukuri and Dr. Ifana Mahbub for their valuable suggestions in completing the thesis. In addition, I acknowledge the support that I received from my lab mates specially from Mahan Ghosh, Lee Smith, and Kayode Oluwabunmi.

Finally, I thank Department of Mechanical Engineering for financially supporting me.

TABLE OF CONTENTS

Page

LIST OF TABLES

LIST OF FIGURES

Page

CHAPTER 1

INTRODUCTION

1.1 Introduction

Corrosion is a natural process that transforms a refined metal into a more chemically stable state, such as sulfide, oxide or hydroxide [1]. It is the gradual decomposition of materials (typically metals) as a result of chemical and/or electrochemical reactions with their environment, as shown in Figures 1.1 and 1.2. The conditions are liquids or gases, while such solid-solid reactions can be classified as corrosion in certain circumstances. As a consequence of corrosion, mechanical properties of the metal such as ductility and strength drop significantly which cause disaster. The economic impact of metallic corrosion is in the range of about 5% of gross income of our nation. These costs are associated with both corrosion prevention and the maintenance or replacement because of corrosion reaction [1].

Figure 1.1: Corrosion in the bridge over the years [2]

There are as many as eight forms of corrosion: uniform attack, galvanic corrosion, crevice corrosion, pitting, intergranular corrosion, erosion corrosion, selective leaching, stress corrosion. Among all of these, uniform and pitting corrosion is most common.

Uniform corrosion is a type of electrochemical oxidation that occurs when metals react with oxidants such as oxygen. As shown in Figure 1.2, the electrochemical mechanism is the transition of electrons as a result of a chemical reaction.

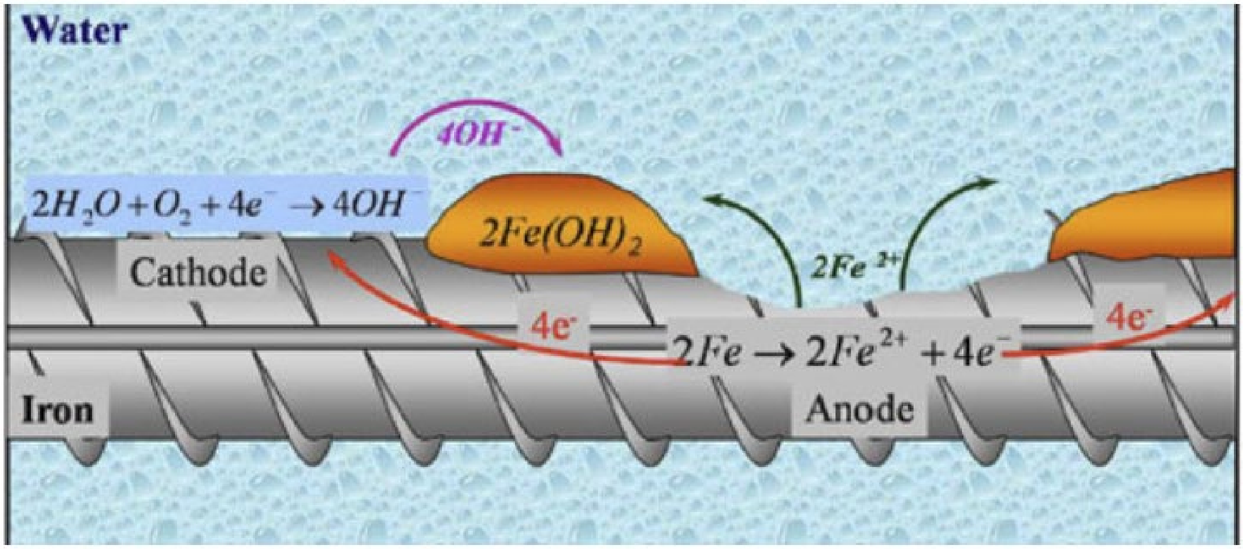

Figure 1.2: Cathodic and anodic area on the surface of carbon steel [3]

The transition of electrons between elements results in two types of reactions: oxidation and reduction. The metal (M) gives up or lacks valence electrons (n) and becomes positively charged during an oxidation reaction. In this case, the metal acts as an anode, and the reaction is referred to as an anodic reaction, as shown by Equation 1.1:

$$M \rightarrow M^{n+} + ne^- \qquad \text{(Eq. 1.1)}$$

For example:

$$Fe \rightarrow Fe^{2+} + 2e^- \qquad \text{(Eq. 1.2)}$$

A reduction reaction occurs when a chemical species accepts a transferred electron and reduces its valence. In the case of a metal, the valence decreases due to electron gain, and this decrease will fully transform the metal from an ionic to a neutral state. This metal is referred to as a cathode, and the reaction is referred to as a cathodic reaction:

$$M^{n+} + ne^{-} \rightarrow M \qquad \text{(Eq. 1.3)}$$

The form of solution to which the metal is exposed determines the reduction reaction. In an acid solution with a high concentration of hydrogen ions (H^+), the ions reduce and hydrogen gas is generated as:

$$2H^{+} + 2e^{-} \rightarrow H_2 \qquad \text{(Eq. 1.4)}$$

The reduction reaction in the acid solution with dissolved oxygen is:

$$O_2 + 4H^{+} + 4e^{-} \rightarrow 2H_2O \qquad \text{(Eq. 1.5)}$$

The reduction reaction in the basic aqueous or neutral solution with dissolved oxygen is:

$$O_2 + 2H_2O + 4e^{-} \rightarrow 4OH^{-} \qquad \text{(Eq. 1.6)}$$

The oxidation or reduction reaction is referred to as a half reaction. Both of them add up to form the complete electrochemical reaction. There is no net charge released by the reaction because all of the electrons produced by oxidation are absorbed by the reduction reaction. For example, rusting iron in water with dissolved oxygen is two-step oxidation of iron. The first move produces Fe^{2+}as:

$$\mathrm{Fe} + \frac{1}{2}O_2 + H_2O \rightarrow Fe^{2+} + 2OH^{-} \rightarrow Fe(OH)_2 \qquad \text{(Eq. 1.7)}$$

The second step produces Fe^{3+}, which is more stable than Fe^{2+} and is more familiar as rust [1,4,5]:

$$2Fe(OH)_2 + \frac{1}{2}O_2 + 2H_2O \rightarrow 2Fe(OH)_3 \qquad \text{(Eq. 1.8)}$$

1.2 Thermodynamics of Corrosion

Corrosion is a natural phenomenon that happens naturally to return the metal to its natural chemical compounds (minerals), which are more solid than the metal itself, as seen in Figure 1.3. Metals occur naturally in nature as minerals. The energy used for metal extraction is released during the electrochemical reaction of corrosion. Since corrosion returns the metal to its initial compound, it is often referred to as reverse extractive metallurgy [5].

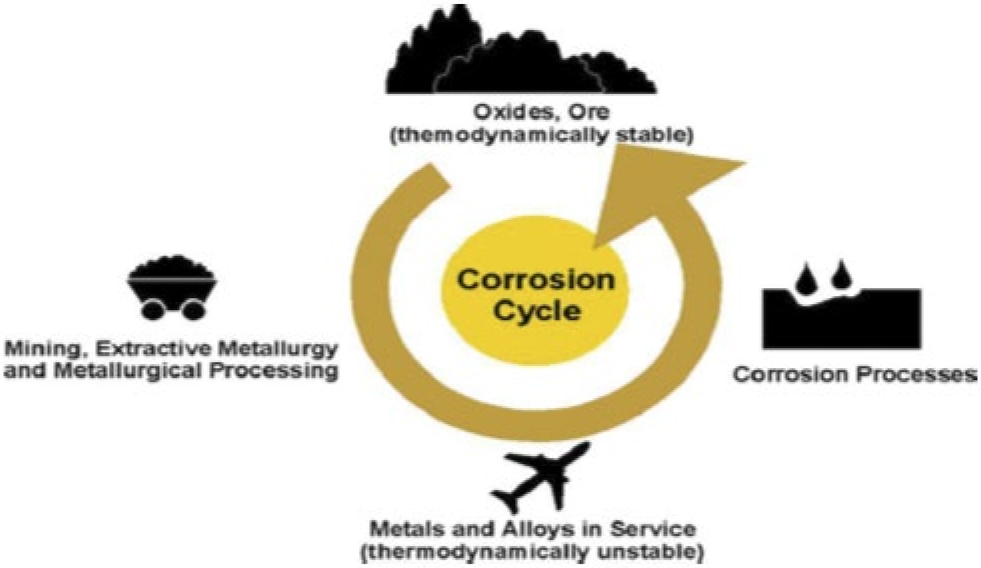

Figure 1.3: Cycle of corrosion [6]

1.3 Corrosion Protection

The protection from uniform oxidizing corrosion can be achieved by four different ways: materials selection, cathodic protection, inhibitors, and coatings [1,4,7]

1.3.1 Materials Selection

If the service conditions have been characterized, the simplest way to avoid corrosion is to use the appropriate materials. As a result, after investigating the chemical, physical, and service environments, the safest time to avoid corrosion is at the design stage. The expense, however, is a challenge for this method. Most anti-corrosive materials, such as silver, nickel, and gold, are very expensive. As a result, incorporating them into steel or other components may be expensive. Their coating is often used inside iron pipes to avoid corrosion and save money, but they often fail due to erosion [7].

1.3.2 Cathodic Protection

Cathodic protection is the most efficient method for reducing or preventing all eight types of corrosion. It requires providing the necessary electrons for the reaction to the metal surface because corrosion of the metal happens in oxidation reactions due to electron loss. This changes the metal from anode to cathode and reverses the reaction from oxidation to reduction [7].

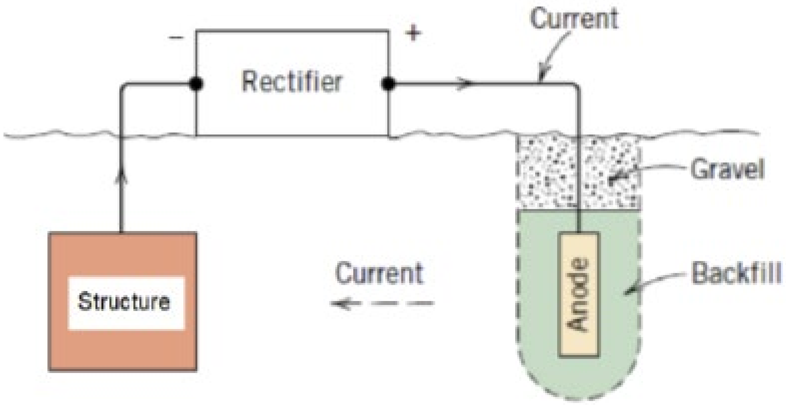

Figure 1.4: Schematic representation for the cathodic protection components [1]

The electrons are supplied by two mechanisms: first, when the metal interacts with a metal which, under the same conditions, is more reactive in order to give electrons and then oxidize the first metal. The sacrificial anode is the second metal. zinc and magnesium are the most frequently used metals to protect carbon steel due to their greater reactivity. The second mechanism, as shown in Figure 1.4, requires the use of direct current dc from an external source to supply the electrons. The completed electrical circuit is formed when the current path from anode to cathode is transferred. The downside of this method is that various components of the system are located at varying distances from the anode, receiving variable currents. Additionally, the effects of the environment on the transferred current produce a non-uniform structure potential. These factors contribute to the system's poor performance [1,4,5].

1.3.3 Inhibitor

It is a blend or material which reduces corrosion when applied in small amounts with the fluid in the pipeline [1]. It forms a thin layer on the metal surface as a result of its interaction with it. This film protects and retards corrosion on the metal surface. Inhibitors include adsorption, hydrogen-evolution toxins, scavengers, oxidizers, and vapor-phase inhibitors. The most often used oxidizer inhibitors are for iron and its alloys. Several examples include chromate, nitrate, and ferric salts [5]. However, they have all harmful effects on the planet [4, 7].

1.3.4 Coating

The most common practice for protecting metal surfaces from corrosion is the application of a protective coatings. Coatings serve as a barrier between metal substrate and surrounding environment to reduce the transport of moisture, water and ionic species to the metal substrate [4]. There are different types of the coatings such as metallic, ceramic, inorganic, and organics [5]. The coatings protect the metal or structure either physically only or physically and chemically. Physically means they provide a physical barrier against the corrosive ions from the environment. All the types of the coating provide a physical barrier at different performance levels. Chemically, the coating reacts with the corrosive ions instead of the metal surface.

The organic coatings are used in wide applications such as pipelines, automobiles, etc. [4]. The main function of the organic coatings is providing a physical barrier against the corroding species. Permanently impermeable organic coating materials are not available yet. Consequently, once a defect is formed, the corrosive species can penetrate the coating easily, resulting in localized corrosion of the metal surface under the coating [1,4]. For example, the Prudhoe Bay oil spill. The oil spill was discovered on March 2, 2006 due to corrosion at a pipeline owned by BP Exploration, Alaska, which costed BP millions of dollars.

1.4 Corrosion Sensor

There is significant concern with corrosion and growing interest in having a corrosion sensor that can alert users to corrosion reaching a critical point enabling the needed intervention to be initiated. Researchers have already found various sensor system which could be very helpful. In general, they classified the sensing system into two broad categories: active and passive [8]. Passive systems are those where the sensing system induces a change in the coating and an external sensor is required to detect it like electrical resistance (ER) sensors. On the other hand, systems are known as active when the sensing system directly outputs a signal such as color change in the coating. A discussion about different types of corrosion sensors is given below:

1.4.1 Optical Sensors

It is simple to track corrosion by observing changes in appearance. Corrosion materials, such as rust on corroded iron, typically cause perceptible differences in material appearance. Unfortunately, human vision's understanding of these appearance often implies a large-scale corrosion. As seen in Figure 1.5, modern optical fiber corrosion sensors (OFCSs) have a much finer detection resolution, which is mostly determined by the wavelength of the light passing through the optical fiber. When opposed to visual inspection, the fine detector resolution allows for corrosion detection at an earlier time. Because of their ability to detect corrosion in complex systems, most OFCSs are used in aircraft corrosion detection, with a few uses in pipelines or building materials [9-13]. The main drawbacks of any kind of optical corrosion sensor are due to their indirect detection methods. Since optical fibers are not electrochemically reactive, detecting corrosion requires converting corrosion-induced changes into optical signals from other media. As a result, corrosion processes are often indistinguishable by these sensors.

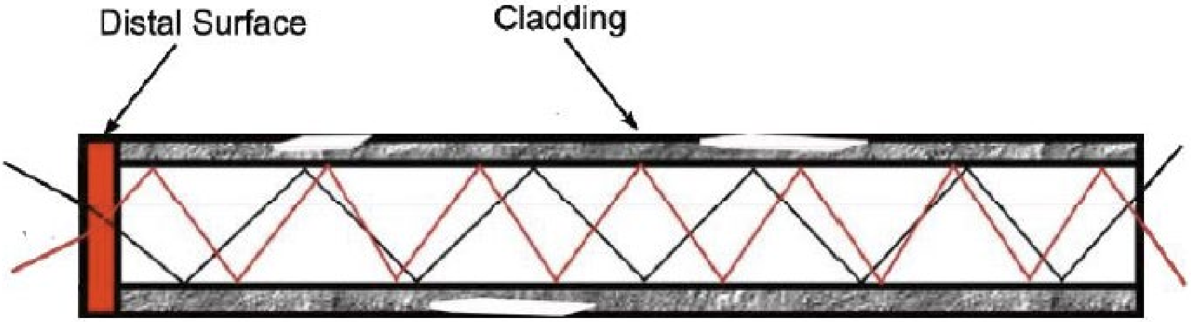

Figure 1.5: Possible sensing sections of an optical-fiber sensor.

OFCSs usually have their cladding replaced by metal layers which will be corroded and cause light-reflectance changes; on the other hand, the distal surface can be coated with chemical-sensitive polymer, combined with imaging devices, to detect corrosive environment [14]

1.4.2 Electromagnetic Sensors

The majority of corrosion sensors depend on two forms of corrosion-induced changes: a) partly exposed electrical circuits and b) the magnetic properties of exposed ferromagnetic materials. These sensors are mostly used in the field of structural engineering. These techniques often employ coils or inductors to produce visible electromagnetic signals, which enables them to be wireless [15,16]. As shown in Figure 1.6, a standard electromagnetic corrosion sensor is composed of two main components: an excitation coil and a receiver coil. The controlled material, either the sensing portion of the sensor or the corroding material, changes the signal produced by the excitation coil in response to the degree and form of corrosion products. A receiver coil receives the altered signal and uses it to associate the signal shift with the corrosion phase.

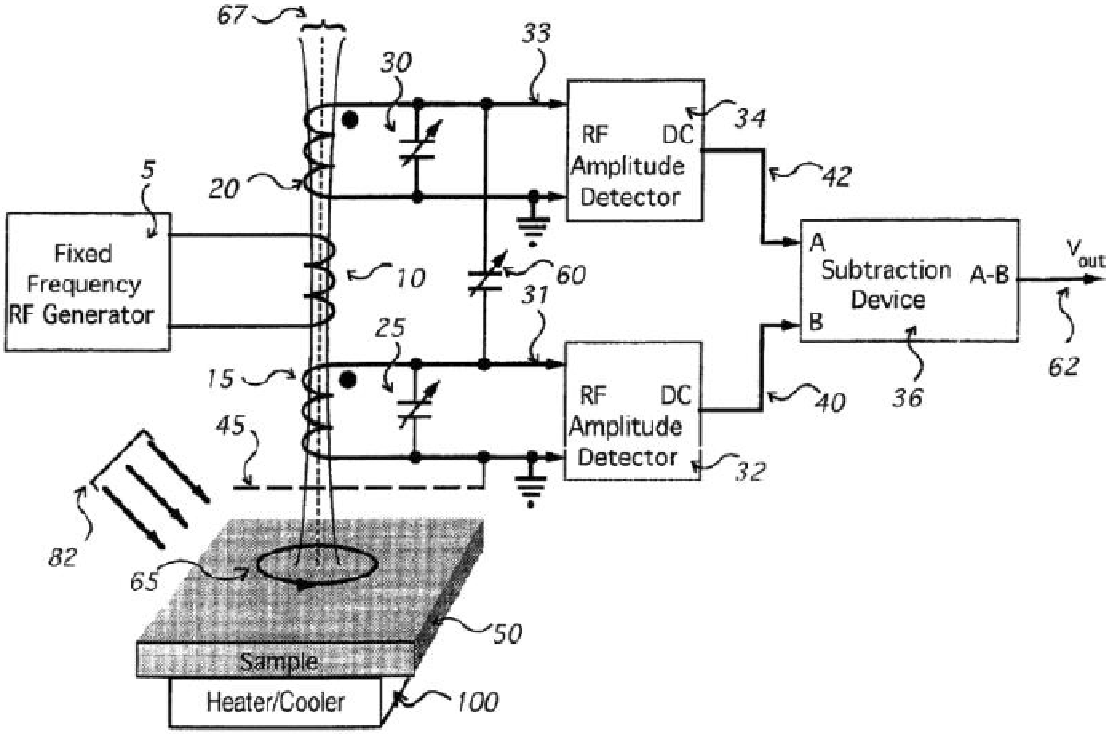

Figure 1.6: An electromagnetic corrosion sensor using eddy current to detect the substrate's conductance change, which indicates the growth oxide film that may be caused by corrosion [17]

1.4.3 Galvanically Coupled Sensors

As shown in Figure 1.7, galvanically coupled sensors are formed by two coupled metal electrodes. Two metal electrodes connected together may be made of two different metals or the same metal. For sensors composed of different metals, the electromotive force produced by their oxidation reactions causes one electrode to be the anode and another electrode to be the cathode. A device such as a zero-resistance ammeter may be used to measure the anodic current (ZRA). However, each single metal electrode contains localized anode/cathode sites.

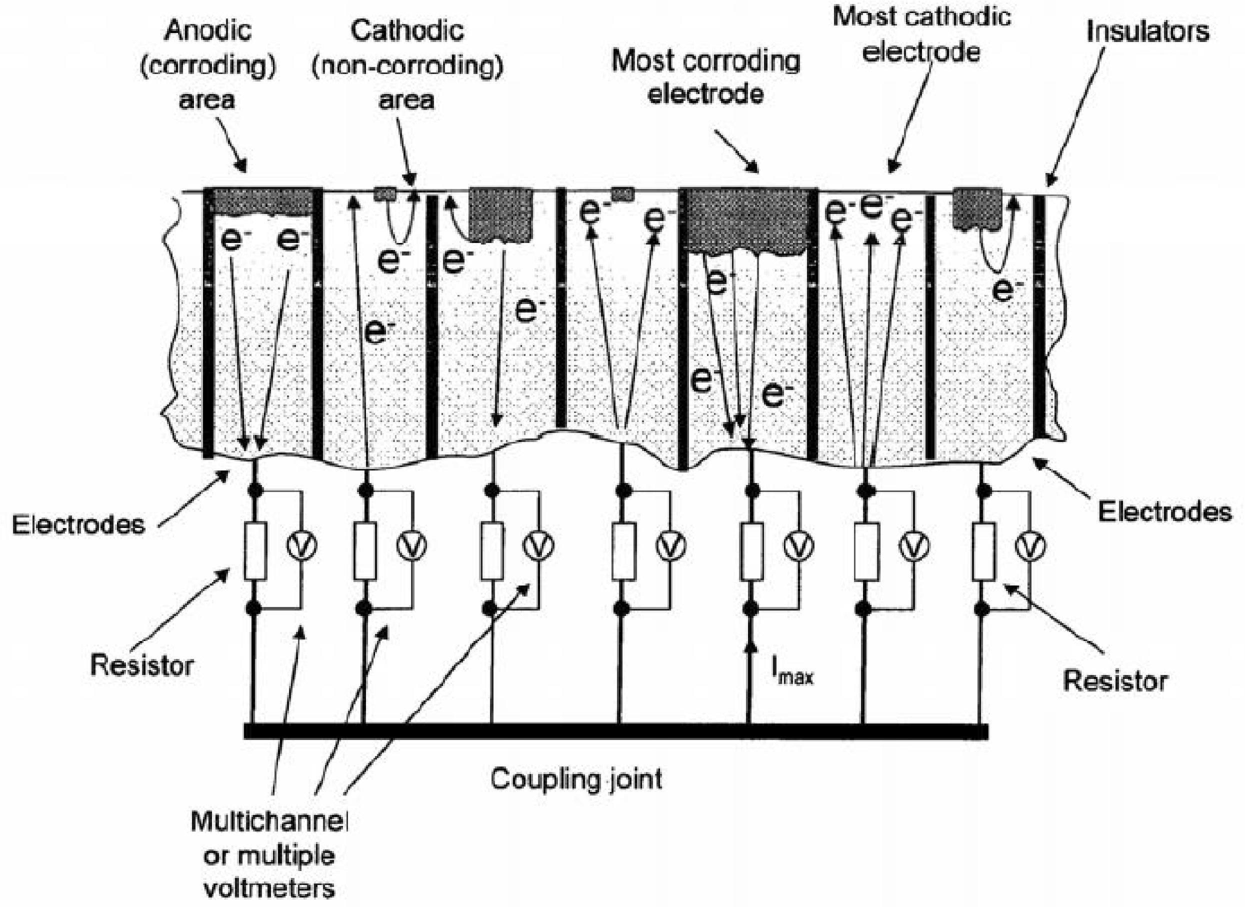

Figure 1.7: A multi-electrode array sensor that measures localized corrosion through exposed electrodes that are insulated from each other and coupled by connection through resistors or zero-resistance ammeters [18]

1.4.4 Other Sensors

W Feng et al. [19] summarized the works of researchers who have reported about using different materials like color changing compounds, dyes, fluorescence materials etc. to detect corrosion. Coatings containing color changing compounds, responding to pH changes that result from corrosion processes have been reported by [20,21]. Some fluorescent coating compounds reach to fluorescent states from non-fluorescent state due to oxidation-reduction reaction caused by corrosion [22-24]. Moreover, releasing of color dyes containing anticorrosive additives from embedded microcapsules filled with dye and additive following mechanical damage of the capsule coating was also reported by few researchers to detect corrosion [25]. Even though these are active sensing systems, their limitations lie in the berried pipe systems where you can't see the change in color. On the contrary, ER systems are too sensitive to detect early stage of corrosion [26]. Other passive sensors such as optical fiber corrosion sensors [9-13] gained much interest in recent years though its corrosion sensing capability was questioned as the optical fiber is electrochemically reactive itself [19].

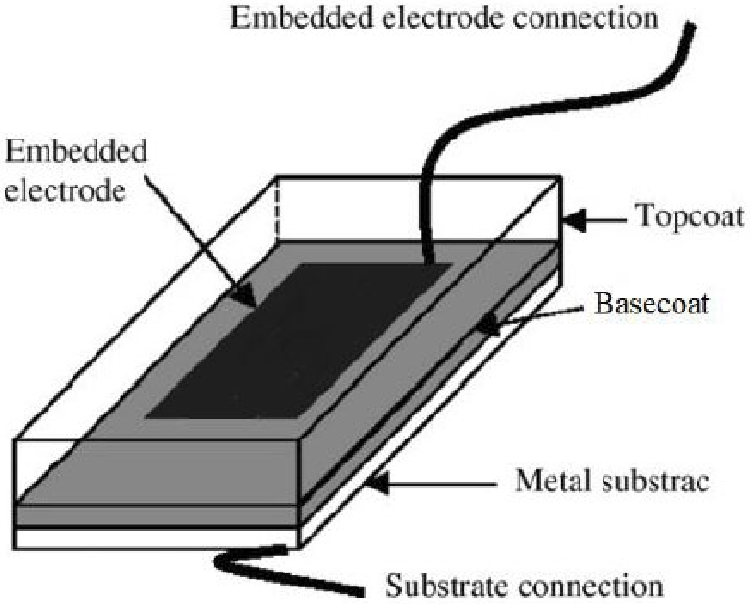

Figure 1.8: Embedded corrosion sensor adaped from [32]

Smart coatings like self-healing coatings are extensively investigated where physical damage in a coating is self-repaired to recover barrier properties before metal corrosion occurs [27-31]. Another type of sensor is embedded sensor which has not been explored explicitly yet. A coating system makes some direct corrosion measurements underneath the coating difficult or even impossible. Embedded corrosion sensors have made these measurements possible through being positioned at or in the interested interfaces or bulk materials. When it is embedded in between two layers of coating, it can sense the corrosion as soon as the corroding particles penetrate the top layer coating as shown in Figure 1.8. That is why embedded sensor could be so interesting.

For buried pipes, both active and passive sensing systems have limits. Active sensing approaches are limited when one deals with subsurface or immersed pipe systems since color change is no longer visible. Passive sensing systems like ER and eddy current testing systems have not been found to be sensitive enough to detect early stages of corrosion [33]. In applications of corrosion, the main reason for inadequate performance of optical fiber sensors has been that the sensor itself was electrochemically reactive [33]. Smart coatings, such as self-healing coatings, where physical damage in a coating is self-repaired to regain barrier properties before metal corrosion occurs have been gaining ground [33-35]. But serious chemical and mechanical limitations of these coatings have been noted [32]. None of these sensors are compatible with real-time corrosion sensing in an environment under any coating systems. Continuous monitoring via embedded sensing is receiving much interest [36]. Kittel et al. deposited a gold and nickel metal layer to measure the impedance of different parts of the coating (i.e. solution + outer layer, inner layer + substrate) [37, 38]. Bierwagen et al. embedded platinum in between two layers of the coating to measure real-time corrosion in their work [39, 40]. A constraint emerges that with a high fraction of sensing elements being metallic, corrosion can be exacerbated from their use. Regardless of the type of sensor, there is a concern with cost in wide area application and measurement of the corrosion response.

1.5 Problem Statement

The problem of the embedded sensor is embedded sensor itself. The comparison between the performance of coatings with and without embedded sensors was done by Hollander et al. [41]. Using metal in the coating has a profound effect on corrosion resistance. Initially, the both coatings didn't show any difference. But as the corrosion started taking place, embedded coating sensor's corrosion rate was higher than the other one. Regardless of the type of sensor, there is a concern with cost in wide area application and measurement of the corrosion.

To overcome the limits of the sensing element being highly conductive and thereby accentuating the corrosion of the pipe, the metal electrode needs to be replaced with a better conductive but non-corrosive electrode. Polyvinylidene fluoride (PVDF) is an extremely non-reactive thermoplastic fluoropolymer formed by the polymerization of vinylidene difluoride. PVDF is a cheap but special plastic that is used in applications that require high purity as well as tolerance to solvents, acids, and hydrocarbons. Normally, PVDF posses 5 different crystal structure such as α, β, γ, δ, and ε. In the bulk state PVDF remains in α crystalline phase which is less electroactive. Hydrogen and fluorine atoms reside on one side of the polymer backbone, resulting a non-zero dipole moment. However, β polymorph is polar and electroactive relevant in context to piezoelectric properties. Electrospun PVDF fiber mesh is a very already known for its energy-harvesting capacity as the α phase of the PVDF is converted into the β phase through the electrospinning process which increases the piezoelectric property [30,31]. In addition to its energy-harvesting property, the fiber can also be used as a corrosion sensor as it changes its resistance from dry state to wet state and can act as a barrier between steel and corrosion species. Few researchers have already started working on fiber-epoxy composites as corrosion coating [42, 43]. This approach encourages us to use PVDF fiber as embedded sensor. Even adding ZnO in glass fiber epoxy composite has increased the corrosion resistance of the coating.

1.6 Scope of this Dissertation

The aim of this project is to examine whether an insulative polymer sensor textile can function as a corrosion sensor. Three questions are examined that demarcate the dissertation from prior work:

1. Are embedded sensor textiles functional in corrosion
2. Is the constituent of the sensor textile via incorporation of nanoparticles vital to improving sensitivity
3. How does the sensor textile perform over time in terms of reliability
4. Can the textile function under different corrosion mechanisms

To answer these questions, the dissertation is organized to first provide a background to constituents of sensor textiles and the current state of knowledge in Chapter 2. In Chapter 3, the role of the nanoparticle filler is established as well as reliability of the sensor is examined over time. In Chapter 4, the use of an accelerated temperature approach for reliability is evaluated using a special cell. In Chapter 5, the effectiveness in discerning pitting versus uniform corrosion is examined.

1.7 Reference

1. W. D. Callister, J.D.G. Rethwisch. Fundamentals of Materials Science and Engineering. 2007.

2. The Engineering Community. Link: https://www.theengineeringcommunity.org/types-and-causes-of-concrete-deterioration/

3. Corrosion of Embedded Metals. https://www.cement.org/learn/concrete-technology/durability/corrosion-of-embedded-materials

4. Jones, D.A. Principles and Prevention of Corrosion, 2nd ed.; 1996.

5. Fontana, M.G. Corrosion engineering; 3rd, Ed. Singapore, 1986.

6. Degrigny, C., HE-Arc CR _ 2012 _ MIFAC projet _ internal report. 2012. Doi: 10.13140/RG.2.1.2368.3447

7. Al-Shenawa, A. Effectiveness Of Fillers For Corrosion Protection of AISI-1018 Steel In Sea Salt Solution, University of North Texas 2017.

8. Cole, I.S. 2 - Smart coatings for corrosion protection: an overview. In Handbook of Smart Coatings for Materials Protection, Makhlouf, A.S.H., Ed. Woodhead Publishing: 2014; https://doi.org/10.1533/9780857096883.1.29pp. 29-55.

9. Leung, K.C.; Wan, T.K.; Chen, L. A Novel Optical Fiber Sensor for Steel Corrosion in Concrete Structures. Sensors 2008, 8, doi:10.3390/s8031960.

10. Cooper, K.R.; Elster, J.; Jones, M.; Kelly, R.G. Optical fiber-based corrosion sensor systems for health monitoring of aging aircraft. In Proceedings of 2001 IEEE Autotestcon Proceedings. IEEE Systems Readiness Technology Conference. (Cat. No.01CH37237), 20-23 Aug. 2001; pp. 847-856.

11. Ahmed, R.; Rifat, A.A.; Yetisen, A.K.; Salem, M.S.; Yun, S.-H.; Butt, H. Optical microring resonator based corrosion sensing. RSC Advances 2016, 6, 56127-56133, doi:10.1039/C6RA11538A.

12. Zhang, N.; Chen, W.; Zheng, X.; Hu, W.; Gao, M. Optical Sensor for Steel Corrosion Monitoring Based on Etched Fiber Bragg Grating Sputtered With Iron Film. IEEE Sensors Journal 2015, 15, 3551-3556, doi:10.1109/JSEN.2015.2393559.

13. Da Silva Marques, R.; Prado, R.A.; Da Costa Antunes, F.P.; De Brito André, S.P.; Ribeiro, R.M.; Frizera-Neto, A.; Pontes, J.M. Corrosion Resistant FBG-Based Quasi-Distributed Sensor for Crude Oil Tank Dynamic Temperature Profile Monitoring. Sensors 2015, 15, doi:10.3390/s151229811.

14. Qi, X.; J Gelling, V. A review of different sensors applied to corrosion detection and monitoring. Recent Patents on Corrosion Science 2011, 1, 1-7.

15. Lynch, J.P.; Law, K.H.; Kiremidjian, A.S.; Kenny, T.; Carryer, E. A wireless modular monitoring system for civil structures. In Proceedings of Proceedings of the 20th International Modal Analysis Conference (IMAC XX), Los Angeles, CA, February; pp. 4-7.

16. Lynch, J.P.; Kotov, N.A.; Loh, K.J. Passive wireless readout mechanisms for nanocomposite thin film sensors. Google Patents: 2013.

17. Ermakov, A.; Hinch, B.J. Three coil apparatus for inductive measurements of conductance. Google Patents: 2002.

18. Yang, L.; Yang, X.S. Measurement of cumulative localized corrosion rate using coupled multielectrode array sensors. Google Patents: 2010.

19. Feng, W.; Patel, S.H.; Young, M.Y.; Zunino Iii, J.L.; Xanthos, M. Smart polymeric coatings—recent advances. Advances in Polymer Technology 2007, 26, 1-13, doi:10.1002/adv.20083.

20. Zhang, J.; Frankel, G.S. Corrosion-Sensing Behavior of an Acrylic-Based Coating System. CORROSION 1999, 55, 957-967, doi:10.5006/1.3283932.

21. Djerahov, L.; Vasileva, P.; Karadjova, I.; Kurakalva, R.M.; Aradhi, K.K. Chitosan film loaded with silver nanoparticles-sorbent for solid phase extraction of Al(III), Cd(II), Cu(II), Co(II), Fe(III), Ni(II), Pb(II) and Zn(II). Carbohyd Polym 2016, 147, 45-52, doi:10.1016/j.carbpol.2016.03.080.

22. Augustyniak, A.; Tsavalas, J.; Ming, W. Early Detection of Steel Corrosion via “Turn-On” Fluorescence in Smart Epoxy Coatings. Acs Appl Mater Inter 2009, 1, 2618-2623, doi:10.1021/am900527s.

23. Sibi, M.P.; Zong, Z. Determination of corrosion on aluminum alloy under protective coatings using fluorescent probes. Progress in Organic Coatings 2003, 47, 8-15, doi:https://doi.org/10.1016/S0300-9440(02)00179-0.

24. Li, S.-m.; Zhang, H.-r.; Liu, J.-h. Preparation and performance of fluorescent sensing coating for monitoring corrosion of Al alloy 2024. Transactions of Nonferrous Metals Society of China 2006, 16, s159-s164, doi:https://doi.org/10.1016/S1003-6326(06)60166-0.

25. Nancy R. Sottos Scott R. White, W.L., Christopher C. Matthews Autonomic damage indication in coatings. 2016.

26. Li, S.; Kim, Y.-G.; Jung, S.; Song, H.-S.; Lee, S.-M. Application of steel thin film electrical resistance sensor for in situ corrosion monitoring. Sensors and

Actuators B: Chemical 2007, 120, 368-377, doi:https://doi.org/10.1016/j.snb.2006.02.029.

27. Qian, H.; Xu, D.; Du, C.; Zhang, D.; Li, X.; Huang, L.; Deng, L.; Tu, Y.; Mol, J.M.C.; Terryn, H.A. Dual-action smart coatings with a self-healing superhydrophobic surface and anti-corrosion properties. Journal of Materials Chemistry A 2017, 5, 2355-2364, doi:10.1039/C6TA10903A.

28. Cui, L.-Y.; Gao, S.-D.; Li, P.-P.; Zeng, R.-C.; Zhang, F.; Li, S.-Q.; Han, E.-H. Corrosion resistance of a self-healing micro-arc oxidation/polymethyltrimethoxysilane composite coating on magnesium alloy AZ31. Corrosion Science 2017, 118, 84-95, doi:https://doi.org/10.1016/j.corsci.2017.01.025.

29. Wei, H.; Wang, Y.; Guo, J.; Shen, N.Z.; Jiang, D.; Zhang, X.; Yan, X.; Zhu, J.; Wang, Q.; Shao, L., et al. Advanced micro/nanocapsules for self-healing smart anticorrosion coatings. Journal of Materials Chemistry A 2015, 3, 469-480, doi:10.1039/C4TA04791E.

30. Behzadnasab, M.; Mirabedini, S.M.; Esfandeh, M.; Farnood, R.R. Evaluation of corrosion performance of a self-healing epoxy-based coating containing linseed oil-filled microcapsules via electrochemical impedance spectroscopy. Progress in Organic Coatings 2017, 105, 212-224, doi:https://doi.org/10.1016/j.porgcoat.2017.01.006.

31. Qian, B.; Michailidis, M.; Bilton, M.; Hobson, T.; Zheng, Z.; Shchukin, D. Tannic complexes coated nanocontainers for controlled release of corrosion inhibitors in self-healing coatings. Electrochimica Acta 2019, 297, 1035-1041, doi:https://doi.org/10.1016/j.electacta.2018.12.062.

32. Su, Q.; Allahar, K.; Bierwagen, G., Embedded electrode electrochemical noise monitoring of the corrosion beneath organic coatings induced by ac–dc–ac conditions. Electrochimica Acta 2008, 53, (6), 2825-2830.

33. G.H. Koch, M.P.H.B., M.G. Thompson, Y.P. Virmani, J.H. Prayer. Corrosion Cost and Preventive Strategies in the United States. Office of Infrastructure Research and Development, FHWA-RD-01-156, Federal Highway Administration (FHWA), Department of Transportation (DOT) 2002-3.

34. Kittel, J.; Celati, N.; Keddam, M.; Takenouti, H. Influence of the coating–substrate interactions on the corrosion protection: characterization by impedance spectroscopy of the inner and outer parts of a coating. Progress in Organic Coatings 2003, 46, 135-147, doi:https://doi.org/10.1016/S0300-9440(02)00221-7.

35. Kittel, J.; Celati, N.; Keddam, M.; Takenouti, H. New methods for the study of organic coatings by EIS: New insights into attached and free films. Progress in Organic Coatings 2001, 41, 93-98, doi:https://doi.org/10.1016/S0300-9440(00)00155-7.

36. Miszczyk, A.; Schauer, T. Electrochemical approach to evaluate the interlayer adhesion of organic coatings. Progress in Organic Coatings 2005, 52, 298-305, doi:https://doi.org/10.1016/j.porgcoat.2004.09.006.

37. Bierwagen, G.P.; Wang, X.; Tallman, D.E. In situ study of coatings using embedded electrodes for ENM measurements. Progress in Organic Coatings 2003, 46, 163-175, doi:https://doi.org/10.1016/S0300-9440(02)00186-8.

38. Su, Q.; Allahar, K.N.; Bierwagen, G.P. Application of embedded sensors in the thermal cycling of organic coatings. Corrosion Science 2008, 50, 2381-2389, doi:https://doi.org/10.1016/j.corsci.2008.06.010.

39. Su, Q.; Allahar, K.; Bierwagen, G. Embedded electrode electrochemical noise monitoring of the corrosion beneath organic coatings induced by ac–dc–ac conditions. Electrochimica Acta 2008, 53, 2825-2830, doi:https://doi.org/10.1016/j.electacta.2007.10.063.

40. Hollaender, J. Rapid assessment of food/package interactions by electrochemical impedance spectroscopy (EIS). Food Additives & Contaminants 1997, 14, 617-626, doi:10.1080/02652039709374574.

41. Hollaender, J.; Ludwig, E.; Hillebrand, S. Assessing protective layers on metal packaging material by electrochemical impedance spectroscopy. In Proceedings of Proceedings of the Fifth International Tinplate Conference, London; pp. 300-315.

42. Wei, B.; Cao, H.; Song, S. Degradation of basalt fibre and glass fibre/epoxy resin composites in seawater. Corrosion Science 2011, 53, 426-431, doi:https://doi.org/10.1016/j.corsci.2010.09.053.

43. Chvalovsky, V.; Mach, L.; Machova, H. Cements containing mineral fibers of high corrosion resistance. Google Patents: 1973.

CHAPTER 2

REVIEW ON POLYMERIC SENSORS

2.1 Introduction

Sensors are used in everyday objects starting from touch sensitive phone and laptop to gas sensing in a toxic environment. With advances in micromachinery and easy-to-use microcontroller platforms, the uses of sensors have expanded beyond the traditional fields of temperature, pressure or pH measurement. Among the various types of sensing materials polymer materials have drown everybody's attention due to its versatile properties. Thereby, researchers have started using polymer materials in sensing applications extensively, so does the global research and development (R&D) on the field of sensors has expanded exponentially in terms of financial investment, the published literature, and the number of active researchers in last few decades. Combining all the literature and compare the value of different polymeric sensors in so many applications has become a challenge especially when the device designers wants to select the right polymer as their sensor. Previously, a number of researchers wrote review articles on polymer based sensors focusing on the field of application of the polymer based sensors and the materials perspective [1-3]. But there is a need for device developers to understand measurement technique, sensitivity, resolution correlated to different material responses and this review addresses these issues.

2.2 Smart Polymeric Materials

Smart materials are the materials which can response to a stimuli. External factors, such as tension, moisture, electric or magnetic fields, light, temperature, pH, or chemical compounds, may dramatically affect one or more properties of this type of materials, which are also often known as intelligent or receptive materials. In the world of sensors, this class of materials are very important as they have the potential to provide response to surrounding environment. Moreover, this effect needs to be repetitive in order to use them as a sensor.

Out of all smart materials, a wide range of polymeric smart materials are developed due their variety of chemical and physical properties. Polymers can be soft or hard, rigid or elastic, insulators or with high electric conductivity, swelling or water repellent, on temperature increase they either melt or harden, and come in all colors and sizes. For these properties, they can adapt to many applications from medicine (replacement organs) through car and airplane manufacturing to construction industry. The last two decades have seen a surge in interest in polymeric materials that can alter their physical and chemical properties reversibly or irreversibly in response to external conditions such as pH, temperature, the interaction of specific ions, light radiation, mechanical forces, magnetic fields, electric fields, and bioactive molecules. Solutions, gels, self-assembled nanoparticles, films, or solids are all examples of smart polymers. At the moment, researchers are looking for polymers with unusual and peculiar properties capable of responding specifically to a given stimulus. Researchers have been attempting to apply previously discovered properties of such materials to more complex problems, such as controlled drug and gene delivery, catalysis, identification and visualization, adaptive coatings, and self-healing materials. Unlike their low molecular weight counterparts, intelligent materials based on polymers show a range of advantages in terms of structural integrity, dispersion in aqueous solutions, biocompatibility, manufacturing ease, and eventual integration with detection systems.

Over the last three decades, global research and development (R&D) in the field of sensors has grown rapidly in terms of financial funding, published literature, and active researchers, with a special emphasis on polymer-based sensors. Smart polymers are used in both highly engineered and everyday materials. They are used to create sensors and actuators such as artificial bodies, hydrogels, and biodegradable packaging, as well as to a large extent in biomedical engineering. A polymer that changes conformation in response to pH changes is one example. This polymer can be used in drug delivery. Another is a humidity-sensitive polymer that is used in self-adaptive wound dressings that control the amount of moisture in and around the wound automatically. Another aspect that contributes to the success of smart polymers is the polymer's ability to combine with other organic and inorganic filler materials such as graphene, ZnO, Fe_2O_3, and $BaTiO_3$, among others. The slow and nonlinear reaction can be observed by using the filler material's properties.

In this chapter, we addressed the fabrication, measuring method, and implementation of various polymeric sensors and devices. Additionally, attention is drawn to the developments and challenges in this area of research, and examples of certain real-time applications are given for a variety of polymer-based sensors, most notably strain sensors, biosensors, piezoelectric sensors, and gas sensors.

2.3 Polymeric Strain Sensor

With the advancement of wearable smart devices for human activity tracking [4-8], body health monitoring [9], artificial muscles and soft robotic skin [10], human computer interfaces [11], and structure health monitoring [12], the need for flexible strain sensors is the. Standard strain sensors, on the other hand, are typically made of metals or inorganic semiconductors, which cannot meet the critical criteria for high-strain sensing capabilities due to their narrow detection range (5 percent) [13-16]. Furthermore, the complex design process and high fabrication cost limit their use and production. Thus, innovative smart versatile strain sensors are in high demand, which polymers and their nanocomposites have met.

2.3.1 Response Mechanism

Polymer based strain sensors are a kind of resistive-type sensor, and their reaction mechanisms are governed by the variations in the conductive networks under strain and stress. To ensure reliable sensing activity, electrically conductive polymers with a filler loading greater than the critical volume fraction of the conductive filler are typically used. Different sensing pathways are usually proposed based on the conductive pathway and the applied strain amplitude. (a) As the strain amplitude is small, the connections between neighboring fillers are not easily destroyed, and the variation of the tunneling distance (the shortest distance between the centers of the adjacent conductive fillers) contributes to the resistance change, resulting in a small sensing signal; (b) when the strain amplitude increases, the tunneling distance of certain tunneling paths becomes longer. Meanwhile, some of the conductive filler's direct links are severed, resulting in the collapse of the entire conductive network. Any of these inevitably cause a greater improvement in resistance than the limited strain amplitude, resulting in a stronger sensing signal [17, 18].

In addition, the relative changes in electrical resistance are most often used to calculate the gauge factor of resistive strain sensors. In general, GF can be written as:

$$GF = ((R - R_0)/R_0)/\varepsilon \qquad \text{(Eq. 2.1)}$$

where R_0 is the initial resistance and R is the resistance of electrically conductive polymer composites at the strain of ε.

2.3.2 Sensing Performance of Electrically Conductive Polymer Composites with Different Conductive Fillers

Researchers have used various kinds of conductive materials with polymers to create conductive polymer composite for strain sensor. Among them carbon black, graphene, CNT and different nanowires are most common. Apart from that hybrid fillers made of inorganic and organic parts are also used in different cases to enhance the sensitivity of the sensor. A description of them is given below:

2.3.3 Organic Fillers: Carbon Black (CB), Graphene and CNT

A nice comparison has been made by Hu and his team where they compared three organic nanofiller and their performance in the polymer matric [19]. All the nano fillers (carbon Black (CB), graphene and CNT) have good-conductivity, these are inexpensive and commercially available nanomaterial and researchers have been made numerous efforts to explore its use in strain sensors [20-23]. The SEM of CB (Fig. 2a) shows that the CB particles are aggregates of several branches, which are useful for the development of efficient conducting networks. The aggregation condition eventually often corresponds to a higher level for percolation. The conduction of the conductive network as a stress sensor is easy to disrupt because of the low interference of the CB component but, after a loading period due to the hysteresis effect of the polymer matrix, certain damaged conductive paths will no longer return to their initial state (Figure 2.1a). As a result, CB-based stress sensors typically show a growing tendency due to their cumulative impact in the initial few cycles. In general, it is classified into low structure

CB, medium CB and high structure CB according to the aggregation status of CB. Several studies to investigate their impact on stress sensing activity have been performed so far [21, 24-26].

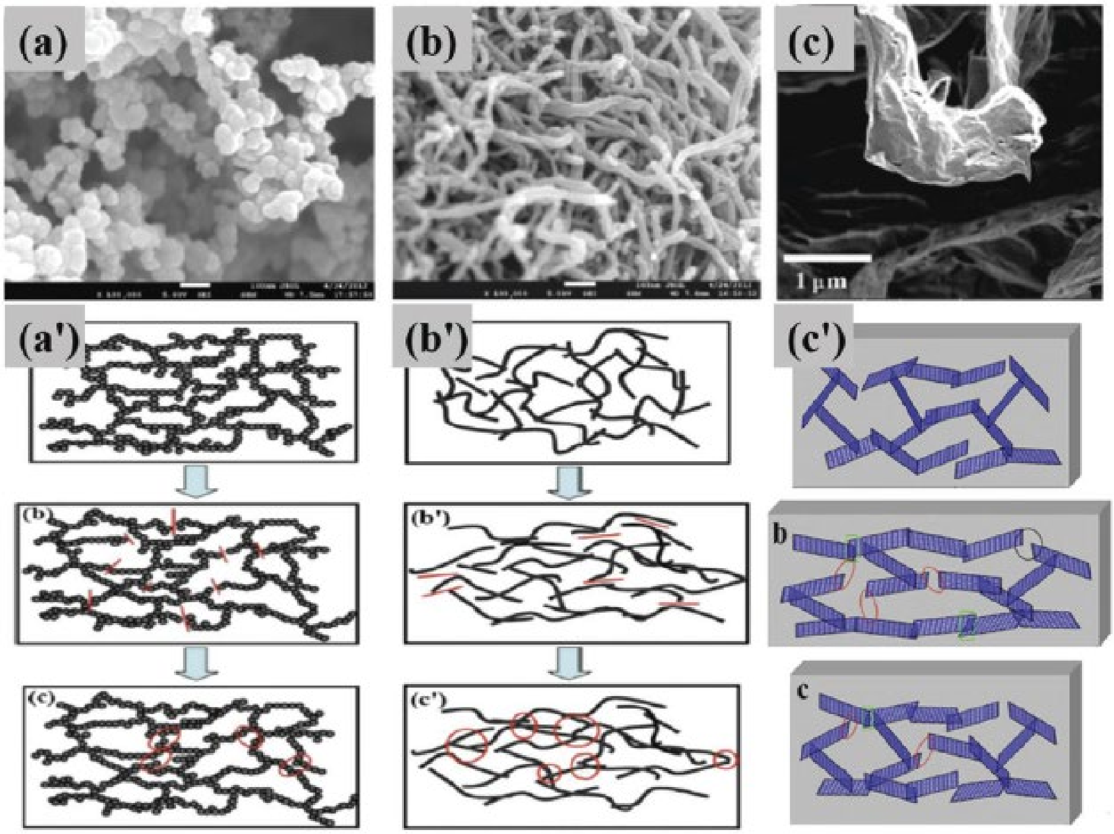

Figure 2.1: SEM image of (a) Carbon black, (b) CNT and (c) graphene; schematic illustration of the change in (a´) Carbon black, (b´) CNT and (c´) graphene conductive network in a single cycle [19].

One-dimensional carbon nanotubes (CNT) are advantageous in electronic devices and sensor applications due to their exceptional electrical conductivity. Electrically conductive polymer composites filled with carbon nanotubes usually have a very low percolation threshold due to the nanoscale diameter and high aspect ratio of the carbon nanotubes. Apart from the size effect, the entangled structure (Figure 2.1b) generated by the van der walls force between individual carbon nanotubes typically imparts a distinct strain-sensing property to electrically conductive polymer composites.

Numerous academic studies have been undertaken recently in order to maximize its application potential [27-29]. For example, using a solution mixture technique, elastomeric TPU/CNT nanocomposites were synthesized with a percolation threshold of approximately 0.35 weight percent [29]. Due to the rearrangement of the entangled conductive networks and the polymer's hysteresis effect, several new conductive networks were formed during the initial several cyclic loadings at 5% strain amplitude (Figure 2.1b´). Following the cyclic loading to stabilize the conductive network, a monotonic strain sensing behavior was found with excellent recoverability and reproducibility.

Recently, 2D graphene (Figure 2.1c) has emerged as the most significant carbon nanomaterial, and considerable effort has been invested to extend its uses in advanced polymer-based nanocomposites. Additionally, graphene has large specific surface area and high-quality crystal lattice, both of which make it an ideal conductive filler [30]. Due to graphene's exceptional electronic transport properties, large specific surface area, and aspect ratio, conductive polymer composites with an ultralow percolation threshold have been successfully obtained. Similar to electrically conductive polymer composites based on carbon black, irreversible resistance was observed due to the hysteresis effect of the TPU molecular chain (Figure 2.1c´). Thus, the conductive polymer composites initially exhibited an increasing trend, but this trend was eventually balanced by the stabilization of the graphene conductive network, resulting in high recoverability and reproducibility. Additionally, it can be concluded that a lower graphene loading, a greater strain amplitude, and a higher strain rate all contribute to the rise in GF (0.78 to 17.7). Encouraged from their results, different researchers used very low percent of graphene different polymers such as TPU, polyurethane acrylate, polystyrene etc. to optimize the sensitivity of the sensor. [31-33].

2.3.4 Inorganic Fillers

The 1D metal nanowires, including silver, copper and gold nanowires, have also shown considerable promise as conductive components for the production of electronic equipment because of their superior electrical conductivity compared to carbon based conductive nanomaterials. Silver nanowires (AgNW) have the highest electrical conductivity (6.3 x 10^7 $S.cm^{-1}$) [34], and are of highest thermal and chemical conductivity among all metallic nanowires. They also have excellent resistance to oxidation and corrosion [35]. Both these make a hotpot for study of silver nanowires mixed conductive composite polymer. Lu et al. successfully prepared a conductive TPU electrospun membrane through vacuum filtration of a AgNW solution, and liquid PDMS was then spin-coated on its surface to form a flexible sandwich structure strain sensor [36]. As a result, it showed excellent repeatability over different strain amplitudes and during cyclic loading there was almost no apparent sensor drift. Furthermore, silver nanowires oxidation in the air is a crucial factor in the longevity of the sensing performance. This analysis showed virtually no conductivity difference when the sensor had been exposed to air for 30 days due to the safety of the sandwich system. Finally, its excellent versatility facilitates the detection of human movements on body parts while its precise and reliable reaction shows that it is suitable for use as motion sensors.

2.3.5 Hybrid Fillers

Synergistic effects in electrically conductive polymer composites packed with organic-inorganic, organic-organic hybrid fillers have been shown to be an important tool for increasing the dispersity of the nanofiller and thus lowering the percolation threshold. Additionally, its dominance at tuning the sensing efficiency of sensors has garnered considerable interest so far [37-44]. The synergistic effects of CNT/graphene nanomaterials in TPU composites showed significant preference in terms of strain sensing [43, 44].

Table 2.1: The reported various electrically conductive polymer composite based strain sensors and their performance collected from [19]

Polymer	Filler	Processing Technique	Measurement Technique	Gauge factor/ Sensing Range (%)	Ref.
PU	carbon black	Layer by layer	Measured the change of resistance with change in strain	39	[4]
Thermoplastic PU	CNT	Diffusion	Resistance vs strain	400%	[45]
Thermoplastic PU	Graphene	Coagulation/hot pressing	Resistance vs strain	17.7	[31]
PU	Ppy	Situ polymerization	Resistance vs strain	100%	[46]
PU	PEDOT:PSS	Fiber wet-spinning	Resistance vs strain	160%	[47]
PDMS	CNT	Cast coating	Resistance vs strain	280%	[48]
PDMS	CNT	Spin coating	Resistance vs strain	62	[11]
PDMS	Graphene	Cast coating	Resistance vs strain	630	[7]
PDMS	Graphene Fabric	Spin coating	Resistance vs strain	1000	[7]
Rubber	Graphene	Solution soaking	Resistance vs strain	35	[49]
Ecoflex	Gold	Contact transfer	Resistance vs strain	70	[8]
SBS	CNT-Ag NP	-	Resistance vs strain	26500	[50]
SBS	Ag-NP	Wet spinning	Resistance vs strain	100%	[51]
POE	Ag-NW	Diffusion process	Resistance vs strain	13920	[27]
PP	CB-CNT	Melting blend and hot compression	Resistance vs strain	3%	[26]
PC	CNT	Electrospinning	Resistance vs strain	16	[52]
PDMS	Gold	-	Resistance vs strain	100%	[53]

2.4 Polymeric Electrochemical Sensor

Conductive polymers (CPs) and conductive polymer nanocomposites (PNCs) have been shown to be superior transducers in electroanalytical sensors due to their morphology diversity and ease of synthesis in comparison to their counterparts [54, 55]. Their distinctive properties include low cost, improved electronic properties, controllable chemical/electrochemical properties, fast electrode kinetics, biocompatibility, and environmental resilience. Considering these properties, in this section we will be reviewing conductive polymers and its nanocomposites in electrochemical sensor application.

2.4.1 Response Mechanism

Electrochemical sensors operate by the diffusion of fluid. Fluid enters the membrane outlet on top of the sensor housing. An electrochemical reaction happens as the gas approaches the working electrode. According to the form of solvent, this reaction is either an oxidation or a reduction, as shown in Figure 2.2. (For instance, carbon monoxide is oxidized to form carbon dioxide, while oxygen is reduced to form water.

In the external circuit, oxidation allows electrons to flow from the working electrode to the counter electrode. Reduced electrons migrate from the counter electrode to the active electrode. Electron flux in any direction generates an electric current equal to the fluid concentration. The external circuit's electrons sense and intensify this current. It then calibrates the output and converts it to engineered systems. PPM (parts per million) readings on the engineered systems have a percentage of the volume of fluid.

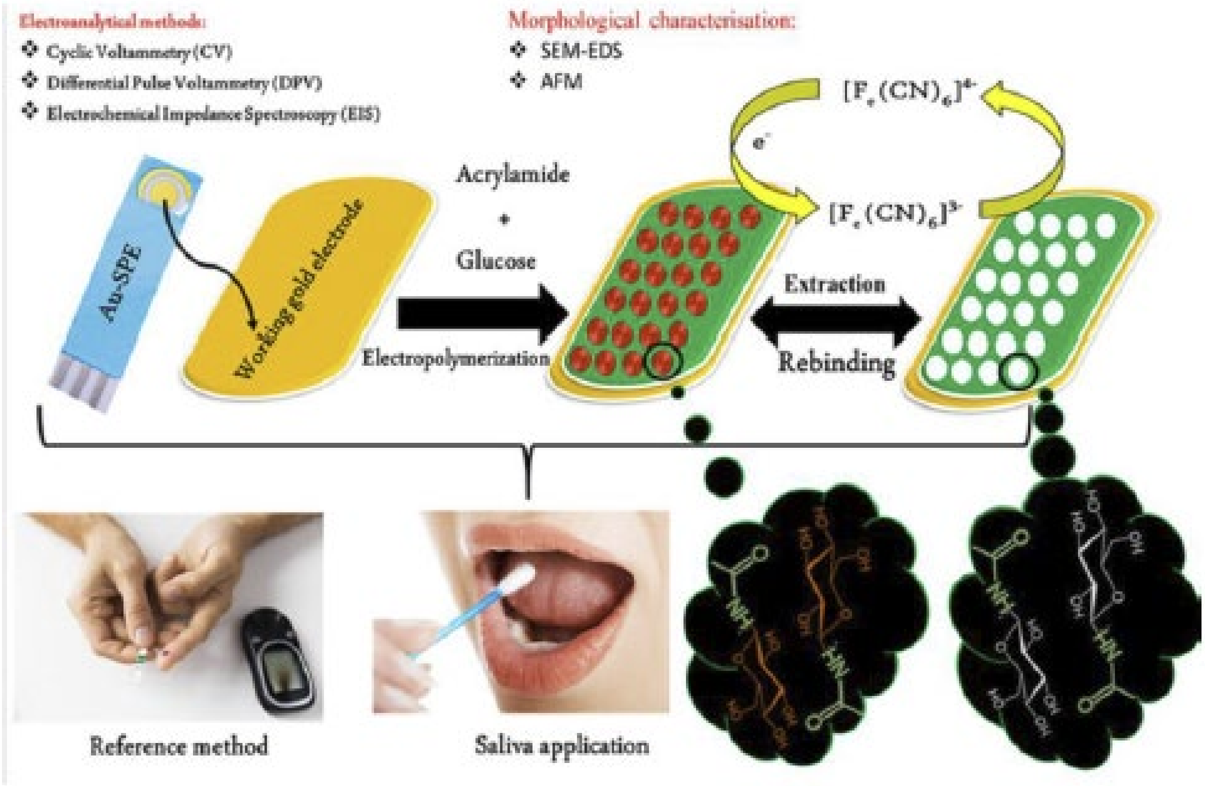

Figure 2.2: Schematic illustration of response mechanism of polymeric electrochemical sensor [56].

2.4.2 Conductive Polymers (CPs) for Electrochemical Sensor

After the CPs have been discovered, they have been extensively studied to develop a diverse array of electrochemical sensors for signal measurement and amplification in a variety of applications, including medical diagnosis, research in the food and pharmaceutical industries, and environmental control of trace metals [57-60]. Conductive polymers exhibit special properties such as light weight, stability, scalability, corrosion resistant, and ease of modification to meet specific requirements, making them attractive alternatives to the products commonly used to fabricate sensors. Conjugated double bonds run around the backbone of these polymers. Due to the closely bound nature of the electrons in a conjugated structure, electron flow may be possible. Each bond incorporates a localized "sigma" bond that contributes to the strength of the chemical bond. Additionally, each double bond comprises delocalized electrons that can pass as charge carriers in the structure, resulting in an intrinsic conductivity of between 10^{10} and 10^5 S.cm^{-1}. Additionally, to achieve electrical conductivity, the conjugated polymers must be doped by adding or subtracting electrons. After doping, electrons in the bonds will "jump" along the polymer chain. An electric current is produced as the electrons pass around the molecule. Chemical modification of the polymer backbone, the quality of the dopant, the amount of doping, and mixing with other polymers can all be used to tune the conductivity of CPs [61].

2.4.3 Conductive Polymer Nanocomposite (PNCs) for Electrochemical Sensor

Pure CAPs had many drawbacks such as high susceptibility, complex toxicity, and interspecies reactivity, which is why they have not yet been approved by the medical community [62]. To overcome the limitations CPs were introduced with different conductive nanomaterials such as CNT, graphene and other inorganic fillers. A description of their performance after adding to CPs are given below:

2.4.4 Organic Fillers: CNT and Graphene

As discussed in previous sections, organic fillers as CNT and graphene has been of great use in terms of conductive sensing applications, these materials showed their resilience in electrochemical sensors as well. Conductive polymer–carbon nanotube nanocomposites have been synthesized with the aim of enhancing the operating characteristics of the resulting sensors in terms of selectivity, reliability, and sensitivity, resulting in a number of important applications. Table 2.2 summarizes some recent sensor designs based on CNT-CP nanocomposites. An electrochemical sensor for the detection of total cholesterol was fabricated using a polypyrrole (PPyox)–multiwalled carbon nanotube (MWCNT)-toluene sulfonic acid nanocomposite deposited on an ITO-coated glass. The same study suggested a method for determining total cholesterol by immobilizing cholesterol oxidase (ChOx) and cholesterol esterase (ChEt) enzymes on a changed electrode surface. Using differential pulse voltammetry (DPV) as a detection tool, this updated sensor demonstrated enhanced biosensing characteristics with high sensitivity with a fast response time of 9 s [63]. Other researchers also used MWCNT-modified glassy carbon electrode (GEC) to detect anticancer drug pemetrexed and antiviral drug acyclovir [64-66]. Few people used carbon paste electrode (CPE) modified with a PEDOT–carbon nanotube (CNT) nanocomposite to detect hydroquinone [67-68]. In all the cases CNT showed excellent performance.

Similar to CNT, 2D graphene has seen considerable growth over the past few years. The fabrication of electrochemical sensors using graphene electrodes is now a common for developing various types of highly sensitive and selective analytical sensors. A PANI-Graphene-GCE-modified sensor used to detect 4-aminophenol (4-AP) [70]. The sensors were of high analytical efficiency with an oxidization limit of $6.5 - 10^{-8}$ M and a maximum sensitivity of 604.2 μAm/M for the oxidation of 4-AP. In the pharmaceutical formulations and biological fluids, researches identified sensors based on the same nanocomposites to measure antimalarial drug artesunate [71]. A PANI-Graphene nanocomposite was electrochemically manufactured on the indium oxide glass plates, followed by immobilization of the enzyme horseradish peroxidase. The subsequent Biosensor demonstrated linearity in artesunate between 0.05 and 0.40 ng mL^{-1} with strong 0.15 mA ng mL^{-1} sensitivity. For the calcium antagonist lercanidipine quantification in pharmaceutical formulations, Jain et al. developed a PANI-Graphene-

GCE dependent sensor. For lercanidipin with correlation coefficients of 0.9998 [72], the procedure was linear over a large concentration spectrum of 5 to 125 ng mL^{-1}. They also stated that an effective sensor using the same nanocomposites as a sensing material is used for the quantification of nitazoxanide [73-75].

2.4.5 MXene

MXene is a new class of materials that has gained a lot of interest since its discovery in 2011. Like graphene, MXene is also a 2D material which is also known as transition metal carbide, nitride or carbonitride. MXene can be produced energetically by selectively etching specific atomic layers (e.g., Al, Si, and Ge) from their parent MAX process in the presence of HF or a combination of strong acid (HCl) and fluoride salt (NaF, LiF and NH4F). MXene has the structural formula $M_{n+1}X_nT_x$, where M represents an early transition metal (such as Ti, V, Zr, or Nb), X represents C and/or N components, and T represents surface functional groups (e.g., –O, OH, and –F). Because of the various atomic layer numbers in the unit cell, n will vary from 1 to 3, resulting in the standard structures M_2XT_x, $M_3X_2T_x$, and $M_4X_3T_x$ [76a]. At the beginning, its use was only limited to energy conversion and storage applications. As the days went by, researchers found its new applications from biosensing to structural composites since it shows excellent mechanical, electrical, and magnetic properties [76b].

As a biosensor, MXene has been used by different researchers with Nafion to detect hemoglobin (Hb) and glucose. $Ti_3C_2T_x$ was first chosen to immobilize hemoglobin (Hb) in a biosensor for detecting nitrites (Nafion/Hb/Ti3C2Tx/GCE). Because of $Ti_3C_2T_x$'s comparatively high conductivity, the Nafion/Hb/$Ti_3C_2T_x$/GCE biosensor has an outstanding biosensor efficiency with an expanded detection range and a lower detection cap. The biosensor's nitrite detection range is increased to 0.5–11 μM, with the lowest detection limit reduced to 0.12 M [76c]. Another researcher discovered that a TiO_2-modified $Ti_3C_2T_x$ nanocomposite synthesized by a hydrothermal method can also be used as the immobilization matrix for hemoglobin in a biosensor (Nafion/Hb/ $Ti_3C_2T_x$ –TiO_2/GCE) capable of rapidly detecting hydrogen peroxide with a reaction time of less than 3 s and a linear range of 0.1 to 380 M [76d]. In order to make MXene have an excellent performance in the enzymatic glucose biosensor, a MXene–Au nanocomposite with a structure similar to that of TiO_2– $Ti_3C_2T_x$ mentioned above is used as the immobilization matrix in a GOx/Au/MXene/Nafion/GC biosensor. The fabricated biosensor shows a wide detection range for the glucose concentration from 0.1 mM to 18 mM, a low detection limit of 5.9 μM, excellent stability and good reproducibility [76e].

2.4.6 Inorganic Fillers

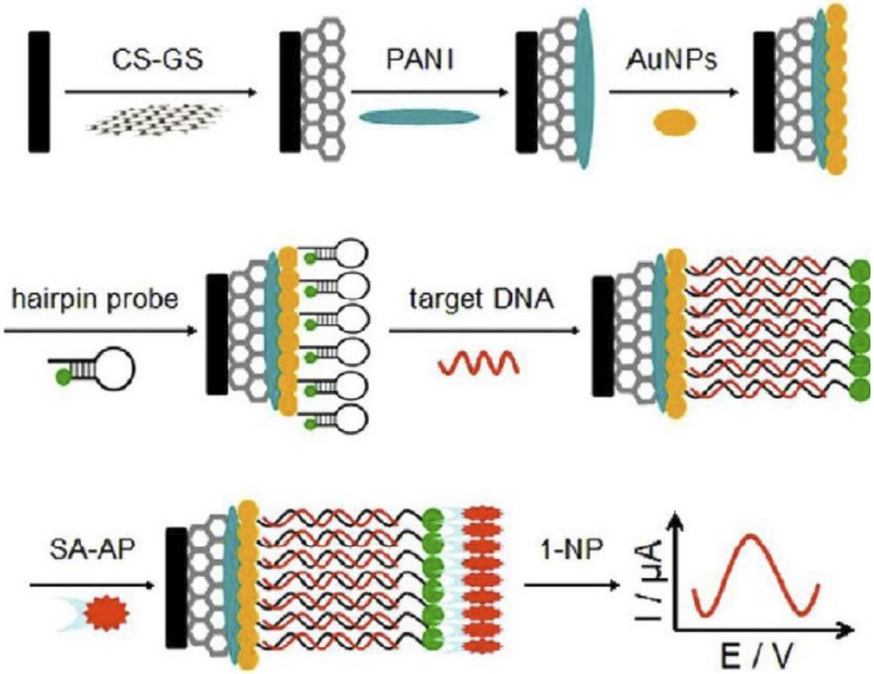

Figure 2.3: Schematic illustration of the electrochemical DNA sensor construction process [77].

Studies on metal and metal oxide nanoparticles as electrochemical sensors have been conducted for several years because of their small size, special chemical, physical, and electronic properties, as well as their capability to produce enhanced and novel sensors [78]. many electrochemical applications were built around the incorporation of metal nanoparticles into matrices a zinc oxide nanoparticle-polyphenon (ZnO-PPN) composite was identified for the study of xanthine in biological samples With enzyme xanthine oxidase, this biosensor showed a significant increase in electrocatalytic activity (EC) against the catalysis of the oxidation of xanthine [79].

A carbon-modified polypyrrole nanofilm was fabricated with Ag nanoparticles for the measurement of H_2O_2 [80]. The changed system displayed a strong reactivity against the drop in the level of H_2O_2, perhaps due to the large amount of surface under normal stress of the nanofilm. They didn't only allow for the binding of Ag but opened up the surface region for water, making it easier for H_2O_2 to react with it. Additionally, a polypyrrole–polyplatinum (Ppy–Pt) voltameter was fabricated to detect H_2O_2. It had an excellent electrochemical activity against H_2O_2, which had previously been seen by Hoffmann et al [81] in alder measurements (the research was suggested by Hoffmann et al using a polyanil–nanoparticle in epinephrine/uric acid measurements). The AuNPs retained their original morphology because PANI made stacking possible. The improved sensor showed considerable electrochemical activity and also demonstrated high stability at the same time, at the same time. A major factor that interferes with identification of EPs and UAs was found to be up to 50-fold in presence of ascorbic acid.

Similarly, PANI was mixed with ZrO_2 and Bi_2O_3 nanoparticles to analyze pramipexole and esomeprazole [72-83]. A PANI-ZnO nanocomposite was used to fabricate an electrochemical sensor for the study of betahistine hydrochloride and PANI-AgNPs nanocomposite was used as DNA sensor [77, 84].

Table 2.2: The reported various electrically conductive polymer composite based electrochemical sensors and their performance collecyed from [85]

Polymer	Filler	Sensing Element	Sensing Technique	Detection Limit	Ref.
Polypyrrole	ZnO	xanthine	Amperometry (changes current when comes in contact with analyte)	0.8 µM	[79]
PANI	Gold NP	Epinephrine	Square wave voltammetry (changes voltage when comes in contact with analyte)	8 × 10−8 mol/L	[82]
Polypyrrole	Ag	Hydrogen peroxide	Amperometry	0.57 µM	[80]
PANI	ZrO_2	Esomeprazole	Square wave voltammetry	97.21 ng /mL	[72]
PVP	Au–Graphene	Butylated hydroxyanisole	Linear sweep voltammetry	0.04 µM	[86]
Polypyrrole	MWCNT	Pemetrexed	Adsorptive stripping differential pulse voltammetry	3.28 X 10-8 M	[86]
poly(p-phenylenediamine)	Fe_3O_4	Hydrogen peroxide	Amperometry	0.21 µM	[87]
PANI-PVP	Graphene	Cholesterol	Amperometry	1.0 µM	[88]
Polypyrrole	MWCNT	Cholesterol	Differential pulse voltammetry	0.04 mM/L	[63]
PANI	Bi_2O_3	Pramipexole	SWV	1.10 µg/mL	[83]
PANI	ZnO	Betahistine hydrochloride	SWV	19.57 µg /mL	[84]
PANI	TiO_2	Glucose	DPV	0.5 µM	[89]
PANI	$NiCo_2O_4$	Glucose	Amperometry	0.3833 µM	[90]
PANI	Graphite	4-aminophenol	DPV	6.5 × 10−8M	[70]

2.5 Piezoelectric Polymers and Sensors

Piezoelectric sensors are critical for producing integrated piezoelectric devices.

Typically, piezoelectric materials with high elastic modulus like quartz has high performance, but they are hard and brittle for which limits there use where flexibility is required. With advances in fabrication techniques such as laminate, dice, and cut, polymers can effectively fill this void. Additionally, the synthesis of various nanostructured composites of piezoelectric ceramics, such as ZnO, $BaTiO_3$, and PZT, allowed the conception of appealing custom-made applications, such as nanogenerators and self-powered sensors. Thus, polymers are the best materials for fabricating piezoelectric films/substrates, as the manufacturing processes are straightforward and less costly. We have discussed about the materials, fabrication techniques, and applications of piezoelectric polymers and sensors in this section.

2.5.1 Piezoelectricity

Piezoelectric materials generate energy when mechanical stress is applied to them, and mechanical strain occurs when an electrical field is applied to them. Since Piere and Jacque Curie reported the direct piezoelectric effect in 1880 and Lippmann reported the converse piezoelectric effect in 1881, no major advances were made until the 1950s, when PZT and $BaTiO_3$ were discovered. Jaffe et al. found piezoelectric ceramics in 1971. The use of piezoelectric materials in various applications then increased.

2.5.2 The Piezoelectric Materials

Piezoelectricity can be found in approximately one third of the materials present on the planet [91]. Despite the fact that a vast range of materials exhibit this property, only a handful of them have found practical applications in research. The piezoelectric materials are roughly defined as follows: [92]:

1. Single crystals: Quartz, $LiNbO_3$, Lithium Tantalate ($LiTaO_3$),
2. Poly crystalline materials: $BaTiO_3$, $PbTiO_3$, Lead Zirconate($PbZrO_3$),
3. Polymers: PVDF, Poly (vinylidene diflouride- trifluoro ethylene) P(VDF-TrFE), Polymer-Ceramic composites.

Polymers and their composites are the best options for producing piezoelectric films/substrates because the manufacturing methods are easy, low cost, and use low temperature and existing micro fabrication techniques.

2.5.3 Piezoelectric Polymers

The topology and dipole moment of piezoelectric polymers can be used to classify them into bulk polymers, polymer composites, and voided charged polymers. Piezoelectric polymer composites are produced by combining piezoelectric ceramic nano particles with polymers such as PVDF, PDMS, and PP. The piezoelectric effect in these materials is primarily provided by piezoelectric ceramic particles, while polymers add versatility to the composite. A description these materials are given below:

2.5.4 Bulk Polymers

Polymers are classified into two types based on their molecular structure: semi-crystalline and amorphous. Semicrystalline structures are made up of uniformly oriented microscopic crystals scattered within an amorphous mass, rather than a single crystal structure. In order to cause crystalline phase transitions, mechanical orientation, thermal annealing, and high voltage treatment can be used. Stretching the polymer significantly aids in aligning the amorphous strands in the film plane and enables uniform rotation of the crystallites by an electric field [93]. This group includes PVDF and its copolymers, Polyamides, and Paralyne-C. PVDF is a special polymer that comes in a variety of crystalline shapes, each of which has a high piezoelectric effect. PVDF's process material is being improved with special attention. Researchers attempted to increase phase content in PVDF using a phase inversion technique and temperature control [94]. Poling is needed in semicrystalline materials to reorient the crystallites and align the molecular dipoles in order to enhance the piezoelectric effect. In polymers, the presence of an applied electrical field induces the equivalent center of charge displacement to induce a difference of polarization, as it does in piezoelectric inorganic materials.

Amorphous is another class of bulk polymer, which lacks long-range order to sustain the piezoelectric effect. This group includes non-crystalline materials such as Polyimide and PVDC. Piezoelectricity of amorphous polymers is heavily influenced by molecular dipole orientation which could be achived by poling of the materials at high votage. Piezoelectric micro-electromechanical systems (MEMS) resonant sensors are made of bulk polymer and used in a variety of sensing applications, such as tissue engineering, DNA hybridization, protein-ligand interactions, and immunosensors. Changes in resonant frequencies of piezoelectric polymers like PVDF are used in structural health control applications [95].

2.5.5 Piezoelectric Composites

A ceramic/polymer composite is a substance composed of ceramic particles dispersed within a polymer matrix [96]. Polymer’s mechanical properties allow them to be used in applications where piezoelectric ceramic crystals are ineffective, such as flexible and wearable electronics. They have a much higher piezoelectric stress constant, g, than ceramics, making them superior sensors [97]. A typical ceramic material is composed of a metal, a non-metal, or a metalloid that is bonded by ionic or covalent interactions. Ceramic materials are common due to their high mechanical strength, thermal and chemical resilience, elastic modulus, and resistance to wear. In polymer nanocomposites, micro and nanoscale piezoelectric ceramic particles such as $BaTiO_3$, PZT, and ZnO are used mostly. Materials such as PDMS, SU8, and PVC lack inherent piezoelectricity, they can be combined with piezoelectric materials such as $BaTiO_3$ and PZT due to their low stiffness coefficient, low acoustic impedance, and thermal and chemical stability. Composite materials are ideal options for mechanical stability combined with a piezoelectric effect at a reasonable cost. A different kind of composite can be created by combining piezoelectric polymers such as PVDF and P(VDF-TrFE) with piezoelectric ceramics such as $BaTiO_3$, PZT, and ZnO. The piezoelectric effect of the polymer is enhanced further by the incorporation of piezoelectric ceramic particles in this case. These functionalized composites are well-suited for nano-scale energy generation and bioimedical applications. Piezocomposites, such as PZT/polyurethane, contribute significantly to ultrasonic transducers by enabling complex shapes for concentrating acoustic beams and low crosstalk without cutting the transducer [98].

2.5.6 Voided Charged Polymers (VCP)

VCPs, also known as cellular polymers, are another notable application of polymer thin films. They have the ability to have a higher piezoelectric constant than piezoelectric ceramics. Electric fields are used to ionize gas molecules in thin films. This accelerates and implants opposite charges on either side of the voids, creating internal dipoles. Any deformation of the void will cause the material to exhibit a piezoelectric effect. The piezoelectric coefficient is determined by the density, form of the void, the type, and pressure of the gas [99]. G. Dreyfus and J. Lewiner's pioneering work established all of the necessary ingredients for piezo- and pyroelectricity in VCPs, including a nonuniform charge distribution, nonuniform tension, and an appropriate coupling between the two layers. These variables have a direct effect on the net dipole moment produced and the charge distribution on either side of the polymer's voids. Polymers used in VCPs must have voids similar to foam and be electrically secure in order to trap and retain electrical charges. Charge trapping may occur between electronegative groups on the chain, between cages of neighboring molecules, or at the interfaces between crystallites and their amorphous surroundings. The piezoelectric coefficient in VCPs can be varied in response to the frequency of the applied electrical field, resulting in two distinct piezoelectric coefficients, respectively quasistatic and dynamic [100, 101]. Due to their low density, high stability, and almost random structure, VCPs are extremely well suited for tracking movement in biomedical applications, such as respiration motions in laboratory animals, human respiration detectors, and dynamic-force tests on the limbs of running dogs [102].

2.5.7 Fabrication Technique to Enhance Piezoelectric Effect

Addition of copolymer into a polymer is viable option for enhancing piezoelectric effect such as adding trifluoroethylene (TrFE) units to PVDF. Semicrystalline polymers like P(VDF-TrFE) have excellent piezoelectric property along and ferroelectricity. The primary crystalline phases are α and β [PVDF has five crystal phases, with phase α and β being the primary]. The α cooling process becoming the most stable after cooling from melt. However, β polymorph is polar and electroactive relevant in context to piezoelectric properties. Hydrogen and fluorine atoms reside on one side of the polymer backbone, resulting in trans-symm movement. PVDF-TrFE copolymer is made by binding trifluoride compounds to polyvinyl difluoride. The piezoelectric effect of PVDF-TrFE copolymer is activated by the β form, resulting in direct crystallization of the all-trans chain. However, with the addition of a third fluorine atom per repeat element, the dipole moment of the PVDF.

Solvent casting is a straightforward method that involves combining and stirring under high heat to create thin films. For instance, PVDF dissolved in solvents such as DMA or DMF is poured into a glass mold to achieve the desired shape and size before being heated further in an oven. Spin coating is a commonly used technique for obtaining PVDF thin films.

Nano fibers made by electrospinning polymers are becoming increasingly common due to their wide variety of properties and applications. In terms of dielectric and piezoelectric constants, PVDF nanofibers have outperformed filled composites [104]. Many groups are working on electro spun PVDF fibers [105] because electrospinning induces β phase in PVDF through the application of high electric voltage.

Stretching the polymer effectively aligns the amorphous strands in the film in the planar direction, making uniform rotation of crystallites by an electric field easier later on [106]. If the stretching is uniaxial or biaxial determines the electrical and mechanical properties (sensing direction). Stretching causes the polymer chains to orient in a certain direction, resulting in orthotropic content in the piezoelectric sense [107]. Stretching thereby increases piezoelectricity.

At high temperatures, dipole moments may be aligned using a high electric field (poling). It results in the choice of such domain states and preserves the material's macroscopic anisotropy. To obtain stable material properties, the poling field must be greater than the coercive field. Since certain materials have dipole moments “frozen” in the matrix, higher poling temperatures make for better domain wall mobility and poling. The poling temperature can not be higher than the Curie temperature (T_C), which is the boundary for the presence of dipole moments and ferroelectricity. The applied electric fields are usually of the range of 50 MV/m, which is necessary to influence crystalline orientation.

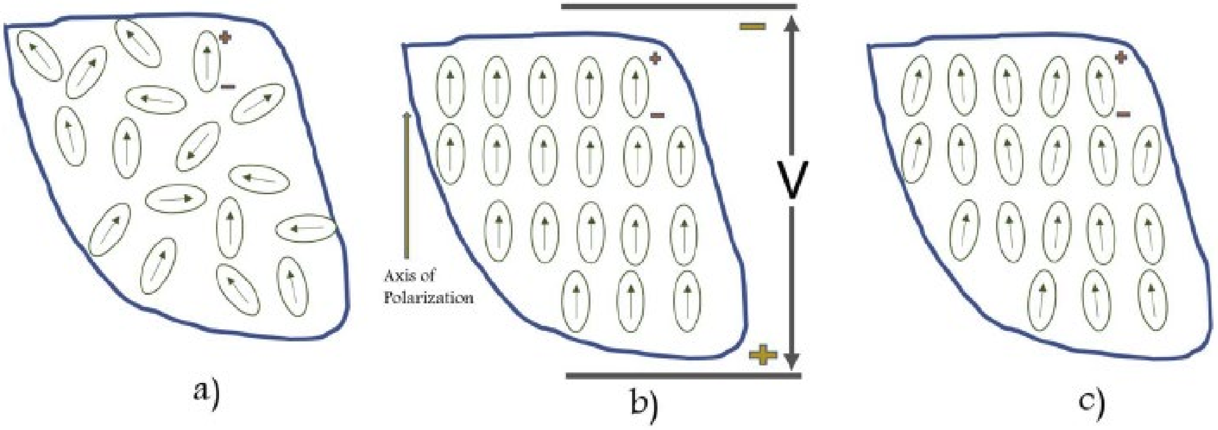

Figure 2.4: Poling process: (a) prior to polarization polar domains are oriented randomly; (b) a very large DC electric field is used for polarization; (c) after the DC field is removed, the remnant polarization remains [93].

Due to the polymers' low stiffness and durability, researchers are increasingly turning to piezoelectric ceramics as a filler material for custom applications such as sensors and actuators. The majority of these filler materials are piezoelectric ceramics such as $BaTiO_3$, PZT, PMN-PT. PZT and lead excluding nanoparticles like ZnO, $LiNbO_3$, $KNaLiNbO_3$, and h-ZnO [108-110] which are environment friendly. These nanoparticles have been extensively investigated in combination with polymers such as PDMS, PVDF, epoxies, and resins due to their high piezoelectric efficiency as discussed in previous section 2.5.5.

Table 2.3: The reported various piezoelectric polymer composite and their performance collected from [93]

Polymer	Filler	d_{33}	Application	Ref.
PVDF	N/A	49.6 pm/V	Actuators and Energy Harvesting	[94]
PET	Aluminum Nitride	0.7 pC/N	Measuring human pulse	[111]
PDMS	PZT	25 C/N	Tactile sensors	[112]
PVDF	$BaTiO_3$	61 pC/N	Actuators and Energy Harvesting	[113]
PDMS	-	350 pC/N	-	[114]
Poly Propylene	$CaCO_3$	250 pC/N	-	[115]
liquid crystalline resin	PZT	g33 = 48 mV-m/N	Pressure Sensors	[112]
P(VDF-HFP)	ZnO	15.2 pC/N	Tiny human activity sensor	[116]
PVC	$BaTiO_3$ nanowires	13.7 pC/N	Finger motion sensor	[117]
PDMS	ZnO	30 pm/V	Soft touch applications	[109]
PVDF	CNT	54pm/V	Actuators and Energy Harvesting	[118]
PDMS	-	47.6 pm/V	Tactile, pressure and acoustic sensors	[110]
PDMS	$KNLiNbO_3$	17 pC/N	Wireless sensors and biodiagnostics.	[108]
Polyetherimide	$PbNO_3$	7.2 pC/N	Structural health monitoring	[108]
ABS	-	70 pC/N	Water and air coupled transducers	[119]
Paylene-C films	-	2 pC/N	BioMEMS	[105]
PPX	-	200 pC/N	BioMEMS	[120]

2.6 Reference

1. Adhikari, B.; Majumdar, S., Polymers in sensor applications. Progress in polymer science 2004, 29, (7), 699-766.

2. Harsányi, G., Polymer films in sensor applications: a review of present uses and future possibilities. Sensor Review 2000.

3. Cichosz, S.; Masek, A.; Zaborski, M., Polymer-based sensors: A review. Polymer testing 2018, 67, 342-348.

4. Wu, X.; Han, Y.; Zhang, X.; Lu, C., Highly sensitive, stretchable, and wash-durable strain sensor based on ultrathin conductive layer@ polyurethane yarn for tiny motion monitoring. ACS applied materials & interfaces 2016, 8, (15), 9936-9945.

5. Park, J. J.; Hyun, W. J.; Mun, S. C.; Park, Y. T.; Park, O. O., Highly stretchable and wearable graphene strain sensors with controllable sensitivity for human motion monitoring. ACS applied materials & interfaces 2015, 7, (11), 6317-6324.

6. Park, S. J.; Kim, J.; Chu, M.; Khine, M., Highly flexible wrinkled carbon nanotube thin film strain sensor to monitor human movement. Advanced Materials Technologies 2016, 1, (5), 1600053.

7. Wang, Y.; Wang, L.; Yang, T.; Li, X.; Zang, X.; Zhu, M.; Wang, K.; Wu, D.; Zhu, H., Wearable and highly sensitive graphene strain sensors for human motion monitoring. Advanced Functional Materials 2014, 24, (29), 4666-4670.

8. Lim, G.-H.; Lee, N.-E.; Lim, B., Highly sensitive, tunable, and durable gold nanosheet strain sensors for human motion detection. Journal of Materials Chemistry C 2016, 4, (24), 5642-5647.

9. Pegan, J. D.; Zhang, J.; Chu, M.; Nguyen, T.; Park, S.-J.; Paul, A.; Kim, J.; Bachman, M.; Khine, M., Skin-mountable stretch sensor for wearable health monitoring. Nanoscale 2016, 8, (39), 17295-17303.

10. Zha, J. W.; Huang, W.; Wang, S. J.; Zhang, D. L.; Li, R. K.; Dang, Z. M., Difunctional graphene–Fe3O4 hybrid Nanosheet/polydimethylsiloxane nanocomposites with high positive Piezoresistive and Superparamagnetism properties as flexible touch sensors. Advanced Materials Interfaces 2016, 3, (1), 1500418.

11. Roh, E.; Hwang, B.-U.; Kim, D.; Kim, B.-Y.; Lee, N.-E., Stretchable, transparent, ultrasensitive, and patchable strain sensor for human–machine interfaces comprising a nanohybrid of carbon nanotubes and conductive elastomers. ACS nano 2015, 9, (6), 6252-6261.

12. Yi, L.; Jiao, W.; Wu, K.; Qian, L.; Yu, X.; Xia, Q.; Mao, K.; Yuan, S.; Wang, S.; Jiang, Y., Nanoparticle monolayer-based flexible strain gauge with ultrafast dynamic response for acoustic vibration detection. Nano Research 2015, 8, (9), 2978-2987.

13. Yan, C.; Wang, J.; Kang, W.; Cui, M.; Wang, X.; Foo, C. Y.; Chee, K. J.; Lee, P. S., Highly stretchable piezoresistive graphene–nanocellulose nanopaper for strain sensors. Advanced materials 2014, 26, (13), 2022-2027.

14. Tang, Y.; Zhao, Z.; Hu, H.; Liu, Y.; Wang, X.; Zhou, S.; Qiu, J., Highly stretchable and ultrasensitive strain sensor based on reduced graphene oxide microtubes–elastomer composite. ACS applied materials & interfaces 2015, 7, (49), 27432-27439.

15. Du, H.; Zhao, C. X.; Lin, J.; Guo, J.; Wang, B.; Hu, Z.; Shao, Q.; Pan, D.; Wujcik, E. K.; Guo, Z., Carbon nanomaterials in direct liquid fuel cells. The Chemical Record 2018, 18, (9), 1365-1372.

16. Zhang, L.; Qin, M.; Yu, W.; Zhang, Q.; Xie, H.; Sun, Z.; Shao, Q.; Guo, X.; Hao, L.; Zheng, Y., Heterostructured TiO2/WO3 nanocomposites for photocatalytic degradation of toluene under visible light. Journal of the Electrochemical Society 2017, 164, (14), H1086.

17. Oskouyi, A. B.; Sundararaj, U.; Mertiny, P., Tunneling conductivity and piezoresistivity of composites containing randomly dispersed conductive nano-platelets. Materials 2014, 7, (4), 2501-2521.

18. Luo, W.; Wu, T.; Chen, B.; Liang, M.; Zou, H., Highly stretchable conductors based on expanded graphite macroconfined in tubular rubber. ACS applied materials & interfaces 2017, 9, (49), 43239-43249.

19. Liu, H.; Li, Q.; Zhang, S.; Yin, R.; Liu, X.; He, Y.; Dai, K.; Shan, C.; Guo, J.; Liu, C., Electrically conductive polymer composites for smart flexible strain sensors: a critical review. Journal of Materials Chemistry C 2018, 6, (45), 12121-12141.

20. Qu, Y.; Dai, K.; Zhao, J.; Zheng, G.; Liu, C.; Chen, J.; Shen, C., The strain-sensing behaviors of carbon black/polypropylene and carbon nanotubes/polypropylene conductive composites prepared by the vacuum-assisted hot compression. Colloid and Polymer Science 2014, 292, (4), 945-951.

21. Yazdani, H.; Hatami, K.; Khosravi, E.; Harper, K.; Grady, B. P., Strain-sensitive conductivity of carbon black-filled PVC composites subjected to cyclic loading. Carbon 2014, 79, 393-405.

22. Zheng, S.; Deng, J.; Yang, L.; Ren, D.; Huang, S.; Yang, W.; Liu, Z.; Yang, M., Investigation on the piezoresistive behavior of high-density polyethylene/carbon black films in the elastic and plastic regimes. Composites science and technology 2014, 97, 34-40.

23. Xu, H.; Zeng, Z.; Wu, Z.; Zhou, L.; Su, Z.; Liao, Y.; Liu, M., Broadband dynamic responses of flexible carbon black/poly (vinylidene fluoride) nanocomposites: A sensitivity study. Composites Science and Technology 2017, 149, 246-253.

24. Flandin, L.; Chang, A.; Nazarenko, S.; Hiltner, A.; Baer, E., Effect of strain on the properties of an ethylene–octene elastomer with conductive carbon fillers. Journal of Applied Polymer Science 2000, 76, (6), 894-905.

25. Jha, V.; Thomas, A.; Bennett, M.; Busfield, J., Reversible electrical behavior with strain for a carbon black-filled rubber. Journal of applied polymer science 2010, 116, (1), 541-546.

26. Zhao, J.; Dai, K.; Liu, C.; Zheng, G.; Wang, B.; Liu, C.; Chen, J.; Shen, C., A comparison between strain sensing behaviors of carbon black/polypropylene and carbon nanotubes/polypropylene electrically conductive composites. Composites Part A: Applied Science and Manufacturing 2013, 48, 129-136.

27. Lin, L.; Deng, H.; Gao, X.; Zhang, S.; Bilotti, E.; Peijs, T.; Fu, Q., Modified resistivity–strain behavior through the incorporation of metallic particles in conductive polymer composite fibers containing carbon nanotubes. Polymer international 2013, 62, (1), 134-140.

28. Bilotti, E.; Zhang, H.; Deng, H.; Zhang, R.; Fu, Q.; Peijs, T., Controlling the dynamic percolation of carbon nanotube based conductive polymer composites by addition of secondary nanofillers: the effect on electrical conductivity and tuneable sensing behaviour. Composites Science and Technology 2013, 74, 85-90.

29. Zhang, R.; Deng, H.; Valenca, R.; Jin, J.; Fu, Q.; Bilotti, E.; Peijs, T., Strain sensing behaviour of elastomeric composite films containing carbon nanotubes under cyclic loading. Composites Science and Technology 2013, 74, 1-5.

30. Wang, X.; Liu, X.; Yuan, H.; Liu, H.; Liu, C.; Li, T.; Yan, C.; Yan, X.; Shen, C.; Guo, Z., Non-covalently functionalized graphene strengthened poly (vinyl alcohol). Materials & Design 2018, 139, 372-379.

31. Liu, H.; Li, Y.; Dai, K.; Zheng, G.; Liu, C.; Shen, C.; Yan, X.; Guo, J.; Guo, Z., Electrically conductive thermoplastic elastomer nanocomposites at ultralow graphene loading levels for strain sensor applications. Journal of Materials Chemistry C 2016, 4, (1), 157-166.

32. Liao, K.-H.; Park, Y. T.; Abdala, A.; Macosko, C., Aqueous reduced graphene/thermoplastic polyurethane nanocomposites. Polymer 2013, 54, (17), 4555-4559.

33. Kaliyathan, A. V.; Rane, A. V.; Huskic, M.; Kunaver, M.; Kalarikkal, N.; Rouxel, D.; Thomas, S., Influence of carbon black on cure properties and mechanical strength of natural rubber/butadiene rubber blends. Journal of Macromolecular Science, Part A 2020, 1-12.

34. Liu, S.; Lin, Y.; Wei, Y.; Chen, S.; Zhu, J.; Liu, L., A high performance self-healing strain sensor with synergetic networks of poly (ε-caprolactone) microspheres, graphene and silver nanowires. Composites Science and Technology 2017, 146, 110-118.

35. Wei, Y.; Chen, S.; Li, F.; Lin, Y.; Zhang, Y.; Liu, L., Highly stable and sensitive paper-based bending sensor using silver nanowires/layered double hydroxides hybrids. ACS applied materials & interfaces 2015, 7, (26), 14182-14191.

36. Lu, L.; Wei, X.; Zhang, Y.; Zheng, G.; Dai, K.; Liu, C.; Shen, C., A flexible and self-formed sandwich structure strain sensor based on AgNW decorated electrospun fibrous mats with excellent sensing capability and good oxidation inhibition properties. Journal of Materials Chemistry C 2017, 5, (28), 7035-7042.

37. Wu, X.; Lu, C.; Zhang, X.; Zhou, Z., Conductive natural rubber/carbon black nanocomposites via cellulose nanowhisker templated assembly: tailored hierarchical structure leading to synergistic property enhancements. Journal of Materials Chemistry A 2015, 3, (25), 13317-13323.

38. Wei, Y.; Chen, S.; Dong, X.; Lin, Y.; Liu, L., Flexible piezoresistive sensors based on “dynamic bridging effect” of silver nanowires toward graphene. Carbon 2017, 113, 395-403.

39. Zhou, Y.; Zhou, Y.; Deng, H.; Fu, Q., A novel route towards tunable piezoresistive behavior in conductive polymer composites: Addition of insulating filler with different size and surface characteristics. Composites Part A: Applied Science and Manufacturing 2017, 96, 99-109.

40. Lin, L.; Liu, S.; Zhang, Q.; Li, X.; Ji, M.; Deng, H.; Fu, Q., Towards tunable sensitivity of electrical property to strain for conductive polymer composites based on thermoplastic elastomer. ACS applied materials & interfaces 2013, 5, (12), 5815-5824.

41. Ke, K.; Pötschke, P.; Wiegand, N.; Krause, B.; Voit, B., Tuning the network structure in poly (vinylidene fluoride)/carbon nanotube nanocomposites using carbon black: toward improvements of conductivity and piezoresistive sensitivity. ACS applied materials & interfaces 2016, 8, (22), 14190-14199.

42. Zhao, H.; Bai, J., Highly sensitive piezo-resistive graphite nanoplatelet–carbon nanotube hybrids/polydimethylsilicone composites with improved conductive network construction. ACS applied materials & interfaces 2015, 7, (18), 9652-9659.

43. Liu, H.; Huang, W.; Yang, X.; Dai, K.; Zheng, G.; Liu, C.; Shen, C.; Yan, X.; Guo, J.; Guo, Z., Organic vapor sensing behaviors of conductive thermoplastic polyurethane–graphene nanocomposites. Journal of Materials Chemistry C 2016, 4, (20), 4459-4469.

44. Liu, H.; Gao, J.; Huang, W.; Dai, K.; Zheng, G.; Liu, C.; Shen, C.; Yan, X.; Guo, J.; Guo, Z., Electrically conductive strain sensing polyurethane nanocomposites with synergistic carbon nanotubes and graphene bifillers. Nanoscale 2016, 8, (26), 12977-12989.

45. Fan, Q.; Qin, Z.; Gao, S.; Wu, Y.; Pionteck, J.; Mäder, E.; Zhu, M., The use of a carbon nanotube layer on a polyurethane multifilament substrate for monitoring strains as large as 400%. Carbon 2012, 50, (11), 4085-4092.

46. Li, M.; Li, H.; Zhong, W.; Zhao, Q.; Wang, D., Stretchable conductive polypyrrole/polyurethane (PPy/PU) strain sensor with netlike microcracks for human breath detection. ACS applied materials & interfaces 2014, 6, (2), 1313-1319.

47. Seyedin, M. Z.; Razal, J. M.; Innis, P. C.; Wallace, G. G., Strain-responsive polyurethane/PEDOT: PSS elastomeric composite fibers with high electrical conductivity. Advanced Functional Materials 2014, 24, (20), 2957-2966.

48. Yamada, T.; Hayamizu, Y.; Yamamoto, Y.; Yomogida, Y.; Izadi-Najafabadi, A.; Futaba, D. N.; Hata, K., A stretchable carbon nanotube strain sensor for human-motion detection. Nature nanotechnology 2011, 6, (5), 296.

49. Boland, C. S.; Khan, U.; Backes, C.; O'Neill, A.; McCauley, J.; Duane, S.; Shanker, R.; Liu, Y.; Jurewicz, I.; Dalton, A. B., Sensitive, high-strain, high-rate bodily motion sensors based on graphene–rubber composites. ACS nano 2014, 8, (9), 8819-8830.

50. Zhao, S.; Li, J.; Cao, D.; Gao, Y.; Huang, W.; Zhang, G.; Sun, R.; Wong, C.-P., Percolation threshold-inspired design of hierarchical multiscale hybrid architectures based on carbon nanotubes and silver nanoparticles for stretchable and printable electronics. Journal of Materials Chemistry C 2016, 4, (27), 6666-6674.

51. Lee, S.; Shin, S.; Lee, S.; Seo, J.; Lee, J.; Son, S.; Cho, H. J.; Algadi, H.; Al-Sayari, S.; Kim, D. E., Ag nanowire reinforced highly stretchable conductive fibers for wearable electronics. Advanced Functional Materials 2015, 25, (21), 3114-3121.

52. Zhang, R.; Baxendale, M.; Peijs, T., Universal resistivity–strain dependence of carbon nanotube/polymer composites. Physical Review B 2007, 76, (19), 195433.

53. Zhang, B.; Lei, J.; Qi, D.; Liu, Z.; Wang, Y.; Xiao, G.; Wu, J.; Zhang, W.; Huo, F.; Chen, X., Stretchable conductive fibers based on a cracking control strategy for wearable electronics. Advanced Functional Materials 2018, 28, (29), 1801683.

54. Wallace, G.; Smyth, M.; Zhao, H., Conducting electroactive polymer-based biosensors. TrAC Trends in Analytical Chemistry 1999, 18, (4), 245-251.

55. Bagheri, H.; Ayazi, Z.; Naderi, M., Conductive polymer-based microextraction methods: a review. Analytica chimica acta 2013, 767, 1-13.

56. Diouf, A.; Bouchikhi, B.; El Bari, N., A nonenzymatic electrochemical glucose sensor based on molecularly imprinted polymer and its application in measuring saliva glucose. Materials Science and Engineering: C 2019, 98, 1196-1209.

57. Shaidarova, L.; Budnikov, G., Chemically modified electrodes based on noble metals, polymer films, or their composites in organic voltammetry. Journal of Analytical Chemistry 2008, 63, (10), 922-942.

58. Dhand, C.; Das, M.; Datta, M.; Malhotra, B., Recent advances in polyaniline based biosensors. Biosensors and Bioelectronics 2011, 26, (6), 2811-2821.

59. Nambiar, S.; Yeow, J. T., Conductive polymer-based sensors for biomedical applications. Biosensors and Bioelectronics 2011, 26, (5), 1825-1832.

60. Li, C.; Bai, H.; Shi, G., Conducting polymer nanomaterials: electrosynthesis and applications. Chemical Society Reviews 2009, 38, (8), 2397-2409.

61. Angelopoulos, M., Conducting polymers in microelectronics. IBM Journal of Research and Development 2001, 45, (1), 57-75.

62. Prakash, S.; Chakrabarty, T.; Singh, A. K.; Shahi, V. K., Polymer thin films embedded with metal nanoparticles for electrochemical biosensors applications. Biosensors and Bioelectronics 2013, 41, 43-53.

63. Singh, K.; Solanki, P. R.; Basu, T.; Malhotra, B., Polypyrrole/multiwalled carbon nanotubes-based biosensor for cholesterol estimation. Polymers for Advanced Technologies 2012, 23, (7), 1084-1091.

64. Karadas, N.; Ozkan, S. A., Electrochemical preparation of sodium dodecylsulfate doped over-oxidized polypyrrole/multi-walled carbon nanotube composite on glassy carbon electrode and its application on sensitive and selective determination of anticancer drug: Pemetrexed. Talanta 2014, 119, 248-254.

65. Shahrokhian, S.; Azimzadeh, M.; Amini, M. K., Modification of glassy carbon electrode with a bilayer of multiwalled carbon nanotube/tiron-doped polypyrrole: application to sensitive voltammetric determination of acyclovir. Materials Science and Engineering: C 2015, 53, 134-141.

66. Karolia, P.; Tiwari, D.; Jain, R., Electrocatalytic sensing of omeprazole. Ionics 2015, 21, (8), 2355-2362.

67. Xu, G.; Li, B.; Luo, X., Carbon nanotube doped poly (3, 4-ethylenedioxythiophene) for the electrocatalytic oxidation and detection of hydroquinone. Sensors and Actuators B: Chemical 2013, 176, 69-74.

68. Xu, G.; Li, B.; Cui, X. T.; Ling, L.; Luo, X., Electrodeposited conducting polymer PEDOT doped with pure carbon nanotubes for the detection of dopamine in the presence of ascorbic acid. Sensors and Actuators B: Chemical 2013, 188, 405-410.

69. Xu, G.; Li, B.; Wang, X.; Luo, X., Electrochemical sensor for nitrobenzene based on carbon paste electrode modified with a poly (3, 4-ethylenedioxythiophene) and carbon nanotube nanocomposite. Microchimica Acta 2014, 181, (3-4), 463-469.

70. Fan, Y.; Liu, J.-H.; Yang, C.-P.; Yu, M.; Liu, P., Graphene–polyaniline composite film modified electrode for voltammetric determination of 4-aminophenol. Sensors and Actuators B: Chemical 2011, 157, (2), 669-674.

71. Radhapyari, K.; Kotoky, P.; Das, M. R.; Khan, R., Graphene–polyaniline nanocomposite based biosensor for detection of antimalarial drug artesunate in pharmaceutical formulation and biological fluids. Talanta 2013, 111, 47-53.

72. Jain, R.; Tiwari, D. C.; Shrivastava, S., A sensitive voltammetric sensor based on synergistic effect of polyaniline and zirconia nanocomposite film for quantification of proton pump inhibitor esomeprazole. Journal of the Electrochemical Society 2014, 161, (4), B39.

73. Jain, R.; Tiwari, D.; Karolia, P., Electrocatalytic detection and quantification of nitazoxanide based on graphene-polyaniline (Grp-Pani) nanocomposite sensor. Journal of The Electrochemical Society 2014, 161, (12), H839.

74. Gao, Y.-S.; Xu, J.-K.; Lu, L.-M.; Wu, L.-P.; Zhang, K.-X.; Nie, T.; Zhu, X.-F.; Wu, Y., Overoxidized polypyrrole/graphene nanocomposite with good electrochemical performance as novel electrode material for the detection of adenine and guanine. Biosensors and Bioelectronics 2014, 62, 261-267.

75. Zhang, W.; Yuan, R.; Chai, Y.-Q.; Zhang, Y.; Chen, S.-H., A simple strategy based on lanthanum–multiwalled carbon nanotube nanocomposites for simultaneous determination of ascorbic acid, dopamine, uric acid and nitrite. Sensors and Actuators B: Chemical 2012, 166, 601-607.

76. a: Lei, J.-C.; Zhang, X.; Zhou, Z., Recent advances in MXene: Preparation, properties, and applications. Frontiers of Physics 2015, 10, (3), 276-286. b: Kuang, P.; Low, J.; Cheng, B.; Yu, J.; Fan, J., MXene-based photocatalysts. Journal of Materials Science & Technology 2020. c:Liu, H.; Duan, C.; Yang, C.; Shen, W.; Wang, F.; Zhu, Z., A novel nitrite biosensor based on the direct electrochemistry of hemoglobin immobilized on MXene-Ti3C2. Sensors and Actuators B: Chemical 2015, 218, 60-66. d: Rakhi, R. B.; Nayak, P.; Xia, C.; Alshareef, H. N., Novel amperometric glucose biosensor based on MXene nanocomposite. Scientific Reports 2016, 6, (1), 36422. e: Wang, Q.; Min, F.; Zhu, J., Preparation of gold nanowires and its application in glucose biosensing. Materials Letters 2013, 91, 9-11.

77. Wang, L.; Hua, E.; Liang, M.; Ma, C.; Liu, Z.; Sheng, S.; Liu, M.; Xie, G.; Feng, W., Graphene sheets, polyaniline and AuNPs based DNA sensor for electrochemical determination of BCR/ABL fusion gene with functional hairpin probe. Biosensors and Bioelectronics 2014, 51, 201-207.

78. Siangproh, W.; Dungchai, W.; Rattanarat, P.; Chailapakul, O., Nanoparticle-based electrochemical detection in conventional and miniaturized systems and their bioanalytical applications: A review. Analytica chimica acta 2011, 690, (1), 10-25.

79. Devi, R.; Thakur, M.; Pundir, C., Construction and application of an amperometric xanthine biosensor based on zinc oxide nanoparticles–polypyrrole composite film. Biosensors and Bioelectronics 2011, 26, (8), 3420-3426.

80. Mahmoudian, M.; Alias, Y.; Basirun, W. J.; Ebadi, M., Preparation of ultra-thin polypyrrole nanosheets decorated with Ag nanoparticles and their application in hydrogen peroxide detection. Electrochimica Acta 2012, 72, 46-52.

81. Xing, L.; Rong, Q.; Ma, Z., Non-enzymatic electrochemical sensing of hydrogen peroxide based on polypyrrole/platinum nanocomposites. Sensors and Actuators B: Chemical 2015, 221, 242-247.

82. Zou, L.; Li, Y.; Cao, S.; Ye, B., Gold nanoparticles/polyaniline Langmuir–Blodgett Film modified glassy carbon electrode as voltammetric sensor for detection of epinephrine and uric acid. Talanta 2013, 117, 333-337.

83. Jain, R.; Tiwari, D. C.; Shrivastava, S., Polyaniline–bismuth oxide nanocomposite sensor for quantification of anti-parkinson drug pramipexole in solubilized system. Materials Science and Engineering: B 2014, 185, 53-59.

84. Jain, R.; Tiwari, D.; Karolia, P., Highly sensitive and selective polyaniline–zinc oxide nanocomposite sensor for betahistine hydrochloride in solubilized system. Journal of Molecular Liquids 2014, 196, 308-313.

85. Shrivastava, S.; Jadon, N.; Jain, R., Next-generation polymer nanocomposite-based electrochemical sensors and biosensors: A review. TrAC Trends in Analytical Chemistry 2016, 82, 55-67.

86. Wang, L.; Yang, R.; Wang, H.; Li, J.; Qu, L.; Harrington, P. d. B., High-selective and sensitive voltammetric sensor for butylated hydroxyanisole based on AuNPs–PVP–graphene nanocomposites. Talanta 2015, 138, 169-175.

87. Baghayeri, M.; Zare, E. N.; Lakouraj, M. M., A simple hydrogen peroxide biosensor based on a novel electro-magnetic poly (p-phenylenediamine)@ Fe3O4 nanocomposite. Biosensors and bioelectronics 2014, 55, 259-265.

88. Ruecha, N.; Rangkupan, R.; Rodthongkum, N.; Chailapakul, O., Novel paper-based cholesterol biosensor using graphene/polyvinylpyrrolidone/polyaniline nanocomposite. Biosensors and Bioelectronics 2014, 52, 13-19.

89. Zhu, J.; Liu, X.; Wang, X.; Huo, X.; Yan, R., Preparation of polyaniline–TiO2 nanotube composite for the development of electrochemical biosensors. Sensors and Actuators B: Chemical 2015, 221, 450-457.

90. Yu, Z.; Li, H.; Zhang, X.; Liu, N.; Tan, W.; Zhang, X.; Zhang, L., Facile synthesis of NiCo2O4@ Polyaniline core–shell nanocomposite for sensitive determination of glucose. Biosensors and Bioelectronics 2016, 75, 161-165.

91. Safari, A.; Akdogan, E. K., Piezoelectric and acoustic materials for transducer applications. Springer Science & Business Media: 2008.

92. Uchino, K. Introduction to piezoelectric actuators and transducers; PENNSYLVANIA STATE UNIV UNIVERSITY PARK: 2003.

93. Sappati, K. K.; Bhadra, S., Piezoelectric polymer and paper substrates: a review. Sensors 2018, 18, (11), 3605.

94. Soin, N.; Boyer, D.; Prashanthi, K.; Sharma, S.; Narasimulu, A. A.; Luo, J.; Shah, T. H.; Siores, E.; Thundat, T., Exclusive self-aligned β-phase PVDF films with abnormal piezoelectric coefficient prepared via phase inversion. Chemical Communications 2015, 51, (39), 8257-8260.

95. Chiu, Y.-Y.; Lin, W.-Y.; Wang, H.-Y.; Huang, S.-B.; Wu, M.-H., Development of a piezoelectric polyvinylidene fluoride (PVDF) polymer-based sensor patch for simultaneous heartbeat and respiration monitoring. Sensors and Actuators A: Physical 2013, 189, 328-334.

96. Ponnamma, D.; Chamakh, M. M.; Deshmukh, K.; Ahamed, M. B.; Erturk, A.; Sharma, P.; Al-Maadeed, M. A.-A., Ceramic-based polymer nanocomposites as piezoelectric materials. In Smart Polymer Nanocomposites, Springer: 2017; pp 77-93.

97. Harrison, J.; Ounaies, Z., Piezoelectric polymers. Encyclopedia of polymer science and technology 2002, 3.

98. Smith, W. A. In The role of piezocomposites in ultrasonic transducers, Proceedings., IEEE Ultrasonics Symposium, 1989; IEEE: 1989; pp 755-766.

99. Ramadan, K. S.; Sameoto, D.; Evoy, S., A review of piezoelectric polymers as functional materials for electromechanical transducers. Smart Materials and Structures 2014, 23, (3), 033001.

100. Hillenbrand, J.; Sessler, G., Quasistatic and dynamic piezoelectric coefficients of polymer foams and polymer film systems. IEEE Transactions on Dielectrics and Electrical Insulation 2004, 11, (1), 72-79.

101. Bauer, S.; Gerhard, R.; Sessler, G. M., Ferroelectrets: Soft electroactive foams for transducers. 2004.

102. Heikkinen, L.; Panula, H.; Lyyra, T.; Olkkonen, H.; Kiviranta, I.; Nevalainen, T.; Helminen, H., Electromechanical film sensor device for dynamic force recordings from canine limbs. Scandinavian Journal of Laboratory Animal Science (Denmark) 1997.

103. Wang, T. T., Production of piezoelectric PVDF films. In Google Patents: 1980.

104. Chowdhury, T.; D'Souza, N.; Ho, Y. H.; Dahotre, N.; Mahbub, I., Embedded Corrosion Sensing with ZnO-PVDF Sensor Textiles. Sensors 2020, 20, (11), 3053.

105. Kim, J. Y.-H.; Cheng, A.; Tai, Y.-C. In Parylene-C as a piezoelectric material, 2011 IEEE 24th International Conference on Micro Electro Mechanical Systems, 2011; IEEE: 2011; pp 473-476.

106. Li, L.; Zhang, M.; Rong, M.; Ruan, W., Studies on the transformation process of PVDF from α to β phase by stretching. RSC Advances 2014, 4, (8), 3938-3943.

107. Sirohi, J.; Chopra, I., Piezoceramic actuators and sensors. Encyclopedia of aerospace engineering 2010.

108. Deutz, D. B.; Mascarenhas, N. T.; Schelen, J. B. J.; de Leeuw, D. M.; van der Zwaag, S.; Groen, P., Flexible Piezoelectric Touch Sensor by Alignment of Lead-Free Alkaline Niobate Microcubes in PDMS. Advanced Functional Materials 2017, 27, (24), 1700728.

109. Singh, A.; Das, S.; Bharathkumar, M.; Revanth, D.; Karthik, A.; Sastry, B. S.; Rao, V. R., Low cost fabrication of polymer composite (h-ZnO+ PDMS) material for piezoelectric device application. Materials Research Express 2016, 3, (7), 075702.

110. Racles, C.; Dascalu, M.; Bele, A.; Tiron, V.; Asandulesa, M.; Tugui, C.; Vasiliu, A.-L.; Cazacu, M., All-silicone elastic composites with counter-intuitive piezoelectric response, designed for electromechanical applications. Journal of Materials Chemistry C 2017, 5, (28), 6997-7010.

111. Akiyama, M.; Morofuji, Y.; Kamohara, T.; Nishikubo, K.; Tsubai, M.; Fukuda, O.; Ueno, N., Flexible piezoelectric pressure sensors using oriented aluminum nitride thin films prepared on polyethylene terephthalate films. Journal of applied physics 2006, 100, (11), 114318.

112. Van den Ende, D.; De Almeida, P.; Van der Zwaag, S., Piezoelectric and mechanical properties of novel composites of PZT and a liquid crystalline thermosetting resin. Journal of materials science 2007, 42, (15), 6417-6425.

113. Choi, W.; Choi, K.; Yang, G.; Kim, J. C.; Yu, C., Improving piezoelectric performance of lead-free polymer composites with high aspect ratio BaTiO3 nanowires. Polymer Testing 2016, 53, 143-148.

114. Kachroudi, A.; Basrour, S.; Rufer, L.; Sylvestre, A.; Jomni, F., Micro-structured PDMS piezoelectric enhancement through charging conditions. Smart Materials and Structures 2016, 25, (10), 105027.

115. Mohebbi, A.; Mighri, F.; Ajji, A.; Rodrigue, D., Polymer ferroelectret based on polypropylene foam: piezoelectric properties prediction using dynamic mechanical analysis. Polymers for Advanced Technologies 2017, 28, (4), 476-483.

116. Mahanty, B.; Ghosh, S. K.; Garain, S.; Mandal, D., An effective flexible wireless energy harvester/sensor based on porous electret piezoelectric polymer. Materials Chemistry and Physics 2017, 186, 327-332.

117. Zhang, M.; Gao, T.; Wang, J.; Liao, J.; Qiu, Y.; Xue, H.; Shi, Z.; Xiong, Z.; Chen, L., Single BaTiO3 nanowires-polymer fiber based nanogenerator. Nano Energy 2015, 11, 510-517.

118. Sharma, M.; Srinivas, V.; Madras, G.; Bose, S., Outstanding dielectric constant and piezoelectric coefficient in electrospun nanofiber mats of PVDF containing silver decorated multiwall carbon nanotubes: assessing through piezoresponse force microscopy. RSC advances 2016, 6, (8), 6251-6258.

119. Assagra, Y. A. O.; Altafim, R. A. C.; do Carmo, J. P. P.; Altafim, R. A. P. In Well-defined piezoelectrets fabricated with 3D printing technology, 2016 IEEE International Conference on Dielectrics (ICD), 2016; IEEE: 2016; pp 257-259.

120. Mitu, B.; Bauer-Gogonea, S.; Leonhartsberger, H.; Lindner, M.; Bauer, S.; Dinescu, G., Plasma-deposited parylene-like thin films: process and material properties. Surface and Coatings Technology 2003, 174, 124-130.

CHAPTER 3

EMBEDDED CORROSION SENSING WITH ZnO-PVDF SENSOR TEXTILES: PROOF OF CONCEPT*

3.1 Introduction

Applying coatings is a common approach to protect metal surfaces from salt-water corrosion. Electrically insulative polymeric coatings are primarily used for this purpose because of their excellent corrosion resistance and adhesive properties. Yet, these protective coatings are subject to failure because of the prolonged exposure of the coated surface to the harsh corrosive environment. This degradation or failure of the coating results in corrosion of the metal causing significant economic and environmental impact [1]. A recent study in the USA calculated the cost of corrosion to be $276 billion corresponding to 3.1% of the U.S. gross domestic product (GDP) [2]. Detection or sensing of degradation of coating is very important.

In general, a sensing system is classified into two broad categories: active and passive [3]. When the sensor system induces a change in the coating and an external sensor is required to detect it, then the system is passive. An example of this is Electrical Resistance (ER) probes which can measure the metal loss from corrosion by measuring the electrical resistance [4]. On the other hand, systems are termed “active” when the sensing system directly outputs a signal such as color change in the coating. Active sensors based on color-changing compounds, dyes and fluorescence materials for corrosion detection were reviewed by Feng et al. [5]. Color dyes that respond to

---

* This chapter is reproduced from Chowdhury, T.; D'Souza, N.; Ho, Y.H.; Dahotre, N.; Mahbub, I. Embedded Corrosion Sensing with ZnO-PVDF Sensor Textiles. Sensors 2020, 20, 3053. Doi: https://doi.org/10.3390/s20113053 MDPI journal: published under Creative Common CC BY license. Authors retain copyright.

changes in pH occurring from corrosion were analyzed by Augustyniak et al. and Frankel et al. [6,7]. Fluorescent particles that transition from non-fluorescent to fluorescent states upon contact with salt water, have driven sensors based on oxidation-reduction reactions [1,8,9]. Color dyes have also been used in embedded microcapsules for corrosion mitigation followed by crack propagation [10].

For buried pipes, both active and passive sensing systems have limits. Active sensing approaches are limited when one deals with subsurface or immersed pipe systems since color change is no longer visible. Passive sensing systems like ER and eddy current testing systems have not been found to be sensitive enough to detect early stages of corrosion [11-16]. In applications of corrosion, the main reason for inadequate performance of optical fiber sensors has been that the sensor itself was electrochemically reactive [5]. Smart coatings, such as self healing coatings, where physical damage in a coating is self-repaired to regain barrier properties before metal corrosion occurs have been gaining ground [17-21]. But serious chemical and mechanical limitations of these coatings have been noted [22]. None of these sensors are compatible with real-time corrosion sensing in an environment under any coating systems. Continuous monitoring via embedded sensing is receiving much interest [23]. Kittel et al. deposited a gold and nickel metal layer to measure the impedance of different parts of the coating (i.e. solution + outer layer, inner layer + substrate) [24,25]. Bierwagen et al. embedded platinum in between two layers of the coating to measure real-time corrosion in their work [26-29]. A constraint emerges that with a high fraction of sensing elements being metallic, corrosion can be exacerbated from their use.

Regardless of the type of sensor, there is a concern with cost in wide area application and measurement of the corrosion response.

In this chapter, we investigated a sensing element that could be compatible with a real-time continuous measurement system for corrosion. To overcome the limits of the sensing element being highly conductive and thereby accentuating the corrosion of the pipe, a non-conductive sensing textile was used. We utilized polyvinylfluoride (PVDF) as the polymer and evaluated the impact of adding a non-metallic ceramic filler. To mitigate the cost of the sensor, we used a non-woven manufacturing approach by using electrospinning. Electrospun PVDF fiber mesh is already known for its energy-harvesting capacity as the α phase of the PVDF is converted into the β phase through the electrospinning process which increases the piezoelectric property [30,31]. In addition to its energy-harvesting property, the fiber can also be used as a corrosion sensor as it changes its resistance from dry state to wet state and can act as a barrier between steel and corrosion species. The goal of the approach was to investigate the viability of using a sensing textile at the interface between the coating and metal substrate. ZnO-PVDF nanocomposite fiber meshes were fabricated using electrospinning by varying ZnO ratios from 1-5 wt%. To estimate the fiber dimensions within the mesh, Scanning Electron Microscopy (SEM) was carried out followed by image analysis. PVDF's ability to function as a sensor textile is closely related to the crystal structure. The α phase does not provide a piezoelectric response but a transformed β phase does. The β phase is typically formed through poling subsequent to manufacture, but we have recently outlined the transformation in a single step method which has been enabled through electrospinning [32]. The β phase for the

PVDF and the ZnO modified meshes were examined using X-ray Diffraction (XRD) and Fourier Transform Infrared Spectroscopy (FTIR). The magnitude of the piezoelectric coefficient (d_{33}) was measured using the d_{33} meter. Then the fibers were embedded in between two layers of epoxy coating over steel substrate. The performance of fiber meshes as a sensor was evaluated by using Electrochemical Impedance Spectroscopy (EIS). Viability of the concept was evaluated by examining the EIS for the textile as a stand-alone system as well as embedded at the coating-metal interface. The long-term application would be to incorporate a self-powered electric chip with the textile for real-time impedance measurement as it has been growing in importance [33-35].

3.2 Materials and Methods

PVDF pellets (Kynar® 721) were purchased from Arkema with following properties: density 1.78 g/cc, Melt Flow Index (MFI) 10 g/10 min and tensile strength 54 MPa. ZnO was purchased from Fisher Scientific Company (Fair Lawn, NJ, USA) with average particle size of 20-30 nm. N,N-dimethylformamide (DMF) and acetone were supplied from Sigma-Aldrich (St. Louis, MO, USA). The coating was a room temperature curable diglycidyl ether-based epoxy resin with hardener having a 2:1 stoichiometry which was obtained from System Three (Lacey, WA, USA). The low-carbon steel (AISI-SAE 1018) was received from McMaster-Carr (Santa Fe Spring, CA, USA), and the sea salt was supplied by Lake Products Company LLC (Florissant, MO, USA).

3.2.1 Preparation of the PVDF and ZnO Nonwoven Textile Mesh

PVDF pellets (18% w/w) were dissolved in DMF/Acetone mixture (2:1 by weight) solution by stirring at 50 °C for 2 hours using magnetic stirrer at 200 rpm. After all the pellets dissolved, ZnO (1%, 3% and 5% w/w with respect to polymer) was added into the solution. Ultrasonication was performed with Sonic Vibracell II (25% pulse amplitude) for 5 mins to have a homogeneous solution. Then the solution was loaded into a 5 mL syringe fitted with a 0.038 in diameter stainless steel needle and fed at 0.05 mL/h with a syringe pump (NE-300, New Era Pump Systems, Farmingdale, NY, USA). Electrospinning was carried out at a voltage of 15 kV using a DC power supply (ES100R-20W, Kansai Elctronics, Osaka, Japan). A rotating roller with a non-stick aluminum foil was collecting the fiber at 400 rpm.

3.2.2 Nanofiber Mesh Characterization

Surface morphology of sputter coated fiber meshes was observed by using the FEI Nova NanoSEM 230 Scanning Electron Microprobe. Crystal structures of PVDF and ZnO-PVDF composite meshes were examined by using a Rigaku Ultima III X-ray diffractometer. A Scientific Nicolet 6700 Fourier Transform Infrared Spectroscopy (FT-IR) was used to characterize the functional groups in PVDF and ZnO-PVDF meshes. Thermal properties of the meshes were studied using Perkin Elmer DSC6 Differential Scanning Calorimeter. The scanning range was 30 °C to 210 °C at the rate of 10 °C/min to calculate the melting temperature and enthalpy. A d_{33} meter was used to measure the piezoelectric coefficient value of the fiber.

3.2.3 Preparation of Corrosion Sensor Sample

Steel coupons having a dimension of 50 X 25.4 X 3.2 mm were obtained. First, the steel coupons were polished using a SiC sheet grit 240 and 600 respectively as mentioned in ASTM G5 for corrosion test requirements. After polishing, the coupons were washed with distilled water and acetone respectively and left at room temperature to dry. Then the epoxy resin was mixed with hardener (2:1 by vol.) and applied on the polished coupons by a smooth brush. The coated coupons were kept at room temperature for 72 hours to cure. After the first layer of the coating was completely cured, a thin layer of same epoxy resin was applied again onto the coating surface intended for the sensor. When the sensor (25 X 15 X 0.025 mm) adhered onto the coating surface, a copper core electrical wire was connected onto the embedded sensor using silver paste and kept into the oven at 100 °C for an hour. Then the second layer of epoxy resin was applied on the surface as shown in Figure 3.1(a). A digital gauge Omega DGT-500 was used to determine the coating thickness of the coupons. The thickness of the base coat and topcoat was 60 µm each leading to a coating thickness of 120±10 µm.

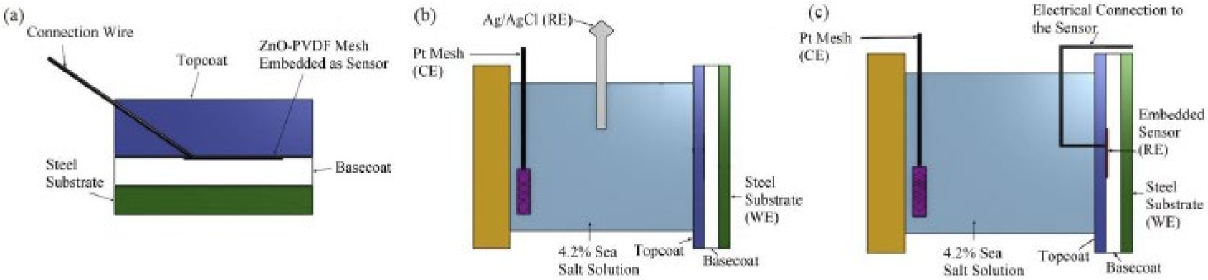

Figure 3.1: Schematic diagram of coated sample and EIS experimental setup (a) cross section view of prepared sample (b) Configuration A (actual data): steel substrate is working electrode (WE), Pt mesh is counter electrode (CE), and Ag/AgCl is reference electrode (RE). (c) Configuration B (sensor data): steel substrate is WE, Pt mesh is CE, and sensor is RE.

To obtain the effectiveness of the sensor in detecting the corrosion/permeation of the fluid, the sensor textile was compared to a calibrated EIS system. A BioLogic SP-300 EIS machine was used using a three electrode configuration. For the EIS of the total coating system, Ag/AgCl used as reference electrode (RE), platinum mesh functioned as the counter electrode (CE) and the steel substrate was the working electrode (WE) as shown in Figure 3.1(b). This set up will be referenced as "Configuration A". To establish validity of the sensor, the EIS set up was modified to convert the sensor textile into the reference electrode as outlined previously by Bierwagen et al. [29,36]. In this configuration, as presented in Figure 3.1(c), the reference electrode was replaced by the sensor textile, with the platinum was the CE and steel was the WE, and the data obtained from this configuration was marked as sensor data. The EIS was collected in a 4.2% sea salt solution each 24 hours for 10 days. The area being sampled was 1 cm^2.

3.3 Results and Discussion

3.3.1 Scanning Electron Microscopy (SEM)

Scanning electron microscopy was used to observe the effect of concentration of ZnO on the morphology of fibers as presented in Figure 3.2. ImageJ software was used to calculate the diameter of fibers and the porosity in the fiber meshes. The presence of ZnO reduced the diameter and porosity of the fibers as shown in Figure 3.3 and Table 3.1. The average fiber diameter was reduced from 0.28 μm to 0.16 μm and porosity reduced from 7.68% to 6.75%. The conductivity of the solution increased after adding ZnO in it. A slow flow rate with the addition of ZnO in the solution acted together to reduce the fiber diameter [37,38]. The O and Zn signals in the EDX chart of the ZnO-PVDF nanocomposite fiber meshes confirmed the presence of ZnO in PVDF fiber as shown in Figure 3.4. Au picks came from the sputter coated thin conductive film over the samples.

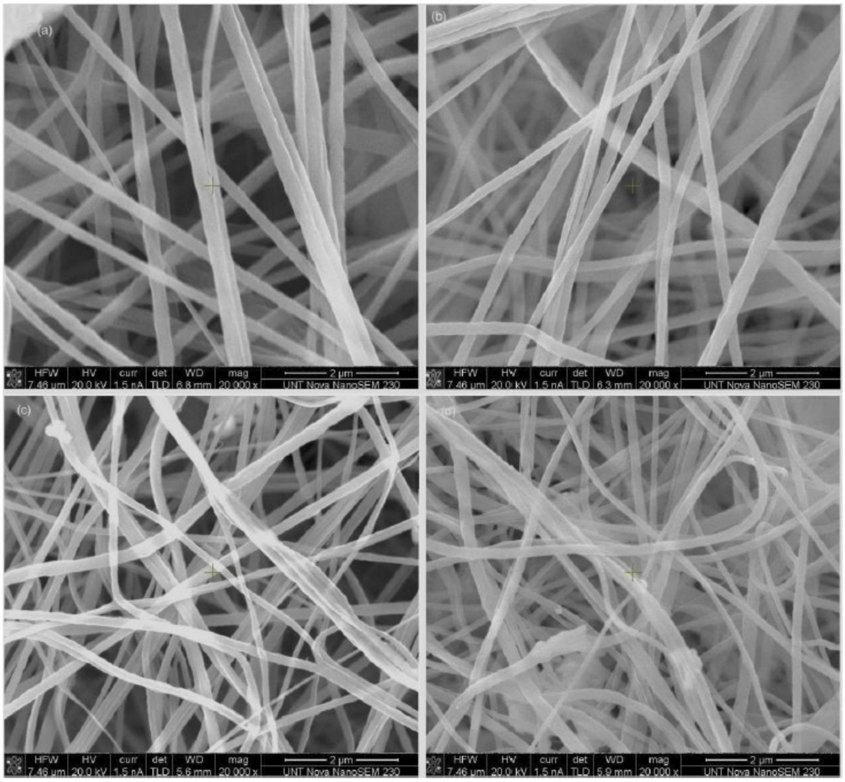

Figure 3.2: SEM images of (a) PVDF fiber, (b) 1% ZnO-PVDF fiber (c) 3% ZnO-PVDF fiber and (d) 5% ZnO-PVDF fiber

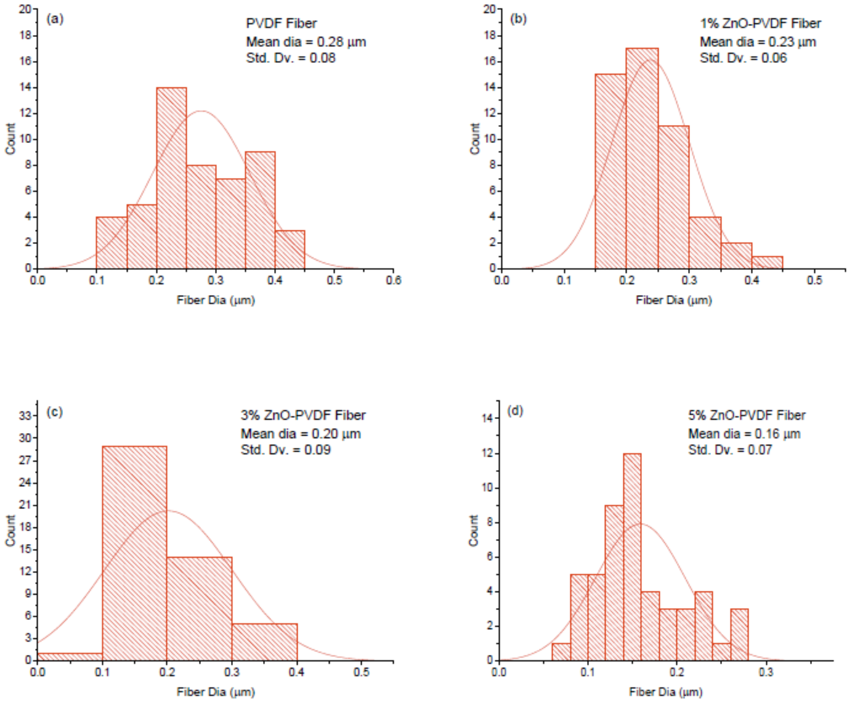

Figure 3.3: Fiber diameter distribution of the non woven textiles (a) PVDF, (b) 1% ZnO-PVDF, (c) 3% ZnO-PVDF and (d) 5% ZnO-PVDF fiber.

Table 3.1: Fiber diameter and porosity

Sample	Average Fiber Diameter (μm)	Average Pore area (μm^2)	Porosity (%)
PVDF Fiber	0.28 ± 0.08	0.015 ± 0.05	7.68
1% ZnO-PVDF	0.23 ± 0.06	0.013 ± 0.03	7.61
3% ZnO-PVDF	0.20 ± 0.09	0.011 ± 0.05	7.36
5% ZnO-PVDF	0.16 ± 0.07	0.010 ± 0.03	6.75

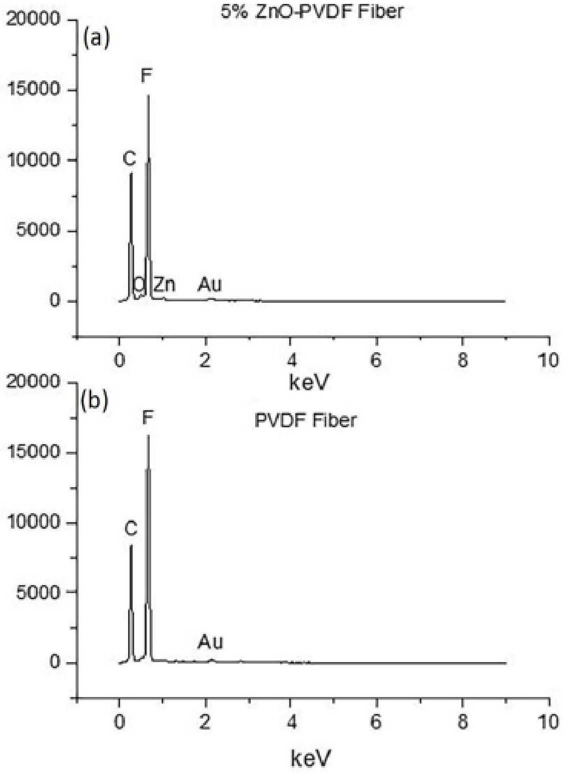

Figure 3.4: EDS of (a) PVDF and (b) 5% ZnO-PVDF fiber

3.3.2 X-Ray Diffraction (XRD)

X-ray diffraction (XRD) patterns of PVDF and ZnO-PVDF nanocomposite fiber meshes are shown in Figure 3.5. The PVDF pellet exhibited two characteristic peaks at 2θ = 18.4° and 20.5° corresponding to α and β crystal phase of PVDF respectively. After electrospinning, the intensity of the α peak decreased and β peak increased indicating that electrospinning process had enlarged the β phase content of PVDF in all the nanocomposite meshes [30,31]. This happened due to the application of high electric voltage (15kV) in the electrospinning process when the random electric dipoles present in the PVDF solution aligned which led the formation of β phase crystal structure [31]. The presence of ZnO was confirmed through the peaks at 31.9°, 34.5°, 36.3°, 47.6°, 56.7°, 62.9° and 68.1° corresponding to (100), (002), (101), (102), (110), (103) and (112) crystallographic orientations which could be indexed as the hexagonal wurtzite structure of ZnO [40,41]. These peaks increased in intensity with increasing ZnO nanoparticles in the meshes.

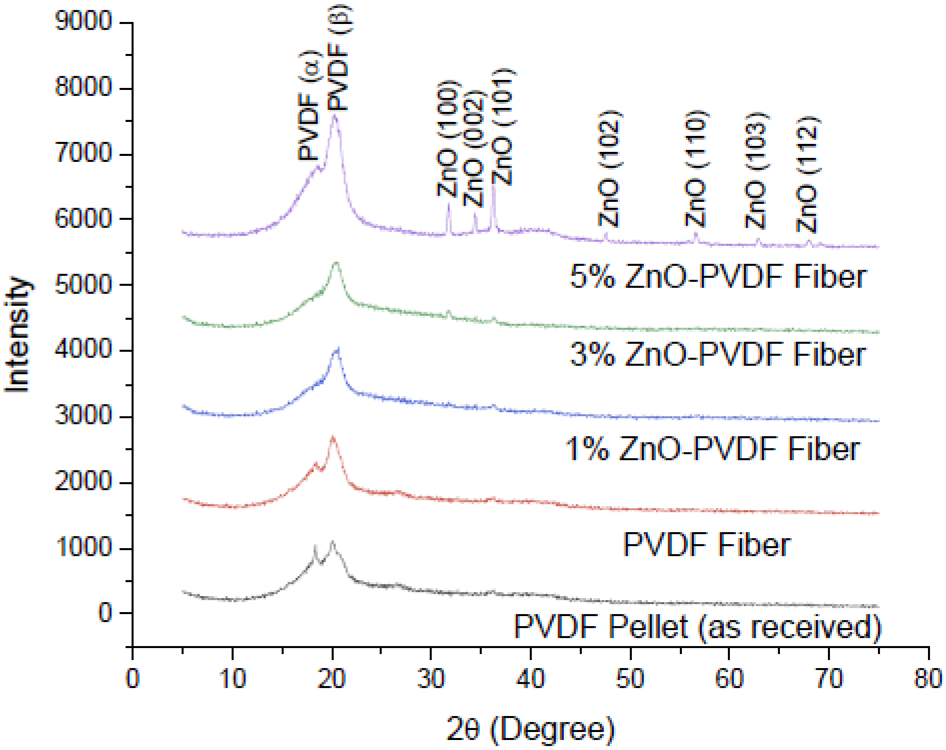

Figure 3.5: XRD pattern of PVDF and ZnO-PVDF fibers

3.3.3 `Fourier Transform Infrared Spectroscopy (FT-IR)

To confirm and examine the crystalline phases indicated in XRD, the FTIR spectra of the electrospun PVDF and ZnO-PVDF nanocomposite meshes were compared (Figure 3.6). The PVDF peaks located at 615 cm^{-1} (CF_2 bending and skeletal bending), 762 cm^{-1} (CF_2 bending), 795 cm^{-1} (CF_2 rocking), and 976 cm^{-1} (CH out-of-plane deformation) were attributed to the α phase whereas the peaks at 840 cm^{-1} (CH_2 rocking), 877 cm^{-1} (CF_2 rocking), 1273 cm^{-1} (CF out-of-plane deformation) and 1402 cm^{-1} (CH_2 scissoring) were considered as β phase [41-44]. The unprocessed PVDF pellet exhibited a dominant α phase together with the β phase. After electrospinning, the peaks corresponding to the α phase decreased in intensity while the β crystalline peaks became stronger. As ZnO was added, the β peak intensity continued to increase. The percentage of the increase in β phase was calculated using Equation 3.1 and shown in Table 3.2 [41]:

$$F(\beta) = \frac{X_\beta}{X_\alpha + X_\beta} \times 100 = \frac{A_\beta}{1.26A_\alpha + A_\beta} \times 100 \qquad \text{(Eq. 3.1)}$$

where F(β) represents the β phase percentage in PVDF, A_α and A_β are their absorption bands at 763 and 840 cm^{-1}. F(β) increased around 40% after electrospinning and adding ZnO into the PVDF fiber increased the β phase further upto 68% for 5% ZnO-PVDF fiber mesh. This signified that both electrospinning and ZnO had a contribution to the β phase of the fiber meshes.

Table 3.2: Percentage of β phase and piezoelectric coefficient (d_{33}) in fiber meshes

Sample	F(β) (%)	d_{33} (pC/N)
PVDF Pellet	48.45	5
PVDF Fiber	67.80	32
1% ZnO-PVDF	79.98	52
3% ZnO-PVDF	80.23	55
5% ZnO-PVDF	81.43	56

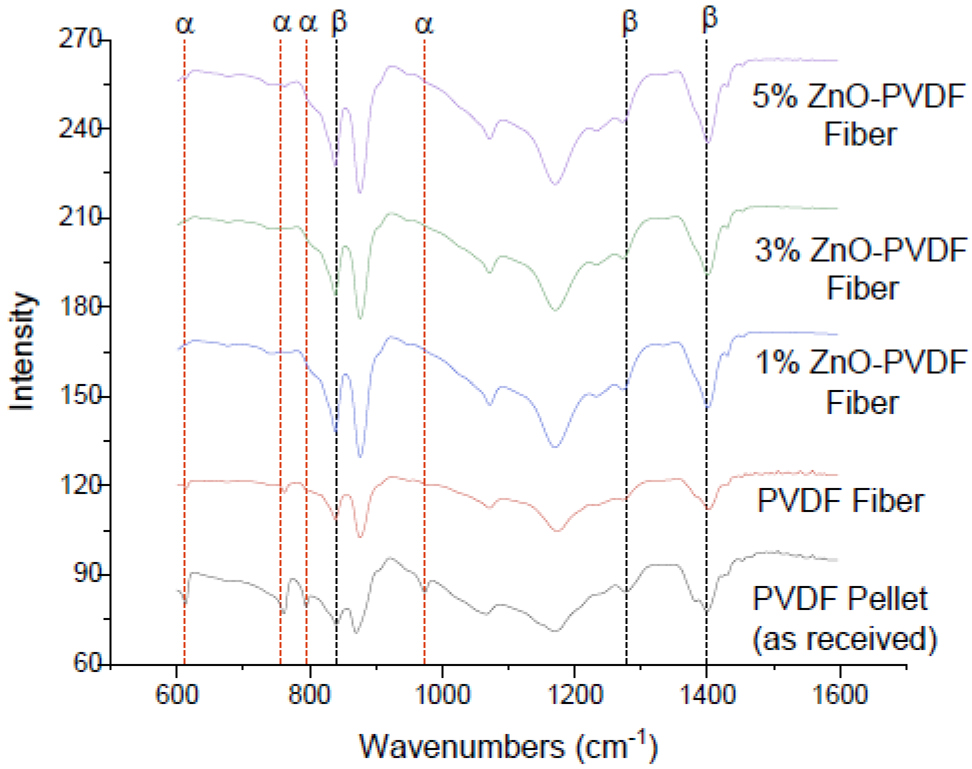

Figure 3.6: FTIR spectra of PVDF and ZnO-PVDF fibers

3.3.4 Differential Scanning Calorimeter (DSC)

The impact of the β phase on the mesh as well as thermal stability of the mesh to withstand the epoxy coating exotherm was estimated using the Differential Scanning Calorimeter (DSC). The results are shown in Figure 3.7 where PVDF showed a melting exothermal at ~160 °C. All the electrospun fiber meshes exhibited a similar melting temperature (T_m) indicating no disruption in the PVDF thermal transitions. The density of the crystalline phase was analyzed using melting enthalpy and degree of crystallinity. The melting enthalpy for the nanofiber meshes is shown in Table 3.3 with the crystallinity of the meshes based on Equation 3.2.

$$X_c = \frac{\Delta H}{\Delta H^{\circ}} \times 100 \qquad \text{(Eq. 3.2)}$$

where X_c is the degree of crystallinity of the fiber mesh, ΔH° is the melting enthalpy of

100% crystalline PVDF (105 J/g) and ΔH is the melting enthalpy of ZnO-PVDF meshes. The results in Table 3.3 showed a small increase in crystallinity and enthalpy with an increase in ZnO content. The crystallinity of the fiber meshes also increased to 19.51% for 5% ZnO-PVDF. The results are in keeping with the literature reports of ZnO-PVDF meshes [44,45].

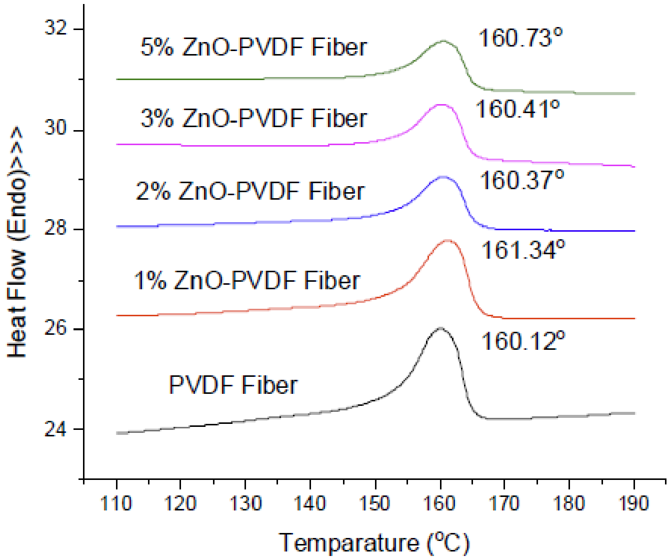

Figure 3.7: DSC curves for PVDF and ZnO-PVDF fiber meshes

Table 3.3: Enthalpy and % crystallinity values obtained from the differential scanning calorimetry (DSC) curves.

Sample	T_m (°C)	ΔH (J/g)	Corrected ΔH (J/g)	X_c (%)
PVDF	160.12	19.70	19.70	19.05
1% ZnO-PVDF	161.34	20.13	19.93	19.27
3% ZnO-PVDF	160.41	20.72	20.10	19.44
5% ZnO-PVDF	160.73	21.25	20.18	19.51

3.3.5 Piezoelectric Coefficient (d_{33}) Test

The piezoelectric coefficient (d_{33}) of a material is the parameter that designates the strength of the piezoelectric effect of that material. The larger the d_{33} value, the better piezoelectric effect [46]. Table 3.2 represents the magnitude of piezoelectric coefficient (d_{33}) of the PVDF fiber meshes as a function of ZnO mass fraction. The d_{33} of PVDF mesh was 32 pC/N and it increased to 56 pC/N as ZnO increased to 5% mass ratio reflecting a 75% increase. The combination of the β phase of the fiber and the bulk ZnO nanoparticles contributed to an increase in d_{33} with a single step electrospun textile [30,37].

3.3.6 Electrochemical Impedance Spectroscopy (EIS)

As indicated previously, the sensor viability was determined through a comparison of the measurements done on the coating in an EIS conventional setup, referred to Configuration A, versus a modified three electrode setup to extract sensor data named Configuration B. EIS testing was done for all the samples in 4.2% sea salt solution immediately after completing the coating using Configuration A to study the impact of embedding the sensor into the coating. The impedance |Z| increased significantly both at low frequency (100 mHz) and high frequency (10 kHz) after adding PVDF mesh in between two layers of coating compared to double layer epoxy coating. The impedance increased even further after introducing ZnO into the fiber meshes as shown in Figure 3.8. This indicates that while |Z| increases with the presence of ZnO the resistance and capacitance contributions require additional analysis through evaluation of an equivalent circuit.

The EIS data were analyzed using EC-Lab employing the electrical circuit model validated previously for insulative coatings [47] is shown in Figure 3.9 where R_s represents the solution resistance, R_{pore} and CPE_{pore} correspond to the pore resistance and pore capacitance of the coating while the R_{ct} and CPE_{dl} are the charge transfer resistance and double layer capacitance of the system, respectively.

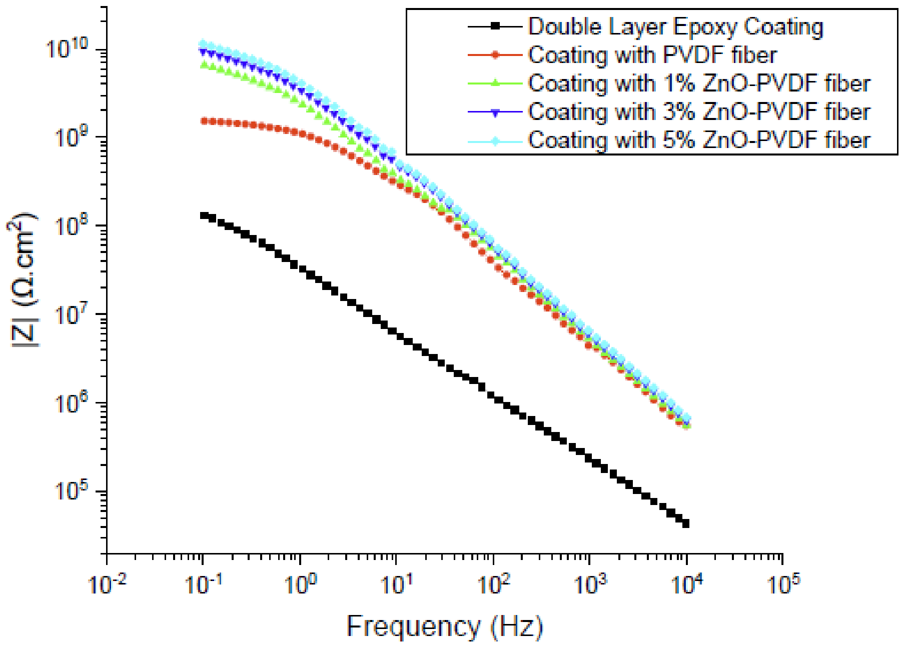

Figure 3.8: Bode magnitude plot for all samples on Day 0 in 4.2% sea salt solution

Constant phase element, CPE, is used instead of a pure capacitor in the model to take into account the deviations from ideal dielectric behavior related to surface heterogeneity and its impedance at constant phase angle is given by $Z_{CPE} = Z_0/(j\omega)^n$, where n and Z_0 are constant [48].

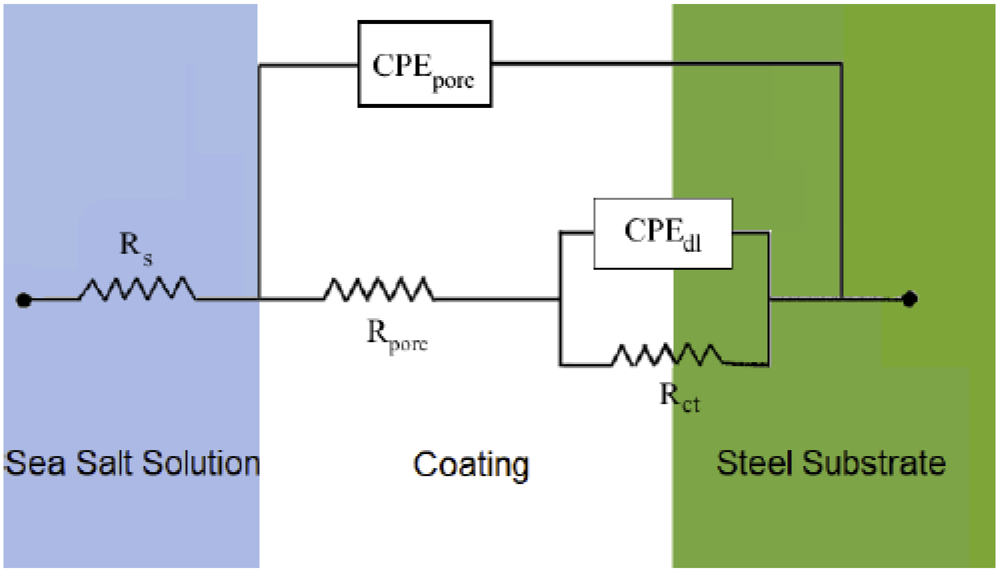

Figure 3.9: Equivalent Circuit from EIS data

The capacitance element CPE will be pure capacitor when n =1 and will be pure resistor when n = 0. The fitted values were extracted and shown in Table 3.4 which were consistent with the Bode Plot (Figure 3.8) A low χ2 value indicated the goodness of the curve fitting. All circuit parameters (R_{ct}, R_{pore}, C_{pore} and C_{dl}) increased considerably for nanoparticle content of 1 and 3% ZnO. However, using further nanoparticles (5% ZnO) did not cause significant changes which is also evident from the Bode Plot (Figure 3.8).

Table 3.4: Equivalent circuit parameters immediately after coating

Sample	R_s (μΩ)	R_{pore} (MΩ)	CPE_{pore}		R_{ct} (GΩ)	CPE_{dl}		$\chi^2(E^{-2})$
			C_{pore}(pF)	n_{pore}		C_{dl}(μF)	n_{dl}	
Epoxy coating	3.59	0.23	5.77	0.91	0.11	0.35	0.89	0.29
Coating with PVDF fiber	2.64	2.34	6.24	0.87	1.32	2.96	0.83	4.62
Coating with 1% ZnO-PVDF fiber	3.47	4.73	8.79	0.89	5.15	4.91	0.92	3.45
Coating with 3% ZnO-PVDF fiber	1.85	7.21	9.93	0.90	8.22	5.21	0.90	9.94
Coating with 5% ZnO-PVDF fiber	2.25	7.94	10.45	0.88	9.78	6.03	0.89	5.59

To establish the viability of real-time monitoring, measurements were conducted over time with continued immersion in a 4.2% sea salt water solution. The coated samples were submersed in 4.2% sea salt solution for 10 days to perform EIS testing using Configurations A and B. The Bode magnitude plots associated with Configuration A and B are shown in Figure 3.10 and 3.11. The EIS shows a plateau region while transitioning from a high to low frequency. This becomes more apparent on day 7 and beyond. This indicates that the onset of corrosion has begun and was captured by the sensor textile as well as by the instrument electrode. Similar trends are also found for all the Nyquist plots. They exhibited a partial capacitive loop, indicating that all epoxy coatings provide good initial corrosion protection. As the days progressed, the loop diameters dropped indicating the change transfer and pore resistance value were decreasing. The EIS data associated with Configurations A and B show that of the electrochemical equivalent circuit parameters, R_{pore} was the most vital parameter in this model circuit as R_{pore} was the resistance of ion-conducting paths that developed in the coating after being exposed in a 4.2% sea salt solution for a long time. Reduction of R_{pore} indicated that the coating had started to degrade and this work aimed to sense it. The low frequency plateau after day 4 indicates that the direct current limit of the coating had been reached. The EEC parameters for the sensor textile (Configuration B) were compared to when the instrument was used as the sensor (Configuration A) by estimating the percent error of each parameter. For days 1 and 4, the error between instrument data in Configuration A and sensor data in Configuration B was less than 10%. The R_{pore} values obtained from Configurations A and B were consistent with a maximum error of 24.56% on day 10, which indicates that prior to the corrosive fluid reaching the sensor textile (day 4), the textile provided a higher accuracy. On days 7 and 10, following the permeation of the salt water to the sensor textile, the textile-salt water interaction had an impact on the net circuit accuracy. Another important circuit element is the charge transfer resistance (R_{ct}), which corresponds to the resistance to electron transfer from the steel substrate to salt solution. R_{ct} also showed a similar trend to that of R_{pore}, and dropped along with R_{pore} as the days of immersion increased. Data obtained from both Configurations A and B were consistent with a similar range of error noted in R_{pore}. Both the capacitance C_{pore} and C_{dl} increased over time, and data obtained from Configurations A and B were consistent with less than 10% error in all cases prior to the onset of corrosion (day 7), as shown in Table 3.5.

Table 3.5: Electrochemical equivalent circuit (EEC) parameters at different time and configuration.

Day	ZnO wt%	Conf.	$\chi^2(E^{-2})$	R_{pore} (MΩ)	R_{ct} (GΩ)	C_{pore} ($pF.s^{n-1}.cm^{-2}$)	C_{dl} ($\mu F.s^{n-1}.cm^{-2}$)	Error for R_{pore} (%)	Error for R_{ct} (%)	Error for C_{pore} (%)	Error for C_{ct} (%)
0	0	A	0.56	2.48 ± 0.13	1.35 ± 0.13	6.13 ± 0.51	2.79 ± 0.25	4.92	7.35	3.15	5.61
		B	0.95	2.36 ± 0.15	1.25 ± 0.11	5.94 ± 0.90	2.63 ± 0.25				
	1	A	1.75	5.21 ± 0.48	5.67 ± 0.52	6.21 ± 0.48	4.45 ± 0.45	4.58	4.80	2.97	3.94
		B	2.43	4.97 ± 0.59	5.40 ± 0.46	6.38 ± 1.24	4.23 ± 0.40				
	3	A	0.87	7.47 ± 1.05	8.51 ± 0.88	10.2 5 ±1.03	5.39 ± 0.56	4.02	3.92	5.06	6.67
		B	2.45	7.17 ± 0.46	8.18 ± 1.01	9.73 ± 0.57	5.03 ± 0.45				
	5	A	0.41	8.74 ± 0.79	10.76 ± 0.98	11.49 ± 1.04	6.63 ± 0.60	6.12	5.91	3.89	5.09
		B	1.27	8.32 ± 0.73	10.12 ± 0.64	11.05 ± 0.75	6.29 ± 0.44				
1	0	A	0.68	2.47 ± 0.17	1.40 ± 0.11	5.91 ± 0.47	2.74 ± 0.32	5.34	6.23	1.08	5.12
		B	1.87	2.34 ± 0.22	1.31 ± 0.14	5.92 ± 1.27	2.60 ± 0.35				
	1	A	0.76	5.21 ± 0.66	5.67 ± 0.73	6.21 ± 0.66	4.45 ± 0.63	4.35	3.27	1.88	2.83
		B	2.43	4.98 ± 0.49	5.48 ± 0.61	7.49 ± 1.72	4.29 ± 0.55				
	3	A	1.84	7.05 ± 0.29	8.02 ± 0.29	9.68 ± 0.35	5.08 ± 0.19	1.75	3.15	2.80	5.03
		B	1.43	6.93 ± 0.47	7.76 ± 0.53	9.41 ± 0.10	4.82 ± 0.38				
	5	A	0.92	8.34 ± 0.56	10.27 ± 0.69	10.97 ± 0.74	6.33 ± 0.43	3.93	4.82	3.20	5.96
		B	3.75	8.01 ± 0.70	9.78 ± 0.26	10.62 ± 0.20	6.08 ± 0.33				
4	0	A	2.54	2.31 ± 0.28	1.35 ± 0.08	6.41 ± 0.75	2.88 ± 0.26	6.54	6.19	5.56	6.01
		B	6.34	2.16 ± 0.18	1.27 ± 0.15	6.06 ± 1.07	2.71 ± 0.43				
	1	A	4.27	2.81 ± 0.36	4.52 ± 0.58	7.81 ± 0.36	4.58 ± 0.72	3.11	3.52	4.99	3.82
		B	3.76	2.72 ± 0.47	4.36 ± 0.34	9.46 ± 0.78	4.37 ± 0.57				

Day	ZnO wt%	Conf.	$\chi^2(E^{-2})$	R_{pore} (MΩ)	R_{ct} (GΩ)	C_{pore} ($pF.s^{n-1}.cm^{-2}$)	C_{dl} ($\mu F.s^{n-1}.cm^{-2}$)	Error for R_{pore} (%)	Error for R_{ct} (%)	Error for C_{pore} (%)	Error for C_{ct} (%)
	3	A	6.23	6.33 ± 0.24	7.72 ± 0.28	9.77 ± 0.36	5.39 ± 0.20	5.43	2.43	4.42	9.94
		B	8.34	5.99 ± 0.56	7.68 ± 0.10	9.34 ± 0.37	4.86 ± 0.19				
	5	A	3.16	6.82 ± 0.45	9.39 ± 0.63	11.36 ± 0.76	6.47 ± 0.43	6.14	4.41	3.70	5.23
		B	4.87	6.40 ± 0.42	8.97±0.17	10.94 ± 0.38	6.13 ± 0.20				
7	0	A	7.82	0.51 ± 0.55	0.31 ± 0.17	6.66 ± 0.81	3.08 ± 0.31	9.41	14.47	8.50	7.71
		B	7.56	1.46 ± 0.49	1.27 ± 0.17	6.10 ± 0.86	2.84 ± 0.40				
	1	A	6.92	1.44 ± 0.19	1.16 ± 0.85	8.44 ± 1.31	4.65 ± 0.72	2.70	11.97	3.21	10.82
		B	8.60	1.48 ± 0.10	1.02 ± 0.98	9.93 ± 0.30	4.03 ± 0.12				
	3	A	9.54	2.53 ± 0.09	4.67 ± 0.17	10.62 ± 0.39	6.28 ± 0.22	13.83	14.37	9.67	10.22
		B	8.81	2.18 ±0.33	3.99 ± 0.41	9.60 ± 0.59	5.64 ± 0.38				
	5	A	6.36	2.47 ± 0.16	5.24 ± 0.42	12.48 ± 0.84	7.07 ± 0.47	12.20	14.15	8.68	0.30
		B	8.92	2.17 ± 0.17	4.50 ± 0.71	11.40 ± 0.71	7.05 ± 0.13				
10	0	A	10.54	0.10 ± 0.05	0.15 ± 0.12	6.96 ± 0.82	3.15 ± 0.24	26.00	2.92	9.65	16.30
		B	12.65	0.07 ± 0.07	0.15 ± 0.08	6.28 ± 0.79	2.64 ± 0.49				
	1	A	9.56	0.09 ± 0.21	0.11 ± 0.22	8.81 ± 1.54	4.75 ± 1.74	17.03	12.47	3.93	14.67
		B	11.45	0.08 ± 0.39	0.10 ± 0.05	12.45 ± 3.56	3.91 ± 0.28				
	3	A	8.89	1.67 ± 0.24	1.02 ± 0.44	10.81 ± 0.39	7.08 ± 0.26	19.51	25.07	10.81	10.91
		B	11.56	1.34 ± 0.18	0.77 ± 0.12	9.65 ± 0.76	6.31 ± 0.35				
	5	A	10.54	1.78 ± 0.32	1.21 ± 0.28	12.80 ± 0.99	7.32 ± 0.49	24.70	16.04	9.71	15.36
		B	13.66	1.34 ± 0.19	1.02 ± 0.41	11.56 ± 0.67	6.20 ± 0.12				

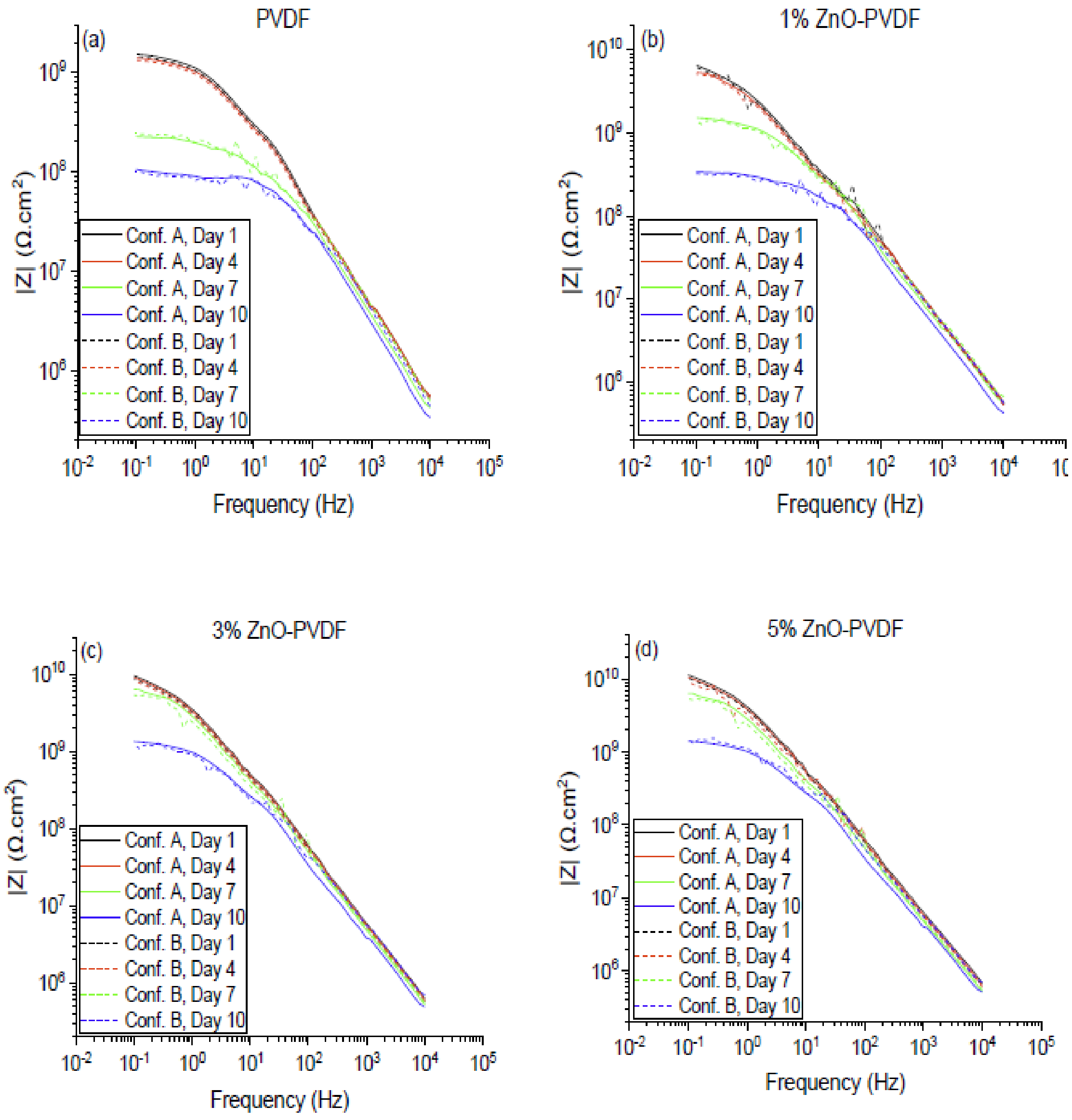

Figure 3.10: Instrument (solid lines) and sensor textile (dotted lines) Bode plots. (a) PVDF fiber, (b) 1% ZnO-PVDF fiber, (c) 3% ZnO-PVDF fiber, and (d) 5% ZnO-PVDF fiber.

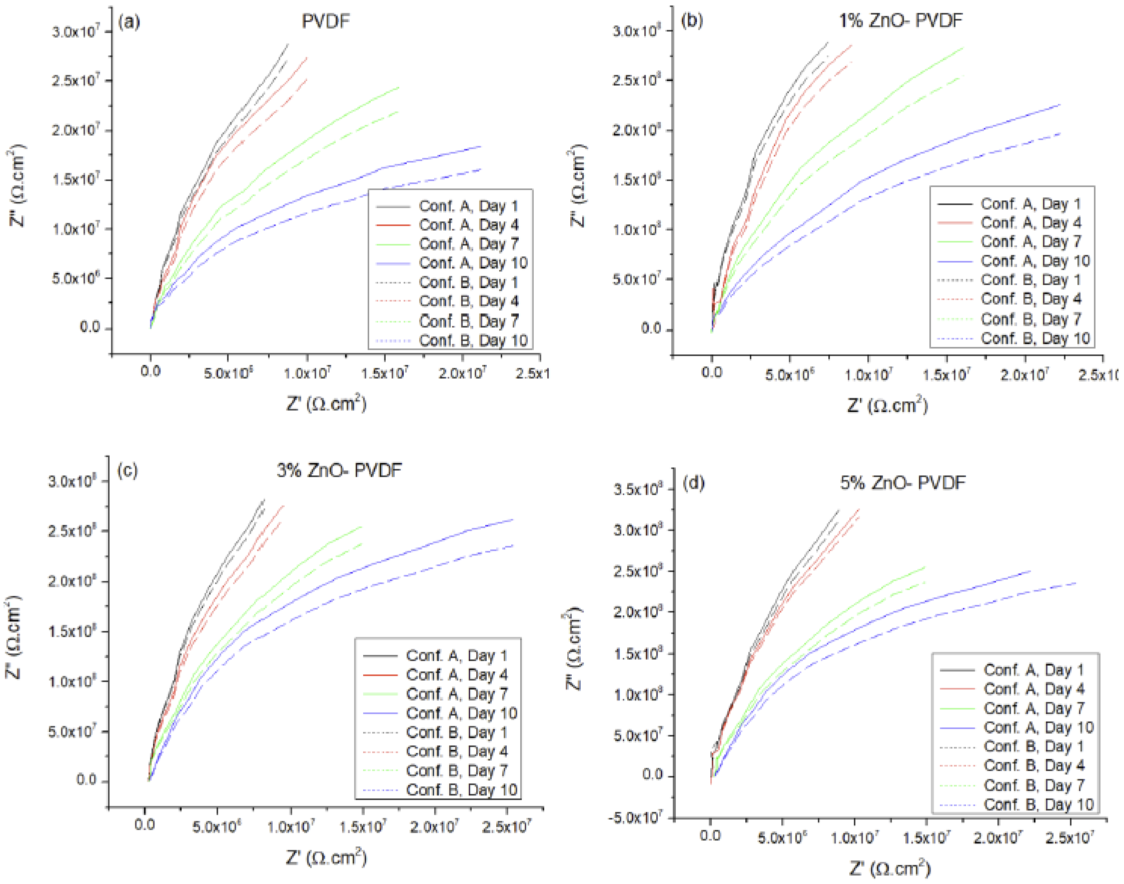

Figure 3.11: Instrument (solid lines) and sensor textile (dotted lines) nyquist plots. (a) PVDF fiber, (b) 1% ZnO-PVDF fiber, (c) 3% ZnO-PVDF fiber, and (d) 5% ZnO-PVDF fiber.

3.4 Conclusions

In this work, fiber meshes were investigated as potential embedded corrosion sensors in corrosion coatings. PVDF, a well-known sensor polymer, was modified with ZnO and formed into non-woven fiber meshes through electrospinning. No poling of the fiber meshes was required. The effect of the ZnO was to decrease the fiber diameter as the ZnO increased. XRD and FTIR indicated that the β phase of the meshes increased with ZnO presence. The mesh d_{33} increased with ZnO content. The mesh contributed positively to the polymer corrosion resistance with an increase in impedance as a function of ZnO. The effectiveness of the sensor was established by comparing the sensor as the reference electrode versus the instrument electrode using EIS over 10 days to evaluate pre-corrosion and post-corrosion effectiveness. The EIS results were analyzed using an electrochemical equivalent circuit. The coating resistance and coating-steel resistance increased with ZnO fraction and decreased with time. The capacitance of the coating and the capacitance at the coating–steel interface increased with ZnO and increased with time. Both trends were obtained in both the instrument data and the sensor textile data. This could be attributed to the contributions of ZnO to the PVDF in increased resistance and capacitance pre-corrosion as well as increased hydrophobicity from the presence of ZnO [50,51]. EIS data were compared and it was found that the actual data and sensor data were consistent with a less than 10% error up to day 4 when the permeation of the fluid through the coating was low. When the corrosion rate increased and coating degraded, the maximum error was recorded as 24.56% at day 10. This established the viability of the sensor textile. The results offer a low cost, novel approach to embedded sensors for chemical corrosion detection using a non-conductive sensor textile.

3.5 References

1. Augustyniak, A.; Tsavalas, J.; Ming, W. Early Detection of Steel Corrosion via "Turn-On" Fluorescence in Smart Epoxy Coatings. ACS Appl. Mater. Interfaces 2009, 1, 2618–2623. doi:10.1021/am900527s.

2. Koch, G.H.; Brongers, M.P.; Thompson, N.G.; Virmani, Y.P.; Payer, J.H. Corrosion Cost and Preventive Strategies in the United States. Office of Infrastructure Research and Development, Technical Report, FHWA-RD-01-156, Federal Highway Administration (FHWA), Department of Transportation (DOT) 2002-3. Link: https://rosap.ntl.bts.gov/view/dot/40697

3. Cole, I.S. 2-Smart coatings for corrosion protection: An overview. In Handbook of Smart Coatings for Materials Protection, Makhlouf, A.S.H., Ed; Woodhead Publishing: Sawston, UK, 2014; pp. 29–55. doi:org/10.1533/9780857096883.1.29

4. Cooper, G.L. Sensing probes and instruments for electrochemical and electrical resistance corrosion monitoring. In Corrosion Monitoring in Industrial Plants Using Nondestructive Testing and Electrochemical Methods; ASTM International: Conshohocken, PA, USA, 1986; pp. 237–250.

5. Feng, W.; Patel, S.H.; Young, M.Y.; Zunino Iii, J.L.; Xanthos, M. Smart polymeric coatings—recent advances. Adv. Polym. Tech. 2007, 26, 1–13, doi:10.1002/adv.20083.

6. Zhang, J.; Frankel, G.S. Corrosion-Sensing Behavior of an Acrylic-Based Coating System. CORROSION 1999, 55, 957–967, doi:10.5006/1.3283932.

7. Frankel, G.S.; Frankel, G.S.; Buchheit, R.G.; Zhang, J. Corrosion-sensing composition and method of use. US Patent 2003/0068824. April 2003. Link: https://patents.google.com/patent/US20030068824A1/en

8. Sibi, M.P.; Zong, Z. Determination of corrosion on aluminum alloy under protective coatings using fluorescent probes. Prog. Org. Coat. 2003, 47, 8–15, doi.org/10.1016/S0300-9440(02)00179-0.

9. Li, S.-m.; Zhang, H.-r.; Liu, J.-h. Preparation and performance of fluorescent sensing coating for monitoring corrosion of Al alloy 2024. Trans. Nonferrous Met. Soc. China 2006, 16, s159–s164, doi:org/10.1016/S1003-6326(06)60166-0.

10. Sottos, N.R.; White, S.R.; Li, W.; Matthews, C.C. Autonomic damage indication in coatings. US Patent 10,174,221 B2. January 2019. Link: https://patents.google.com/patent/US10174221B2/en

11. Leung, K.C.; Wan, T.K.; Chen, L. A Novel Optical Fiber Sensor for Steel Corrosion in Concrete Structures. Sensors 2008, 8, 1960–1976, doi:10.3390/s8031960.

12. Cooper, K.R.; Elster, J.; Jones, M.; Kelly, R.G. Optical fiber-based corrosion sensor systems for health monitoring of aging aircraft. In Proceedings of the 2001 IEEE Autotestcon Proceedings. IEEE Systems Readiness Technology Conference. (Cat. No.01CH37237), Valley Forge, PA, USA, 20–23 August 2001.

13. Ahmed, R.; Rifat, A.A.; Yetisen, A.K.; Salem, M.S.; Yun, S.-H.; Butt, H. Optical microring resonator based corrosion sensing. RSC Adv. 2016, 6, 56127–56133, doi:10.1039/C6RA11538A.

14. Zhang, N.; Chen, W.; Zheng, X.; Hu, W.; Gao, M. Optical Sensor for Steel [10] Corrosion Monitoring Based on Etched Fiber Bragg Grating Sputtered With Iron Film. IEEE Sens. J. 2015, 15, 3551–3556, doi:10.1109/JSEN.2015.2393559.

15. Da Silva Marques, R.; Prado, A.R.; Da Costa Antunes, P.F.; De Brito André, P.S.; Ribeiro, M.R.N.; Frizera-Neto, A.; Pontes, M.J. Corrosion Resistant FBG-Based Quasi-Distributed Sensor for Crude Oil Tank Dynamic Temperature Profile Monitoring. Sensors 2015, 15, 30693–30703, doi:10.3390/s151229811.

16. Li, S.; Kim, Y.-G.; Jung, S.; Song, H.-S.; Lee, S.-M. Application of steel thin film electrical resistance sensor for in situ corrosion monitoring. Sens. Actuators B 2007, 120, 368–377, doi: org/10.1016/j.snb.2006.02.029.

17. Qian, H.; Xu, D.; Du, C.; Zhang, D.; Li, X.; Huang, L.; Deng, L.; Tu, Y.; Mol, J.M.C.; Terryn, H.A. Dual-action smart coatings with a self-healing superhydrophobic surface and anti-corrosion properties. J. Mater. Chem. A 2017, 5, 2355–2364, doi:10.1039/C6TA10903A.

18. Cui, L.-Y.; Gao, S.-D.; Li, P.-P.; Zeng, R.-C.; Zhang, F.; Li, S.-Q.; Han, E.-H. Corrosion resistance of a self-healing micro-arc oxidation/polymethyltrimethoxysilane composite coating on magnesium alloy AZ31. Corros. Sci. 2017, 118, 84–95, doi:org/10.1016/j.corsci.2017.01.025.

19. Wei, H.; Wang, Y.; Guo, J.; Shen, N.Z.; Jiang, D.; Zhang, X.; Yan, X.; Zhu, J.; Wang, Q.; Shao, L.; et al. Advanced micro/nanocapsules for self-healing smart anticorrosion coatings. J. Mater. Chem. A 2015, 3, 469–480, doi:10.1039/C4TA04791E.

20. Behzadnasab, M.; Mirabedini, S.M.; Esfandeh, M.; Farnood, R.R. Evaluation of corrosion performance of a self-healing epoxy-based coating containing linseed oil-filled microcapsules via electrochemical impedance spectroscopy. Prog. Org. Coat. 2017, 105, 212–224, doi:org/10.1016/j.porgcoat.2017.01.006.

21. Qian, B.; Michailidis, M.; Bilton, M.; Hobson, T.; Zheng, Z.; Shchukin, D. Tannic complexes coated nanocontainers for controlled release of corrosion inhibitors in

self-healing coatings. Electrochim. Acta 2019, 297, 1035–1041, doi:org/10.1016/j.electacta.2018.12.062.

22. Cho, S.H.; White, S.R.; Braun, P.V. Self-healing polymer coatings. Adv. Mater. 2009, 21, 645–649.

23. Xia, D.-H.; Song, S.; Behnamian, Y.; Hu, W.; Cheng, F.; Luo, J.; Huet, F. Electrochemical Noise Applied in Corrosion Science: Theoretical and Mathematical Models towards Quantitative Analysis. J. Electrochem. Soc. 2020, 167, 081507.

24. Qi, X.; J Gelling, V. A review of different sensors applied to corrosion detection and monitoring. Recent Patents Corros. Sci. 2011, 1, 1–7.

25. Kittel, J.; Celati, N.; Keddam, M.; Takenouti, H. Influence of the coating–substrate interactions on the corrosion protection: characterisation by impedance spectroscopy of the inner and outer parts of a coating. Prog. Org. Coat. 2003, 46, 135–147.

26. Kittel, J.; Celati, N.; Keddam, M.; Takenouti, H. New methods for the study of organic coatings by EIS: New insights into attached and free films. Prog. Org. Coat. 2001, 41, 93–98.

27. Bierwagen, G.; Wang, X.; Tallman, D. In situ study of coatings using embedded electrodes for ENM measurements. Prog. Org. Coat 2003, 46, 163–175.

28. Su, Q.; Allahar, K.N.; Bierwagen, G.P. Application of embedded sensors in the thermal cycling of organic coatings. Corros. Sci. 2008, 50, 2381–2389.

29. Su, Q.; Allahar, K.; Bierwagen, G. Embedded electrode electrochemical noise monitoring of the corrosion beneath organic coatings induced by ac–dc–ac conditions. Electrochim. Acta 2008, 53, 2825–2830.

30. Allahar, K.N.; Upadhyay, V.; Bierwagen, G.P.; Gelling, V.J. Monitoring of a military vehicle coating under Prohesion exposure by embedded sensors. Prog. Org. Coat. 2009, 65, 142–151, doi:org/10.1016/j.porgcoat.2008.10.011.

31. Sorayani Bafqi, M.S.; Bagherzadeh, R.; Latifi, M. Fabrication of composite PVDF-ZnO nanofiber mats by electrospinning for energy scavenging application with enhanced efficiency. J. Polym. Res. 2015, 22, 130, doi:10.1007/s10965-015-0765-8.

32. Wu, H.; Huang, Y.; Xu, F.; Duan, Y.; Yin, Z. Energy Harvesters for Wearable and Stretchable Electronics: From Flexibility to Stretchability. Adv. Mater. 2016, 28, 9881–9919, doi:org/10.1002/adma.201602251

33. Ramesh, D.; D’Souza, N.A. One-step fabrication of biomimetic PVDF-BaTiO3 nanofibrous composite using DoE. Mater. Res. Express 2018, 5, 085308, doi:10.1088/2053-1591/aad156.

34. Randall, T.C.; Islam, S.K.; Mahbub, I.; McFarlane, N.; Yu, Y. A low-power, reconfigurable, pipelined ADC for implantable bioimpedance measurement system with vertically aligned carbon nanofibers (VACNF) electrodes. Analog Integr. Circuits Sign. Proces. 2016, 89, 139–149.

35. Cheng, K.-S.; Ko, Y.-F.; Wang, T. The Application of bioimpedance method for foot sole blood perfusion characterization. In Proceedings of the 2012 Sixth International Conference on Genetic and Evolutionary Computing, Kitakushu, Japan, 25–28 August 2012.

36. Lumbroso, R.; Naas, N.; Beitel, L.K.; Lawrence, M.F.; Trifiro, M.A. Novel bioimpedance sensor for glucose recognition. In Proceedings of the 2007 International Symposium on Signals, Systems and Electronics, Montreal, QC, Canada, 30 July–2 August 2007.

37. Bierwagen, G.P.; Allahar, K.N.; Su, Q.; Gelling, V.J. Electrochemically characterizing the ac–dc–ac accelerated test method using embedded electrodes. Corros. Sci. 2009, 51, 95–101, doi:org/10.1016/j.corsci.2008.09.023.

38. Mansouri, S.; Sheikholeslami, T.F.; Behzadmehr, A. Investigation on the electrospun PVDF/NP-ZnO nanofibers for application in environmental energy harvesting. J. Mater. Res. Technol. 2019, 8, 1608–1615, doi:org/10.1016/j.jmrt.2018.07.024.

39. Suyitno, S.; Purwanto, A.; Lullus Lambang G Hidayat, R.; Sholahudin, I.; Yusuf, M.; Huda, S.; Arifin, Z. Fabrication and characterization of zinc oxide-based electrospun nanofibers for mechanical energy harvesting. J. Nanotechnol. Eng. Med. 2014, 5, 011002–011008.

40. Athauda, T.J.; Butt, U.; Ozer, R.R. One-dimensional hierarchical composite materials based on ZnO nanowires and electrospun blend nanofibers. RSC Adv. 2013, 3, 21431–21438, doi:10.1039/C3RA43672A.

41. Sun, B.; Li, X.; Zhao, R.; Ji, H.; Qiu, J.; Zhang, N.; He, D.; Wang, C. Electrospun poly (vinylidene fluoride)-zinc oxide hierarchical composite fiber membrane as piezoelectric acoustoelectric nanogenerator. J. Mater. Sci. 2019, 54, 2754–2762.

42. Kim, M.; Wu, Y.; Kan, E.; Fan, J. Breathable and Flexible Piezoelectric ZnO@PVDF Fibrous Nanogenerator for Wearable Applications. Polymers 2018, 10, 745, doi:10.3390/polym10070745.

43. Bormashenko, Y.; Pogreb, R.; Stanevsky, O.; Bormashenko, E. Vibrational spectrum of PVDF and its interpretation. Polym. Test. 2004, 23, 791–796, doi:org/10.1016/j.polymertesting.2004.04.001.

44. Salimi, A.; Yousefi, A.A. Analysis Method: FTIR studies of β-phase crystal formation in stretched PVDF films. Polym. Test. 2003, 22, 699–704, doi:org/10.1016/S0142-9418(03)00003-5.

45. Satapathy, S.; Pawar, S.; Gupta, P.K.; Varma, K.B.R. Effect of annealing on phase transition in poly(vinylidene fluoride) films prepared using polar solvent. Bull. Mater. Sci. 2011, 34, 727, doi:10.1007/s12034-011-0187-0.

46. Choi, S.-S.; Lee, Y.S.; Joo, C.W.; Lee, S.G.; Park, J.K.; Han, K.-S. Electrospun PVDF nanofiber web as polymer electrolyte or separator. Electrochim. Acta 2004, 50, 339–343, doi:org/10.1016/j.electacta.2004.03.057.

47. Zhao, P.; Wang, S.; Kadlec, A. Piezoelectric and dielectric properties of nanoporous polyvinylidence fluoride (PVDF) films. In Proceedings of the Behavior and Mechanics of Multifunctional Materials and Composites. Las Vegas, NV, USA, 18 April 2016; doi:org/10.1117/12.2218896

48. Amirudin, A.; Thieny, D. Application of electrochemical impedance spectroscopy to study the degradation of polymer-coated metals. Prog. Org. Coat. 1995, 26, 1–28, doi:org/10.1016/0300-9440(95)00581-1.

49. Chang, J.; Liang, G.; Gu, A.; Cai, S.; Yuan, L. The production of carbon nanotube/epoxy composites with a very high dielectric constant and low dielectric loss by microwave curing. Carbon 2012, 50, 689–698, doi:org/10.1016/j.carbon.2011.09.029.

50. Zhang, X.; Si, Y.; Mo, J.; Guo, Z. Robust micro-nanoscale flowerlike ZnO/epoxy resin superhydrophobic coating with rapid healing ability. Chem. Eng. J. 2017, 313, 1152–1159, doi:org/10.1016/j.cej.2016.11.014.

51. Hu, C.; Li, Y.; Kong, Y.; Ding, Y. Preparation of poly(o-toluidine)/nano ZnO/epoxy composite coating and evaluation of its corrosion resistance properties. Synth. Met. 2016, 214, 62–70, doi:org/10.1016/j.synthmet.2016.01.021.

CHAPTER 4

RELIABILITY OF THE CORROSION SENSOR*

4.1 Introduction

Metals have a tendency to corrode upon exposure to the environment especially where there is a high moisture content. The situation becomes worse in the case of the submerged steel pipes subjected to corrosive salt-water. Organic coatings serve as a barrier between the metal substrate and surrounding environment to reduce the transport of moisture, water and ionic species to the metal substrate [1]. However, after being exposed to the corrosive environment for a long time, these organic coatings start degrading and cause corrosion of the metal. Corrosion sensors have been investigated using an embedded electrode or sensor placed in the coating to measure changes in the electrochemical properties [2-5]. Researchers have embedded platinum, gold, and nickel sensor layers at the metal coating interface to measure the electrochemical impedance real time [5-11]. A major drawback in such a system is the corrosion of the sensing element itself as they are also metallic. Moreover, cost becomes a concern for wide area application and measurement of the corrosion response. To overcome these limitations, a cheap non-conductive sensing material is highly desired in order to detect corrosion without being corroded. In our previous work, we have shown that non-conductive ZnO-PVDF nanocomposite nonwoven textile, fabricated from electrospinning method, could be used as embedded sensor to sense corrosion under organic coating after it was immersed into sea salt solution [12]. The textile was found to

---

* This chapter is reproduced from Chowdhury, T.; D'Souza, N.; Dahotre, N.; Low-cost Reliable Corrosion Sensors Using ZnO-PVDF Nano-composite Textiles. Submitted to Nanocomposite Sensors 2021 (under review). MDPI journal articles are published under Creative Commons CC BY license; authors retain copyright.

offer two benefits. First, it performed well as a sensor and the impedance matched that of an external calibrated corrosion instrument. Second, the presence of the textile improved the corrosion performance of the coating by increasing corrosion resistance. In this paper, we investigate long term reliability of the sensor through accelerated aging and impact of the coating glass transition on it's performance.

Long term reliability of corrosion sensors could be best determined by examination of the sensor in actual service condition. However, the time for degradation of insulative coatings having slow diffusion rates renders that option impractical. To counter that, accelerated methods such as Prohesion or salt-fog have been introduced which can simulate coating service conditions and promote failure in shorter times. Yet, it takes months to make little changes in some coating systems such as polyurethane/epoxy primer coating as reported by Allahar and Birrwagen which brings the requirements of a new accelerated system [13,14]. The thermal cycling method has emerged as a means to promote coating failure by exposing the coated panels to cyclic temperature changes under constant immersion as an accelerated approach. The method involves heating the coating to an elevated temperature followed by cooling to room temperature with monitoring of impedance changes through each transition. When the temperature reaches around the glass transition temperature (T_g) of the coating or higher, it's lifetime shortens drastically. Researchers have determined that thermal cycling induces irreversible changes on the coatings and observing these irreversible degradation of coating properties is the indicator of coating failures [15,16]. These failures in the coatings have similar degradation mechanisms as the changes caused by natural atmospheric conditions [15,17-20].

In this paper, a non-conductive sensing textile, ZnO-PVDF mesh, was used as an embedded sensor to overcome the limits of the highly conductive sensing elements which amplify the corrosion of the pipe. To test the reliability of the sensor, accelerated thermal cycling method was used under constant immersion in 4.2% sea salt solution. The plasticization effect of electrolyte solution on epoxy coating is minimal at temperatures well below T_g, leading to slow diffusion and permeation of the corrosive fluid. As the temperature of the epoxy coating approaches the T_g plasticization effect can no longer be ignored as diffusion for the permeating fluid increase decreasing corrosion resistance significantly. Thus in the thermal cycling method was designed for the set temperature reaches around the T_g of the epoxy coating. We note that the sensor textile polymer, PVDF, has a T_g of around 160 ˚C which is much higher than that of epoxy coating (57 ˚C) indicating that the sensor should not be affected by temperature increase around the T_g of epoxy coating. Moreover, ZnO is hydrophobic and thermally stable nanoparticle which is used as filler material in composite sensor textile [21,22]. Embedding ZnO-PVDF in between two layer of epoxy coating should not only sense the corrosion data but also reduce plasticization effect due to its superior thermal and hydrophobic properties. EIS testing was done for the textile as a stand-alone system as well as embedded at the coating-metal interface to evaluate the performance of a standard epoxy coating along with the sensor's capability of sensing corrosion when exposed to thermal cycling method. Reversibility, temperature dependence of the barrier property of the coating along with its activation energy werecalculated at different temperatures to study the effect of adding ZnO nanoparticles into the sensor.

4.2 Materials and Method

ZnO-PVDF fiber mats were fabricated using the electrospinning process. To prepare the corrosion sensor sample, first the steel coupons were coated with epoxy coating with a thickness of 120 ± 10 μm. Then the ZnO-PVDF fiber mat was placed on the coating with copper core electrical wire connected to it followed by second layer of same epoxy coating (120 ± 10 μm) as shown in Figure 4.1. The electrospinning process and corrosion sample preparation process has been described in our previous work [12]. To establish validity of the sensor, EIS testing was done on two different configurations to confirm accuracy of the textile as a sensor: Configuration A and Configuration B. In Configuration A the coated steel substrate operated as a working electrode (WE), Pt mesh as counter electrode (CE), and Ag/AgCl as reference electrode (RE) whereas the steel substrate worked as WE, Pt mesh as CE, and sensor textile as the RE in the Configuration B.

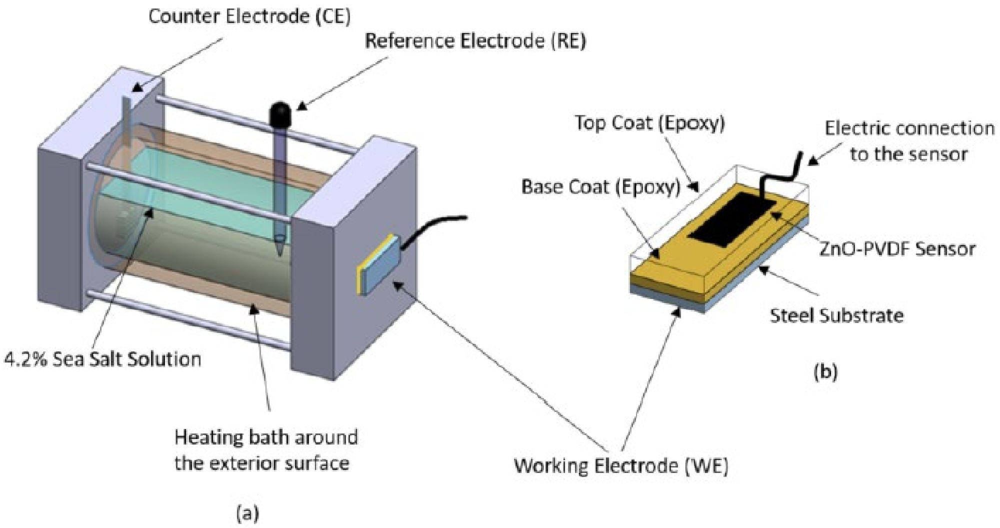

Figure 4.1: Schematic diagram of (a) electrochemical impedance spectroscopy (EIS) experimental setup with a double jacket corrosion cell and (b) corrosion sample with embedded sensor.

Configuration A (actual data) setup: steel substrate is WE, Pt mesh is CE, and Ag/AgCl is RE and Configuration B (sensor data) setup: steel substrate is WE, Pt mesh is CE, and sensor is RE.

4.2.1 Thermal Cycling Method

The thermal cycling experiment was conducted using a flat corrosion testing cell obtained from Biologic which had a double jacket for temperature control. First, the coated panel was immersed in 4.2% sea salt solution at room temperature for 1 day until a steady state was reached after which the thermal cycling started. The thermal cycle method consisted of nine cycles with three different set temperatures (35, 45, and 55 ˚C or (T_g -20 ˚C), (T_g -10 ˚C) and T_g) as shown in Figure 4.2(a). Three cycles were run at each set temperatures of 35, 45, and 55 ˚C and each cycle consisted of two EIS measurements: one at room temperature and another at set temperature. For example, cycle 1 consisted of EIS testing at room temperature (M-1), heating to the set temperature of 35 ˚C, holding at this set temperature for 1 hr for equilibration, then EIS testing (M-2), and then allowed to cool down to room temperature by exposure to ambient conditions for 23 hrs as shown in Figure 4.2(b) and Table 4.1. The temperature increase was accomplished using a heating bath around the exterior surface of the cell. The area being sampled was 1 cm^2.

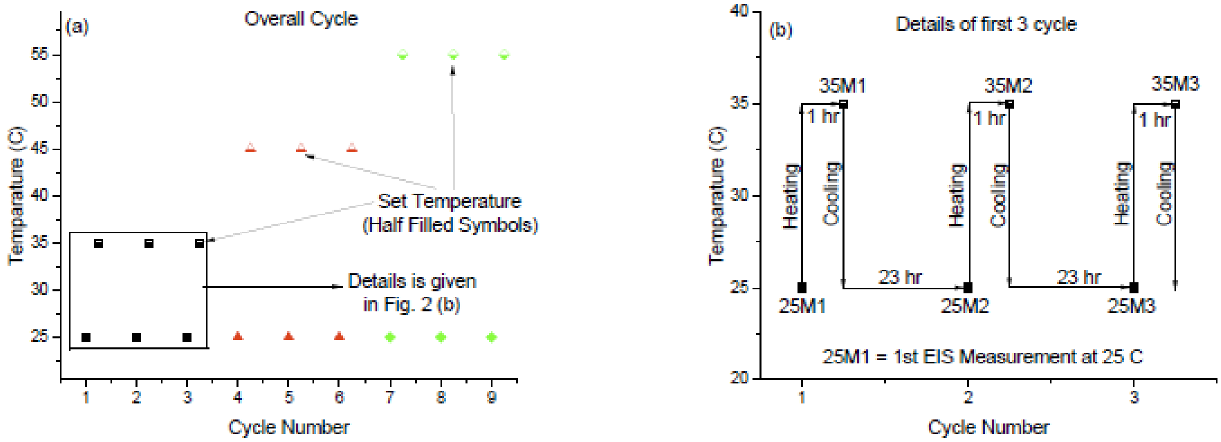

Figure 4.2: Schematic of thermal cycling method: (a) temperature as function of cycle number used in experiment and (b) detail experimental procedure for first 3 cycles.

Table 4.1: Indexing the EIS measurement at different time of thermal cycling method

Index	Meaning
M-1, M-3, M-5	EIS measurement at room temperature when set temperature is 35 ˚C (T_g -20 ˚C)
M-7, M-9, M-11	EIS measurement at room temperature when set temperature is 45 ˚C (T_g -10 ˚C)
M-13, M-15, M-17	EIS measurement at room temperature when set temperature is 55 ˚C (T_g)
M-2, M-4, M-6	EIS measurement at set temperature of 35 ˚C (T_g -20 ˚C)
M-8, M-10, M-12	EIS measurement at set temperature of 45 ˚C (T_g -10 ˚C)
M-14, M-16, M-18	EIS measurement at set temperature of 55 ˚C (T_g)

4.3 Results and Discussion

4.3.1 EIS Results

In order to determine the efficiency of the sensor in real-time monitoring, corrosion was induced through thermal cycling method which involved exposing the coating to alternating room temperature and higher temperature (T_g -20 ˚C, T_g -10 ˚C and T_g) cycles to perform EIS testing using Configurations A and B. The Bode plot associated with Configuration A and B of the topcoat/basecoat system with different sensors are shown in Figure 4.3 and 4.4. In these figures, the 25 ˚C data is associated with cycle 2 (M-3), while the set temperature data are associated with the second of the three cycles that the coating was exposed to for a given set temperature (M-4, M-10 and M-16). At 25 ˚C (T_g - 30 ˚C), the impedance value |Z| of PVDF, 1% ZnO-PVDF, 3% ZnO-PVDF and 5% ZnO-PVDF fiber embedded samples are 1.53 GΩ, 6.55 GΩ, 9.24 GΩ and 11.3 GΩ respectively, indicating a sharp increase in corrosion resistance after adding ZnO into the fiber. This is due to the addition of hydrophobic ZnO to PVDF fiber which increased the resistance and capacitance of the coating [21,23].

On the other hand, the EIS data of set temperatures shows a plateau region while transitioning from high to low frequency. This becomes more apparent at 45 ˚C (T_g - 20 ˚C) and above temperatures. This indicated that corrosion resistance (e.g. pore and charge transfer resistance) of the coating started degrading significantly after exposing it to T_g - 20 ˚C. Normally, the electrolytic solution has a plasticization effect in the polymer which induces a decrease of the glass transition temperature (T_g), and allows a faster water intake within the coating that drastically reduces the corrosion resistance [15,16]. At T_g - 20 ˚C, the epoxy started plasticizing and accumulated more water in it, thereby reduced the corrosion resistance. Similarly, the plateau region became more dominant for 55 ˚C (T_g) data which is consistent with previous discussion. The overlay of the Bode plots of Configuration A and B also showed similar trends indicating the efficiency of the sensor. Similar patterns can be seen in all of the Nyquist plots. They showed a partial capacitive loop, showing that all epoxy coatings provide strong initial corrosion resistance. As time passed, the loop diameters shrank, showing that the change transfer and pore resistance values were dropping. For additional analysis, the EIS data was fitted into an electrochemical equivalent circuit (EES) using EC-Lab software, as shown in Figure 4.5, which was previously validated for insulative coatings [24,25]. In this proposed electrochemical equivalent circuit, R_s is the solution resistance, R_{pore}, CPE_{pore}, R_{ct} and CPE_{dl} are the pore resistance, pore capacitance, charge transfer resistance and double layer capacitance of the system, respectively. The average of the fitted value of all the EIS measurement for each parameter is listed in Table 4.2 and found to be consistent with the Bode magnitude plot as shown in Figure 4.3. The chi-square (χ2) from the fitting results were on the order of 10^{-2}, indicating the goodness of the curve fitting. The R_{pore} values obtained from Configuration A and B were consistent with a maximum error of 27.12% at T_g. For T_g - 20 ˚C and T_g - 10 ˚C, the error between instrument data in Configuration A and sensor data in Configuration B was less than 10% except for PVDF. This indicates that prior to the corrosive fluid reaching the sensor textile (T_g), the textile provides a higher accuracy. On T_g - 20 ˚C and T_g - 10 ˚C, following the permeation of the salt water to the sensor textile, the textile-salt water interaction impacts the net circuit parameter accuracy. R_{ct} also showed similar trend to that of R_{pore}. It dropped along with R_{pore} as the cycle progressed and data obtained from both Configuration A and B were consistent with a similar range of error noted in R_{pore}. Both the capacitance C_{pore} and C_{dl} increased over the time and data obtained from Configuration A and B were consistent with less than 20% error in all cases as shown in Table 4.2. It is also notable that the error between the sensor data and actual data reduced as the concentration of the ZnO increased in PVDF fiber mats, indicating an improvement in the reliability of the sensor.

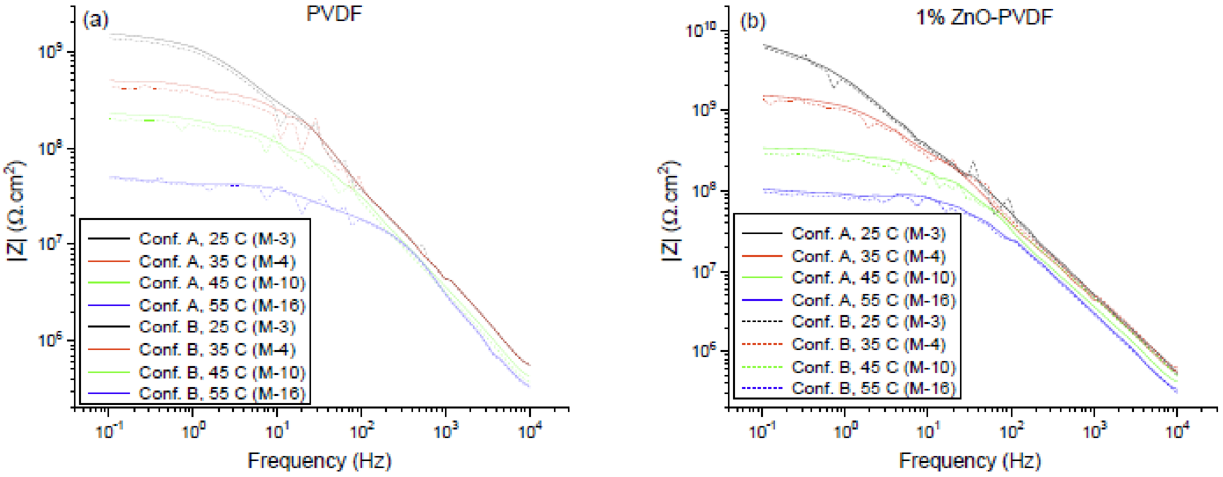

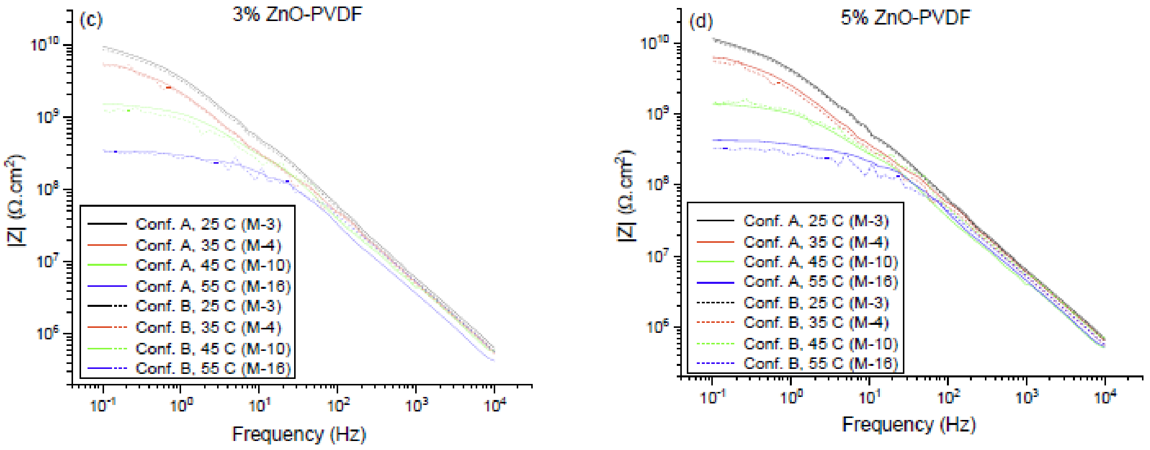

Figure 4.3: Bode magnitude plots at different temperature of (a) PVDF fiber, (b) 1% ZnO-PVDF fiber, (c) 3% ZnO-PVDF fiber and (d) 5% ZnO-PVDF fiber. Solid line is associated with the instrument data and dotted line represents the sensor data.

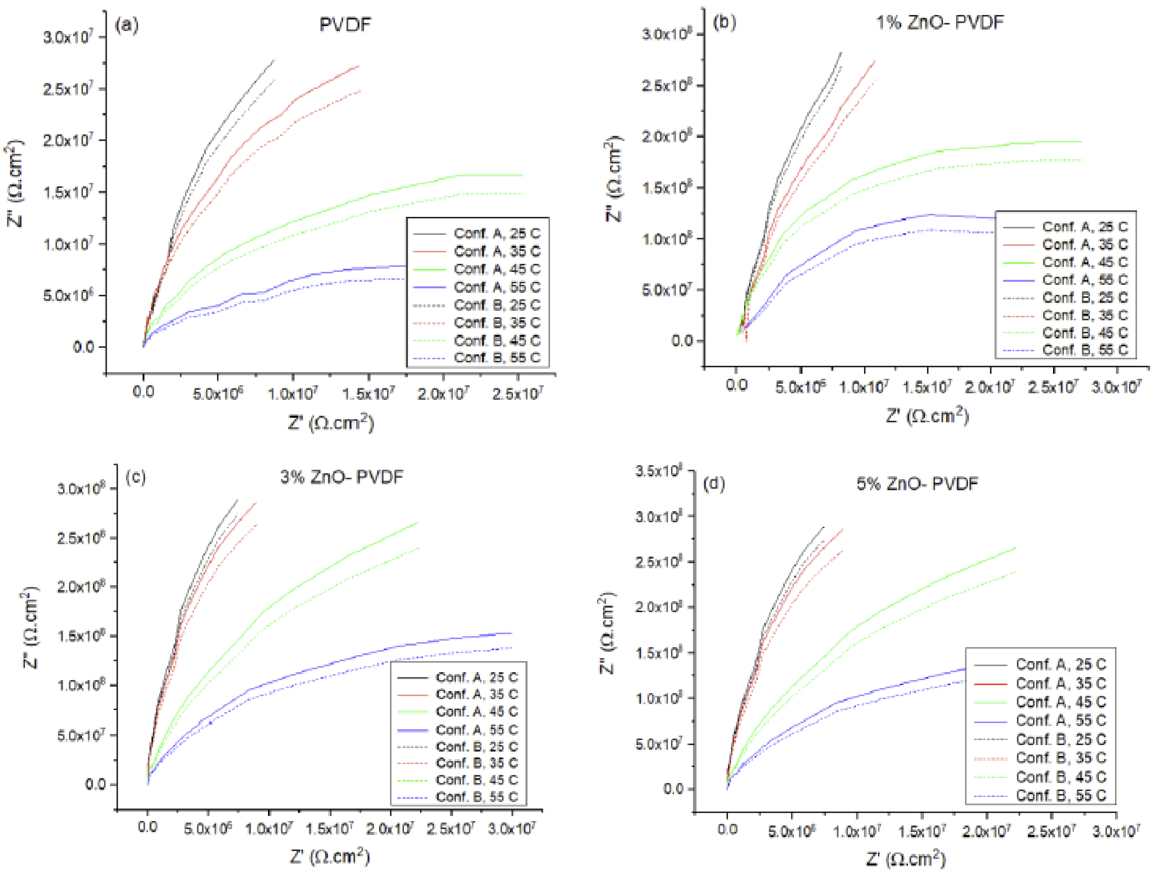

Figure 4.4: Nyquist plots at different temperature of (a) PVDF fiber, (b) 1% ZnO-PVDF fiber, (c) 3% ZnO-PVDF fiber and (d) 5% ZnO-PVDF fiber. Solid line is associated with the instrument data and dotted line represents the sensor data.

Table 4.2: Electrochemical equivalent circuit parameters at different temperatures and configurations. 25 ˚C data is accociated to M-1, M-3, M-5, 35 ˚C to M-2, M-4, M-6, 45 ˚C to M-8, M-10, M-12, and 55 ˚C to M-14, M-16, M-18.

Sample	Conf.	$\chi^2(E^{-2})$	R_{pore} (MΩ)	R_{ct} (GΩ)	C_{pore} (pF.s^{n-1}.cm^{-2})	C_{dl} (μF.s^{n-1}.cm^{-2})	Error for R_{pore} (%)	Error for R_{ct} (%)	Error for C_{pore} (%)	Error for C_{ct} (%)
0%_ZnO_25C	A	0.23	2.47±0.17	1.40±0.11	5.92±0.12	2.74±0.16	5.34	6.23	1.08	5.12
	B	0.54	2.34±0.13	1.31±0.14	5.92±0.20	2.60±0.22				
0%_ZnO_35C	A	2.67	1.09±0.29	0.41±0.12	6.62±0.27	2.98±0.30	9.33	10.75	8.56	6.37
	B	5.86	1.01±0.37	0.37±0.25	6.28±0.38	2.79±0.43				
0%_ZnO_45C	A	5.23	0.28±0.79	0.11±0.87	6.91±0.51	3.15±0.55	17.71	19.09	9.11	9.40
	B	9.45	0.23±0.68	0.09±0.76	6.28±0.68	2.90±0.82				
0%_ZnO_55C	A	16.45	0.02±1.05	0.03±1.06	7.11±1.82	3.32±1.49	15.90	19.28	10.13	12.65
	B	25.43	0.01±1.11	0.01±1.01	6.39±1.79	2.90±1.95				
1%_ZnO_25C	A	0.43	5.21±0.25	5.67±0.23	5.21±0.05	5.45±0.08	4.35	3.27	1.88	2.83
	B	1.29	4.98±0.39	5.48±0.21	5.49±0.12	5.29±0.15				
1%_ZnO_35C	A	2.65	2.42±0.16	1.35±0.28	6.01±0.16	5.82±0.02	7.85	6.67	4.16	2.58
	B	5.32	2.23±0.27	1.26±0.14	5.76±0.08	5.67±0.57				
1%_ZnO_45C	A	6.65	1.23±0.59	0.25±0.55	6.38±0.81	5.97±0.72	7.57	9.70	8.62	4.02
	B	5.54	1.10±0.45	0.22±0.68	6.93±0.49	5.73±0.54				
1%_ZnO_55C	A	12.94	0.05±0.75	0.09±0.75	6.49±0.74	6.25±0.96	21.82	11.11	14.18	20.80
	B	18.65	0.04±0.79	0.08±0.89	7.41±0.49	4.95±0.79				
3%_ZnO_25C	A	0.87	7.05±0.29	8.02±0.15	9.68±0.08	5.68±0.22	1.75	3.15	2.80	5.03
	B	0.38	6.93±0.17	7.76±0.23	9.41±0.10	5.52±0.09				
3%_ZnO_35C	A	3.95	5.43±0.28	5.23±0.21	9.89±0.17	6.15±0.26	4.42	3.25	4.55	8.44
	B	5.71	5.19±0.37	5.06±0.35	9.44±0.15	6.26±0.29				

Sample	**Conf.**	**$\chi^2(E^{-2})$**	**R_{pore} (MΩ)**	**R_{ct} (GΩ)**	**C_{pore} (pF.s^{n-1}.cm^{-2})**	**C_{dl} (μF.s^{n-1}.cm^{-2})**	**Error for R_{pore} (%)**	**Error for R_{ct} (%)**	**Error for C_{pore} (%)**	**Error for C_{ct} (%)**
3%_ZnO_45C	A	7.51	1.93±0.19	1.37±0.27	10.81±0.34	6.69±0.52	8.95	8.14	9.16	10.51
	B	9.74	2.18±0.23	1.19±0.31	9.82±0.49	5.92±0.38				
3%_ZnO_55C	A	10.79	0.59±0.74	0.27±0.84	10.98±0.91	7.28±0.71	27.12	22.22	10.66	10.16
	B	13.75	0.43±0.87	0.21±0.72	9.81±0.69	6.54±0.65				
5%_ZnO_25C	A	0.76	8.34±0.16	10.27±0.19	10.97±0.24	6.33±0.03	3.93	4.82	3.20	5.96
	B	2.78	8.01±0.10	9.78±0.26	10.62±0.20	6.08±0.14				
5%_ZnO_35C	A	7.54	5.86±0.25	6.09±0.23	11.16±0.16	6.65±0.31	4.78	2.79	1.34	5.71
	B	3.96	5.58±0.22	5.92±0.17	11.01±0.28	6.27±0.20				
5%_ZnO_45C	A	6.87	2.28±0.36	2.01±0.41	12.62±0.54	7.24±0.47	9.84	9.95	8.56	6.35
	B	10.56	2.01±0.47	1.79±0.51	11.54±0.62	6.78±0.23				
5%_ZnO_55C	A	12.73	1.21±0.92	0.59±0.98	12.89±0.79	7.54±0.81	15.70	18.64	9.46	13.93
	B	11.69	1.02±0.89	0.48±0.91	11.67±0.65	6.49±0.77				

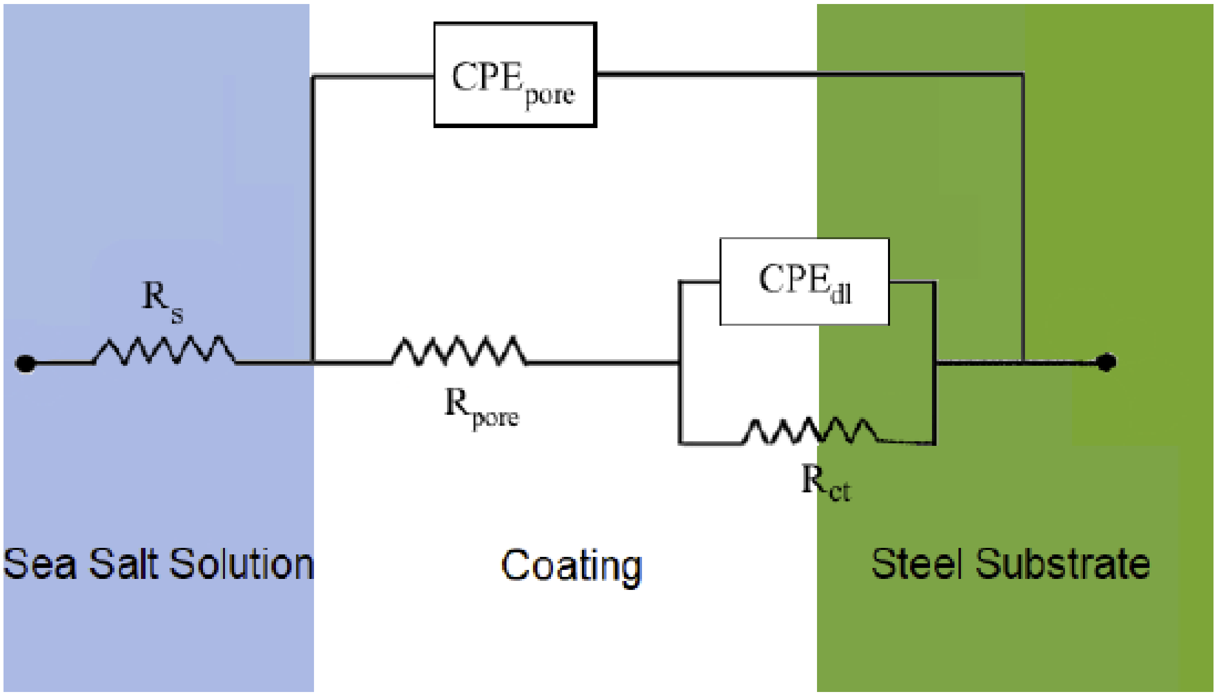

Figure 4.5: Electrochemical equivalent circuit from EIS data [12]

4.3.2 Reversibility

To better understand the failure process in the coating, a comprehensive study is conducted on the reversibility of the coating's barrier property as the irreversible changes in its barrier property is the indicator of coating failures [13]. The barrier property is linked to the d.c. resistance of the epoxy coating. A measure of this resistance is associated with the low frequency impedance modulus of the EIS data that approaches the d.c. limit [26]. The Bode magnitude plot shown in Fig 4.3, has a low frequency plateau which is indicative of the d.c. limit of the coating. The impedance at the lowest frequency was selected ($|Z|_{0.1\ Hz}$) from Bode plot to represent the barrier property of the epoxy coating systems for Configuration B. The $|Z|_{0.1\ Hz}$ values measured at 25 ˚C and at the set temperatures of the coating system are shown in Figure 4.6 as functions of cycle number.

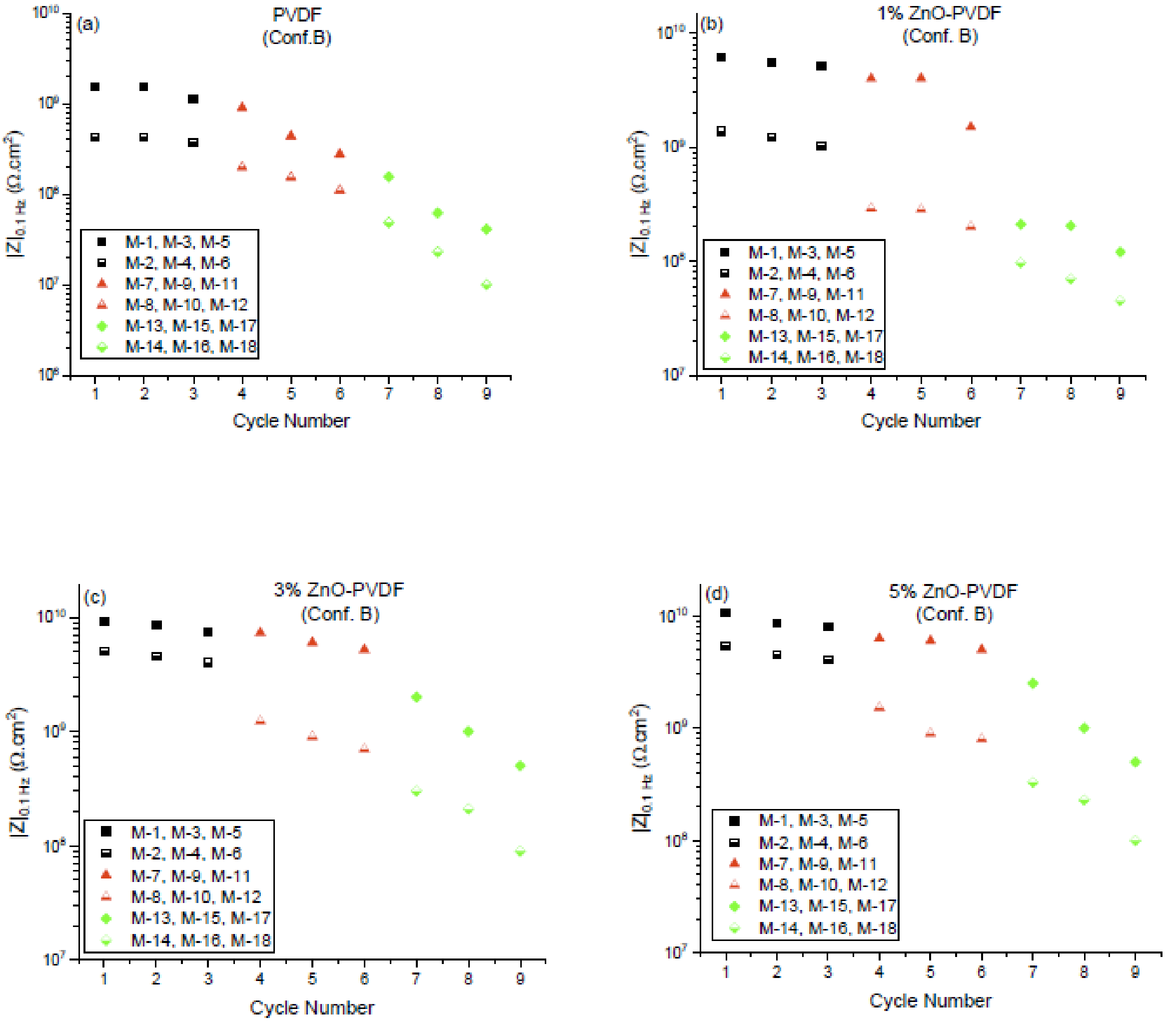

Figure 4.6: $|Z|_{0.1\text{ Hz}}$ values measured at room temperature and set temperatures as a function of thermal cycle number

For the of PVDF fiber embedded coating as shown in Figure 4.6(a), the $|Z|_{0.1\text{ Hz}}$ values at 25 ˚C were roughly same at 1.5 X 10^9 Ω.cm^2 for up to 4 cycles. So, the changes in impedance were induced by the increase in temperature though it was not permanent for up to 4 cycles. This showed the reversibility of the coating after being exposed to 35 ˚C (T_g - 20 ˚C) for three times and 45 ˚C (T_g - 10 ˚C) for single time. As no permanent damage was caused by the thermal cycling, the electrolytes that entered the topcoat/basecoat system were forced out when the mobility of polymer segments and the polymer free volume returned to their original states as the temperature returned to 25 ˚C [16]. The $|Z|_{0.1\ Hz}$ values for PVDF fiber embedded coating did not return to its initial value from 5 cycle rather it kept decreasing as the thermal cycle number progressed. This indicated that the reversibility of the coating was limited to a temperature as high as T_g - 20 ˚C. Thermal cycling above that temperature (T_g - 10 ˚C and T_g) was inducing permanent changes to the PVDF fiber embedded epoxy coating under constant immersion in 4.2% sea salt solution. When the ZnO was introduced in the PVDF fiber and embedded between two layers of coating, the permanent change in epoxy coating was also delayed to 6 cycle for 1% ZnO-PVDF, 7 cycle for both 3% ZnO-PVDF and 5% ZnO-PVDF instead of 5 cycle for PVDF fiber as shown in Fig 4.5(b, c and d). This happened due to the addition of thermally stable ZnO particles which improved the thermal properties of the coating and dropped the degradation rate [22,23,27]. $|Z|_{0.1\ Hz}$ values from Configuration B followed the same trend that of Configuration A.

4.3.3 Temperature Dependence of EIS Impedance

Temperature dependence of the impedance of the coatings embedded with different fiber sensors was evaluated by comparing their activation energy. The activation energies ware calculated using Equation 4.1 [8,28] from both Configuration A and B data under the assumption of Arrhenius behavior of the coatings.

$$|Z|_{0.1\,Hz} = A.exp\frac{E_a}{RT} \qquad \text{(Eq. 4.1)}$$

where $|\mathrm{Z}|_{0.1\ \mathrm{Hz}}$ is the impedance of the coating at 0.1 Hz, $\mathrm{E_a}$ is the activation energy, A is Arrhenius constant, T is the temperature in Kelvin and R is the universal gas constant. EIS impedance of the coatings |Z| at 0.1 Hz, measured from Configuration A and B (M-3, M-4, M-10, M-16) is shown in Figure 4.7 as a function of 1/T. There were observable linear relationships between the logarithmic values and 1/T for both configurations data indicating that the barrier properties were consistent with Arrhenius behavior. The glass transition temperature (T_g) can also be predicted by tracking the changes in slopes of |Z| vs. 1/T curves [29]. There was no visible change in slope for the data associated with both configurations, suggesting that the T_g of the coatings were below the values determined by DSC at dry state which was 57 ˚C [16]. This was consistent with the findings that the T_g of a coating can be reduced by plasticization when the coating is immersed in an electrolyte.

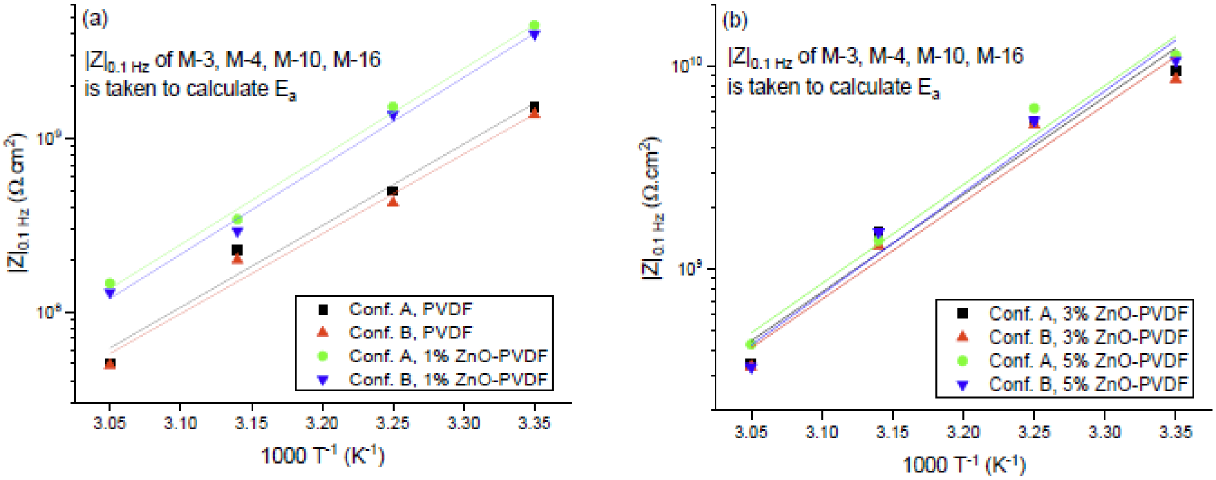

Figure 4.7: The low frequency impedance modulus ($|Z|_{0.1\ Hz}$) as a function of 1/T for (a) PVDF and 1% ZnO-PVDF, (b) 3% ZnO-PVDF and 5% ZnO-PVDF

Activation energy, E_a, is the minimum amount of energy that is required for atoms or molecules of a system to activate a chemical reaction or physical transport. The larger the E_a value, the better barrier property of the coating [30]. Table 4.3 lists the magnitude of E_a of the epoxy coatings from both configurations as a function of ZnO mass fraction in the embedded fibers. E_a of the epoxy coating embedded with PVDF mesh was 56.72 kJ.mol^{-1} and it increased to 62.23 kJ.mol^{-1} as ZnO increased to 5%

mass ratio in the fiber indicating that the coating became more stable against any chemical reaction or physical transport of corrosive fluid. Both the $\mathrm{E_a}$ values obtained from Configuration A and B were consistent with less than 1% error in all cases. It is to be noted that the activation energy is not significantly affected by the magnitude of ZnO in the textile showing that the epoxy (coating) permeability governs the sensor textile performance.

Table 4.3: Activation energy of different samples at different configurations

Sample	E_a from Conf. A (kJ.mol^{-1})	E_a from Conf. B (kJ.mol^{-1})	Error (%)
Coating with PVDF	56.72 ± 1.47	56.44 ± 1.38	0.49
Coating with 1% ZnO-PVDF	59.11 ± 2.21	58.84 ± 2.27	0.45
Coating with 3% ZnO-PVDF	61.94 ± 1.48	61.71 ± 1.46	0.37
Coating with 5% ZnO-PVDF	62.23 ± 1.42	61.99 ± 1.58	0.39

4.4 Conclusion

This paper investigated the reliability of the electrospun ZnO-PVDF mats as embedded corrosion sensor using accelerated corrosion testing. To accelerate the corrosion in the coating system, the thermal cycling method was used. The results showed that ZnO increases the accuracy of the sensor textile over the base PVDF while concurrently improving the impedance of the coating itself. From a vantage point of a sensor textile, the 3% ZnO-PVDF sensor was the most optimum showing a less than 10% deviation for temperatures Tg -20 ˚C and below. As the set temperature of thermal cycle approached to the Tg of the epoxy coating, the barrier property of the coating was damaged significantly and sensor reading deviated. The barrier protection of the coating was reversible up to Tg -30 ˚C and Tg -20 ˚C for PVDF fiber and ZnO-PVDF fiber embedded coating, respectively, after which coating stated to degrade and irreversible changes occurred. This change in reversibility could be attributed from using thermally stable and hydrophobic ZnO nanoparticles into PVDF matrix which improved thermal and barrier properties of the coating significantly by increasing the activation energy of the system. As a result of that, the addition of ZnO decreased the measurement error in sensor textile and improved coating's barrier property.

4.5 References

1. Augustyniak, A.; Tsavalas, J.; Ming, W. Early Detection of Steel Corrosion via "Turn-On" Fluorescence in Smart Epoxy Coatings. Acs Appl Mater Inter 2009, 1, 2618-2623, doi:10.1021/am900527s.
2. Bierwagen, G.P.; Allahar, K.N.; Su, Q.; Gelling, V.J. Electrochemically characterizing the ac–dc–ac accelerated test method using embedded electrodes. Corrosion Science 2009, 51, 95-101.
3. Bierwagen, G.; Wang, X.; Tallman, D. In situ study of coatings using embedded electrodes for ENM measurements. Progress in Organic Coatings 2003, 46, 163-175.
4. Kittel, J.; Celati, N.; Keddam, M.; Takenouti, H. New methods for the study of organic coatings by EIS: New insights into attached and free films. Progress in Organic Coatings 2001, 41, 93-98.
5. Kittel, J.; Celati, N.; Keddam, M.; Takenouti, H. Influence of the coating–substrate interactions on the corrosion protection: characterisation by impedance spectroscopy of the inner and outer parts of a coating. Progress in Organic Coatings 2003, 46, 135-147.
6. Kittel, J.; Celati, N.; Keddam, M.; Takenouti, H. New methods for the study of organic coatings by EIS: New insights into attached and free films. Progress in Organic Coatings 2001, 41, 93-98, doi:https://doi.org/10.1016/S0300-9440(00)00155-7.
7. Bierwagen, G.P.; Wang, X.; Tallman, D.E. In situ study of coatings using embedded electrodes for ENM measurements. Progress in Organic Coatings 2003, 46, 163-175, doi:https://doi.org/10.1016/S0300-9440(02)00186-8.
8. Su, Q.; Allahar, K.N.; Bierwagen, G.P. Application of embedded sensors in the thermal cycling of organic coatings. Corrosion Science 2008, 50, 2381-2389, doi:https://doi.org/10.1016/j.corsci.2008.06.010.

9. Su, Q.; Allahar, K.; Bierwagen, G. Embedded electrode electrochemical noise monitoring of the corrosion beneath organic coatings induced by ac–dc–ac conditions. Electrochimica Acta 2008, 53, 2825-2830, doi:https://doi.org/10.1016/j.electacta.2007.10.063.

10. Allahar, K.N.; Upadhyay, V.; Bierwagen, G.P.; Gelling, V.J. Monitoring of a military vehicle coating under Prohesion exposure by embedded sensors. Progress in Organic Coatings 2009, 65, 142-151.

11. Miszczyk, A.; Schauer, T. Electrochemical approach to evaluate the interlayer adhesion of organic coatings. Progress in Organic Coatings 2005, 52, 298-305.

12. Chowdhury, T.; D'Souza, N.; Ho, Y.H.; Dahotre, N.; Mahbub, I. Embedded Corrosion Sensing with ZnO-PVDF Sensor Textiles. Sensors 2020, 20, 3053.

13. Bierwagen, G.; Tallman, D.; Li, J.; He, L.; Jeffcoate, C. EIS studies of coated metals in accelerated exposure. Progress in Organic Coatings 2003, 46, 149-158, doi:https://doi.org/10.1016/S0300-9440(02)00222-9.

14. Allahar, K.N.; Su, Q.; Bierwagen, G.P. In situ monitoring of organic coatings under QUV/prohesion exposure by embedded sensors. Corrosion 2008, 64, 860-870.

15. Touzain, S.; Le Thu, Q.; Bonnet, G. Evaluation of thick organic coatings degradation in seawater using cathodic protection and thermally accelerated tests. Progress in Organic Coatings 2005, 52, 311-319.

16. Bierwagen, G.P.; He, L.; Li, J.; Ellingson, L.; Tallman, D. Studies of a new accelerated evaluation method for coating corrosion resistance—thermal cycling testing. Progress in organic coatings 2000, 39, 67-78.

17. Miszczyk, A.; Darowicki, K. Accelerated ageing of organic coating systems by thermal treatment. Corrosion science 2001, 43, 1337-1343.

18. Miszczyk, A.; Darowicki, K. Effect of environmental temperature variations on protective properties of organic coatings. Progress in organic coatings 2003, 46, 49-54.

19. Valentinelli, L.; Vogelsang, J.; Ochs, H.; Fedrizzi, L. Evaluation of barrier coatings by cycling testing. Progress in organic coatings 2002, 45, 405-413.

20. Richards, B.T.; Begley, M.R.; Wadley, H.N. Mechanisms of ytterbium monosilicate/mullite/silicon coating failure during thermal cycling in water vapor. Journal of the American Ceramic Society 2015, 98, 4066-4075.

21. Zhang, X.; Si, Y.; Mo, J.; Guo, Z. Robust micro-nanoscale flowerlike ZnO/epoxy resin superhydrophobic coating with rapid healing ability. Chem Eng J 2017, 313, 1152-1159.

22. Samad, U.A.; Alam, M.A.; Chafidz, A.; Al-Zahrani, S.M.; Alharthi, N.H. Enhancing mechanical properties of epoxy/polyaniline coating with addition of ZnO nanoparticles: Nanoindentation characterization. Progress in Organic Coatings 2018, 119, 109-115, doi:https://doi.org/10.1016/j.porgcoat.2018.02.018.

23. Hu, C.; Li, Y.; Kong, Y.; Ding, Y. Preparation of poly (o-toluidine)/nano ZnO/epoxy composite coating and evaluation of its corrosion resistance properties. Synthetic Metals 2016, 214, 62-70.

24. Amirudin, A.; Thieny, D. Application of electrochemical impedance spectroscopy to study the degradation of polymer-coated metals. Progress in Organic Coatings 1995, 26, 1-28, doi:https://doi.org/10.1016/0300-9440(95)00581-1.

25. Alsamuraee, A.M.A.; Jaafer, H.I. Electrochemical impedance spectroscopic evaluation of corrosion protection properties of polyurethane/polyvinyl chloride blend coatings on steel Abdulkareem Mohammed Ali Alsamuraee1, Harith Ibraheem Jaafer2, Hani Aziz Ameen3 and Ahmed Qasim Abdullah4. 2011.

26. Zhang, J.; Zhang, L.; Wilke, B.M.; Li, W.; Ning, C.; Chowdhury, T. Corrosion behaviour of microarc-oxidised magnesium alloy in Earle’s balanced salt solution. Surface Innovations 2017, 5, 43-53.

27. Ramezanzadeh, B.; Attar, M.M. Studying the corrosion resistance and hydrolytic degradation of an epoxy coating containing ZnO nanoparticles. Mater Chem Phys 2011, 130, 1208-1219, doi:https://doi.org/10.1016/j.matchemphys.2011.08.065.

28. Aneja, K.S.; Böhm, H.M.; Khanna, A.; Böhm, S. Functionalised graphene as a barrier against corrosion. FlatChem 2017, 1, 11-19.

29. Li, J.; Jeffcoate, C.; Bierwagen, G.; Mills, D.; Tallman, D. Thermal transition effects and electrochemical properties in organic coatings: part 1—initial studies on corrosion protective organic coatings. Corrosion 1998, 54, 763-771.

30. Sykes, J.M.; Whyte, E.P.; Yu, X.; Sharer Sahir, Z. Does “coating resistance” control corrosion? Progress in Organic Coatings 2017, 102, 82-87, doi:https://doi.org/10.1016/j.porgcoat.2016.04.015.

CHAPTER 5

DETECTION OF THE TYPE OF CORROSION (UNIFORM OR PITTING) IN STEEL PIPE BY ZnO-PVDF SENSOR TEXTILES

5.1 Introduction

Detecting the corrosion mechanism is vital to decisions related to intervention, mitigation and alleviation of large scale damage in structural steel structures. Corrosion does not necessarily occur uniformly underneath the coating. Pitting corrosion and crevice corrosion could also undertake beneath the coating. These have a more aggressive impact than uniform corrosion. So, the types of corrosion (pitting or uniform) occuring underneath the epoxy coating is also an important factor to consider as it has profound effect on overall performance and durability of the steel pipe [1].

Classical pitting corrosion mechanism of metals is attributed to the rust coved corrosion cells which are formed due to the oxygen concentration difference inside and outside of the corrosion pits. Corrosion media such as Cl^- then enter into the corrosion pits and form an aggressive HCl corrosion environment. As a result, corrosion will propagate toward the depth direction to form pitting corrosion. When the depth of the pit becomes critical, failure occurs in the pipeline. The objective of this chapter is to explore if the sensor textiles can be used to detect the mechanism differences. We first explore the mechanisms of corrosion.

5.2 Background to Corrosion Mechanisms

Typically, uniform corrosion is a type of electrochemical oxidation that occurs when metals react with oxidants such as oxygen. The transfer of electrons between metals results in two types of reactions: oxidation and reduction. The metal (Fe) gives up or lacks valence electrons (2e) and becomes positively charged during an oxidation reaction. In this case, the metal acts as an anode, and the reaction is referred to as an anodic reaction, as shown by Equation 5.1 [2]:

$$Fe \rightarrow Fe^{2+} + 2e^- \qquad \text{(Eq. 5.1)}$$

The cathodic reactions tend to change based on the conditions associated to it. At a higher pH (10) the possible anodic and cathodic reactions could be defined by Equation 5.2 and 5.3 respectively [3]. The overall reaction can be expressed through Equation 5.4.

$$Fe \rightarrow Fe^{2+} + 2e^- \qquad \text{(Eq. 5.2)}$$

$$2H_2O + 2e^- \rightarrow H_2 + 2OH^- \qquad \text{(Eq. 5.3)}$$

$$Fe^{2+} + 2OH^- \leftrightarrow Fe(OH)_2 \qquad \text{(Eq. 5.4)}$$

But the final corrosion product can be affected by any deposits such as rust. It accelerates the corrosion process significantly on the deposited area and cause pitting. Kim et al. [2] deposited 3 different iron oxides (Fe_3O_4, Fe_2O_3 and α-FeOOH) into the metal and tested its corrosion mechanism. They find that the pitting corrosion took place in α-FeOOH where as uniform corrosion had taken place for all other sample. They also found the corrosion process increased significantly after depositing iron oxides on steel surface and the final product of their corrosion was Fe_3O_4 for all the case. They assign the following reactions for Fe_3O_4 formation where the $Fe(OH)_2$ converts into more stable $Fe(OH)_3$ and then become Fe_3O_4 [2].

The surface film formation is accelerated by different iron oxide deposits. Under the α-FeOOH deposit, the following reactions occurred on the steel substrate [2]:

$$2FeOOH + Fe^{2+} \rightarrow Fe_3O_4 + 2H^+ \qquad \text{(Eq. 5.6)}$$

$$Fe^{2+} + 8FeOOH + 2e^- \rightarrow 3Fe_3O_4 + 4H_2O \quad \text{(Eq. 5.7)}$$

Due the reduction rection of α-FeOOH as shown in Equation 5.7, the cathodic reaction was increased and that was reflected the polarization curve and cathodic Tafel constant. In addition, with the increase in α-FeOOH reduction reactions, more Fe^{2+} ions were required to satisfy the equilibrium of Equations 5.6 and 5.7 such that the anodic dissolution of Equation 5.1 was increased simultaneously. So, the anodic Tafel constant increased for α-FeOOH deposited samples.

Under the Fe_3O_4 deposit, the following reactions can occur on the substrate [2]:

$$Fe_3O_4 + 5H_2O \rightarrow 3Fe(OH)_3(s) + H^+ + e^- \quad \text{(Eq. 5.8)}$$

$$Fe_3O_4 + 4H_2O + OH^- \rightarrow 3Fe(OH)_3^- \quad \text{(Eq. 5.9)}$$

Equations 5.8 and 5.9 indicate the oxidation and reduction of Fe_3O_4 with water and hydroxide ions in the test solution, respectively. These oxidation and reduction reactions of Fe_3O_4 are indicated by the increase in anodic and cathodic reactions in the polarization curve. Similarly, the oxidation and reduction reaction was expressed by Equation 5.10 and 5.11 for Fe_2O_3 deposit [4,5]. Due to this additional oxidation and reduction reaction in presence of Fe_2O_3, anodic and cathodic reactions increased as indicated by their anodic and cathodic Tafel constant. Under the Fe_2O_3 deposit, the following reaction occurred on the substrate [4,5]:

$$Fe(OH)_4^- + e^- \rightarrow Fe(OH)_3 + OH^- \quad \text{(Eq. 5.10)}$$

$$Fe_2O_3 + Fe(OH)_3^- \rightarrow Fe_3O_4 + H_2O + OH^- \quad \text{(Eq. 5.11)}$$

From the optical microscopy author concluded that that a large pitting corrosion took place in α-FeOOH-covered steel substrate whereas uniform pitting carrion was noticed for rest of the covered samples. Normally, pitting corrosion takes place in stagnant water like our testing condition. At first, corrosion occurs uniformly in metal surface, forming a rust layer over it [6]. When there is a void or crack in the rust, heavier ions like Cl- reaches to there but cant start a corrosion reaction as the remaining rust is obstructing the positive and negative ions to meet together, thereby creating a anodic and cathodic region. Then acidification occurs due to $FeCl_2$ in the anodic region and pitting corrosion starts taking place. Similarly, uniform corrosion took place initially and formed a rust layer. The rust on the steel and iron at the initial stage of corrosion is generally composed of $Fe(OH)_3$, α-FeOOH, and Fe_3O_4 from each transformation.

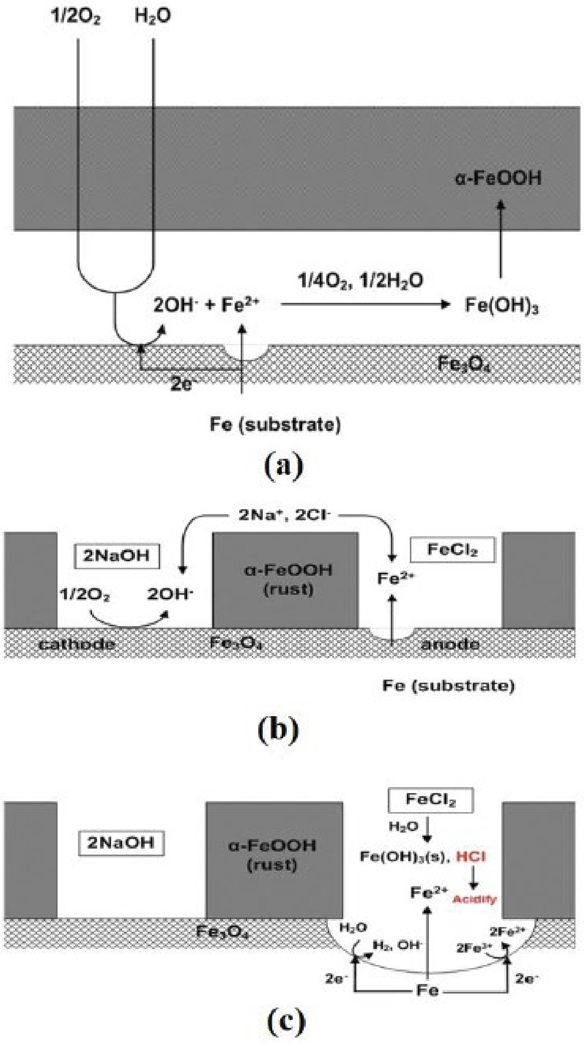

Figure 5.1: Schematic mechanism of (a) rust film formation on the steel at the initial stage of corrosion, (b) and (c) corrosion under the α-FeOOH rust [2,6].

Based on oxidation and reduction reactions, porous defects such as cracks and voids were developed in the rust layer, and the outside environment reaches the metal. The corrosion in these defects initiates a reaction, but the Fe^{2+} and OH^- ions cannot react directly because the remaining α-FeOOH rust obstructs their direct reaction as shown in Figure 5.1(b). Due to these separated reactions, $FeCl_2$ and NaOH are formed in the anode and cathode regions, respectively. Acidification occurs due to the $FeCl_2$ in the anode region when the anode dissolution is accelerated as shown in Figure 5.1(c) and pitting corrosion started taking place.

Replicating this approach for inducing different corrosion mechanisms [2], we examine the viability of the sensor textiles impact both on the corrosion rate and detection. Corrosion was thus initiated into steel pipe by covering the steel with different iron oxides (Fe_3O_4, Fe_2O_3 and α-FeOOH), and investigated in simulated heating water at 40 ºC while submerging it in 4.2% sea salt solution to stimulate pitting corrosion in the steel substrate. Electrochemical measurements (Tafel, EIS, Potentiodynamic Polarization tests) were carried out to study the influence of each oxide on the corrosion behavior in the in 4.2% sea salt water. Furthermore, the corrosion mechanism under different iron oxides was also investigated by XRD and optical microscopic images. Then all the corroded specimens were coated with epoxy and sensor textile embedded in the coating. The EIS was monitored for 10 days. The effectiveness of the sensor for different corroded samples was established by comparing the sensor as the reference electrode versus the instrument electrode using EIS to evaluate pre-corrosion and post-corrosion effectiveness.

5.3 Materials and Methods

5.3.1 Deposition of Iron Oxides on Carbon Steel Sample

The low-carbon steel (AISI-SAE 1018), received from McMaster-Carr (Santa Fe Spring, CA, USA), was machined into 50 × 25.4 × 3.2 mm shapes first. Then the steel coupons were polished using SiC sheets with grit 240 and 600, respectively, as mentioned in ASTM G5 for corrosion test requirements. After polishing, the coupons were washed with distilled water and acetone, respectively, and left at room temperature to dry. SkySpring Nanomaterials Inc. (Houston, TX, USA) and Sigma-Aldrich (St. Louis, MO, USA) provided the three iron oxides (Fe_3O_4, Fe_2O_3 and α-FeOOH) used in this study. Since powder-state iron oxides are difficult to deposit on the specimen, the iron oxides were mixed with ethanol as shown in Figure 5.2. To simulate the UDC environment, the specimen was covered with a rubber ‘O' shaped ring (diameter: 1 cm, height: 2 mm) and then filled with iron oxide mixed with ethanol, which has the same thickness as the rubber ring, approximately 2 mm ethanol. The deposit-covered samples were dried in air for 30 minutes before electrochemical tests.

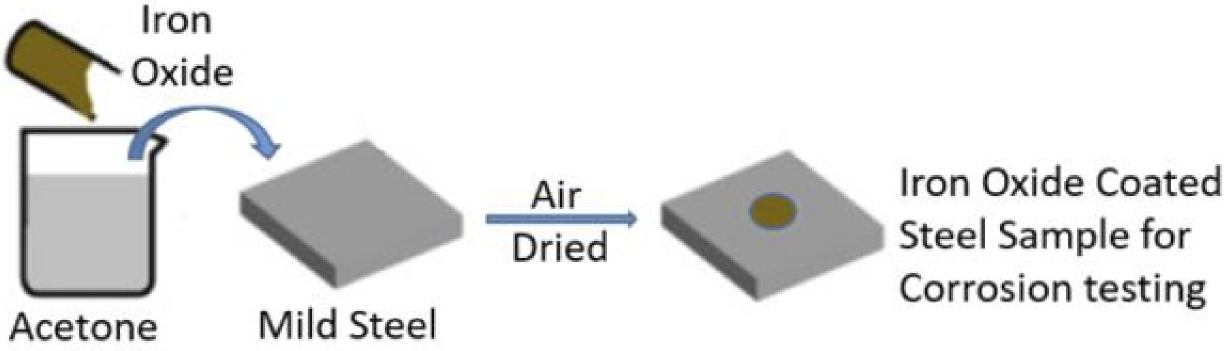

Figure 5.2: Schematic diagram of the deposition of iron oxides on carbon steel sample

5.3.2 Electrochemical Measurements of Iron Oxides Deposited Samples

To analyze the corrosion behavior and properties of the iron oxide deposits, electrochemical tests were carried out. A three-electrode electrochemical cell was built, with iron oxide deposited steel serving as the working electrode (WE), Pt mesh serving as the counter electrode (CE), and Ag/AgCl serving as the reference electrode (RE). The samples were fully covered with iron oxide dep in potentiodynamic polarization tests. The working electrode was immersed in the test solution for 3 hours prior to potentiodynamic polarization tests, until a steady state was reached and the open-circuit potential (OCP) was obtained. Tafel tests were performed by scanning the potential at a sweep rate of 0.166 mV/s from 250 mV versus OCP to 400 mV_{SCE}. The electrochemical impedance spectroscopy (EIS) was performed at the OCP with amplitude of 10 mV at frequencies ranging from 10,000 to 0.1 Hz.

To induce the corrosion process, potentiostatic tests were carried out for 20 hours at an applied potential of 0.65 mV_{SCE}, which was slightly higher than the corrosion potential (E_{corr}) of each specimen. The corrosion process beneath the deposits was observed using fully deposit-covered specimens. Following potentiostatic tests, the iron oxide deposits and corrosion products on the carbon steel surface were analyzed to evaluate the corrosion process by removing and cleaning the steel surface for 10 min in the cleaning solution containing (500 mL HCl of 37% concentration with 1000mL distilled water). The specimens were then rinsed in distilled water again and dried in vacuum.

5.3.3 Surface Characterization

Using optical microscopy, the morphology of the corroded specimens was examined following the potentiostatic tests (OM). For a clear view of the damaged surface, a cleaning solution containing 500 mL HCl of 37% concentration and 1000 mL distilled water was applied for 10 minutes. Furthermore, the specimens were analyzed by Rigaku Ultima III X-ray Diffractometer to investigate the surface condition beneath the oxide deposits (Rigaku Americas Corporation, The Woodlands, TX, USA).

5.3.4 Preparation of Corrosion Sensor Sample

After the surface cauterization, a diglycidyl ether-based epoxy resin (System Three, Lacey, WA, USA) with hardener with a 2:1 stoichiometry was then mixed and applied to the corroded coupons by a smooth brush. The coated coupons were kept at room temperature for 72 hours to cure. After the first layer of the coating was completely cured, a thin layer of the same epoxy resin was applied again onto the coating surface intended for the sensor. When the 3% ZnO-PVDF sensor (25 × 15 × 0.025 mm) adhered to the coating surface, a copper core electrical wire was connected onto the embedded sensor using silver paste and kept in an oven at 100 °C for an hour. Then, the second layer of epoxy resin was applied on the surface, as shown in Figure 5.3(a). A digital gauge Omega DGT-500 was used to determine the coating thickness of the coupons. The thickness of the base coat and topcoat was 60 µm, each leading to a coating thickness of 120 ± 10 µm. The preparation of the 3% ZnO-PVDF sensor is discussed in our previous studies [1].

5.3.5 Electrochemical Impedance Spectroscopy (EIS) Experimental Setup to Evaluate Sensor Performance

The sensor textile was compared to a calibrated EIS system to assess its effectiveness in detecting fluid corrosion/permeation. A BioLogic SP-300 EIS machine with three electrodes was used. As shown in Figure 5.3, the reference electrode (RE) for the total coating system was Ag/AgCl, the counter electrode (CE) was platinum mesh, and the working electrode (WE) was the steel substrate (b). This configuration is known as "Configuration A." To validate the sensor, we modified the EIS setup to convert the sensor textile into the reference electrode, as described in our previous work [1]. The reference electrode was replaced by the sensor textile in this configuration, as shown in Figure 5.3(c), with platinum as the CE and steel as the WE, and the data obtained from this configuration were labeled as sensor data. For ten days, the EIS was collected every 24 hours in a 4.2% sea salt solution. The sampled area was 1 cm^2.

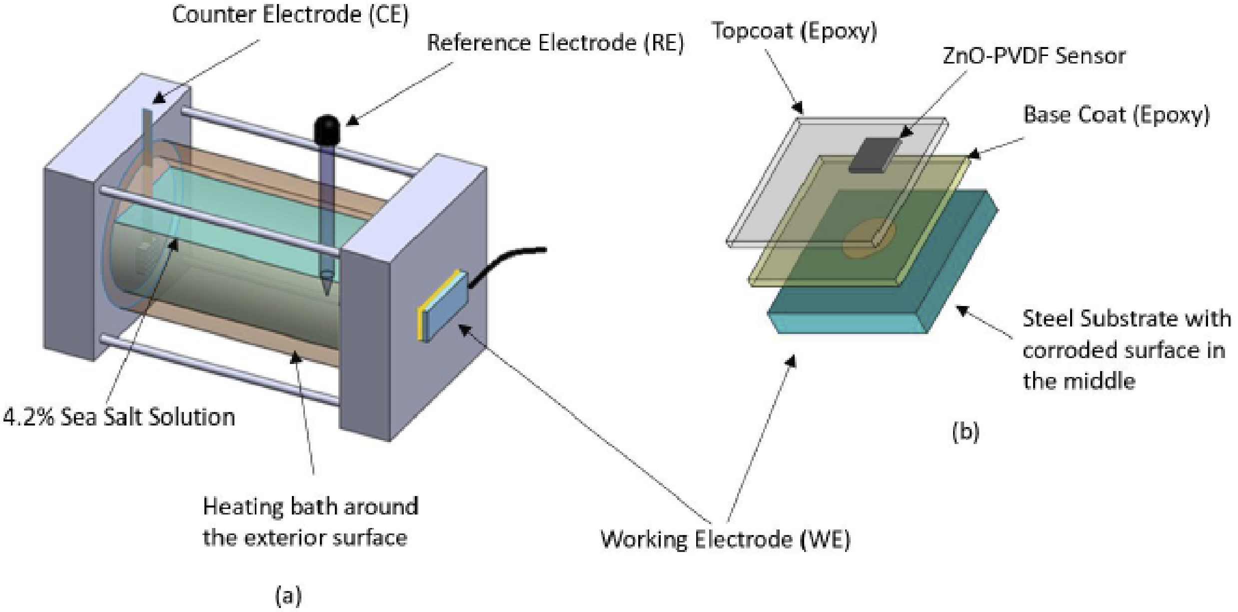

Figure 5.3: Schematic diagram coated sample and EIS experimental setup (a) corrosion cell (b) metal substrate with corroded surface in it. Configuration A: steel substrate is WE, Pt mesh is CE and Ag/AgCl is RE and Configuration B: steel substrate is CE, Pt mesh is WE and sensor is RE.

5.4 Results and Discussion

5.4.1 Tafel Test

Potentiodynamic polarization curves of bare steel and iron oxides (Fe_3O_4, Fe_2O_3 and α-FeOOH) covered specimens are presented in Figure 5.4 after submerging them in 4.2% sea salt solution for 3 h immersion at 40 °C. The curves were then extrapolated to obtain the corrosion kinetics parameters like the anodic and cathodic Tafel slopes (βa, βc), corrosion potential (E_{corr}), corrosion current density (i_{corr}), polarization resistance (R_p) and corrosion rate. Corrosion rate was calculated according to Faraday's law [7]:

$$Corrosion\ Rate = \frac{3.16\times10^{8}\times i_{corr}\times M}{z\times F\times \rho} \qquad \text{(Eq. 5.12)}$$

where, M is the molar mass of the metal (g/mol), z is the number of electrons transferred per metal atom, F is the Faraday's constant, and ρ is the density of the metal (g/cm^3). The polarization resistance was calculated by the following equation [7]:

$$R_p = \frac{\beta_a\times\beta_c}{2.3\times i_{corr}\times(\beta_a+\beta_c)} \qquad \text{(Eq. 5.13)}$$

where the i_{corr} and R_p are related to the corrosion resistance of the materials. All these values are listed in Table 5.1.

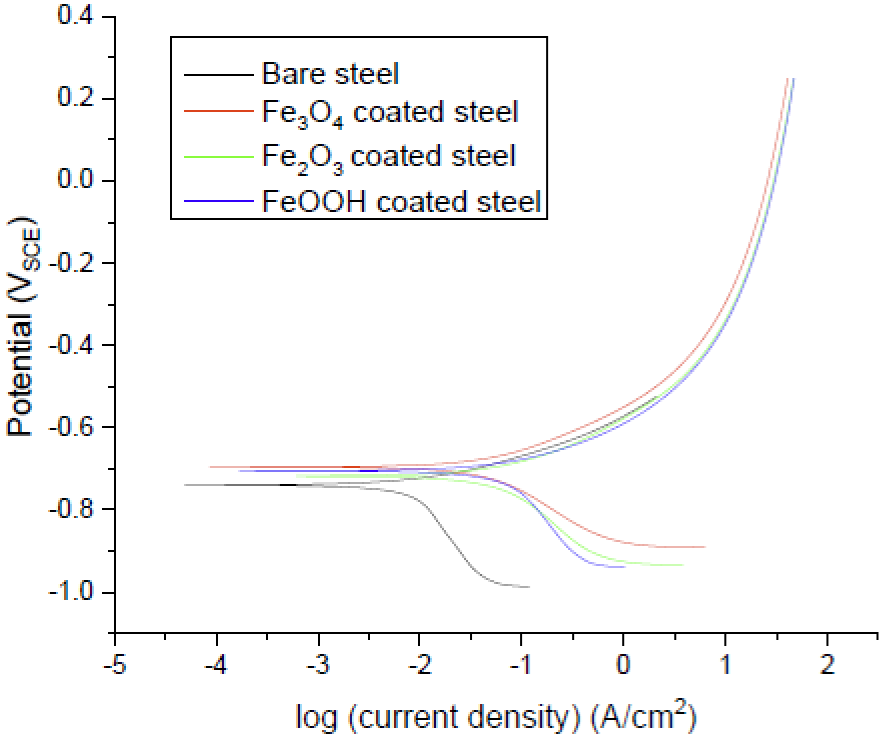

Figure 5.4: Polarization curves with Tafel slopes of the specimens covered with different iron oxides (Fe_3O_4, Fe_2O_3 and α-FeOOH) and uncovered after 3 hour of immersion in at 40 °C.

Table 5.1: Electrochemical parameters of the polarization curves of the bare specimen and iron oxides (Fe_3O_4, Fe_2O_3 and α-FeOOH) covered specimens in the simulated district heating water at 40 °C.

Spaceman	β_a (mV/decade)	β_c (mV/decade)	E_{corr} (mV_{SCE})	i_{corr} (μA/cm^2)	R_p (Ω.cm^2)	Corrosion Rate (mm/year)
Steel	30.32±2.64	-61.21±1.31	738.92±1.42	2.80±0.76	3146.93±10.62	0.033±0.007
Fe_3O_4	90.35±1.59	-146.56±2.27	693.41±1.04	38.27±1.02	633.09±9.28	0.447±0.005
Fe_2O_3	84.62±2.25	-150.74±1.16	715.31±2.76	40.76±0.91	540.73±8.91	0.486±0.008
FeOOH	75.48±3.16	-134.45±2.84	709.58±2.57	41.94±1.23	499.02±12.29	0.489±0.012

The data in the Table 5.1 clearly shows that the both anodic and cathodic Tafel slopes (β_a, β_c) have shifted in the positive and negative direction respectively compared to bare steel. This indicates that there was an increase in cathodic and anodic reactions for all iron oxides covered samples as expected [8-10]. Current densities (i_{corr}) of the all the iron oxides covered samples increased by approximately 15 times and followed this order: α-FeOOH > Fe_2O_3 > Fe_3O_4 > bare. Since, i_{corr}, β_a, and β_c are directly connected to R_p and corrosion rate, a drop in R_p and increase in corrosion rate of the iron oxide coved specimens were recorded. The overall data indicates that the corrosion reactions were affected by all three iron oxide deposits and corrosion in the steel had significantly increased validating the sample is appropriately reflective of the corrosion for sensor textile assessment.

5.4.2 Electrochemical Impedance Spectroscopy (EIS)

The Bode impedance and phase angle data for all samples have been plotted and are shown in Figure 5.5. The specimen coated with iron oxides has a lower absolute impedance value than the bare specimen. The order in which the absolute impedance value decreases is as follows: α-FeOOH > Fe_2O_3 > Fe_3O_4 > bare, which follows the pattern observed in potentiodynamic polarization experiments. Additionally, the phase angle decreased in the following order: α-FeOOH > Fe_2O_3 > Fe_3O_4 > bare, and the shoulder on the phase angle curve of the bare pipe shifted to a lower frequency as expected. The findings have been attributed to inhomogeneity or porosity in the surface film [11], suggesting that the surface film degrades when coated with iron oxides, especially in the case of the α-FeOOH-covered specimen.

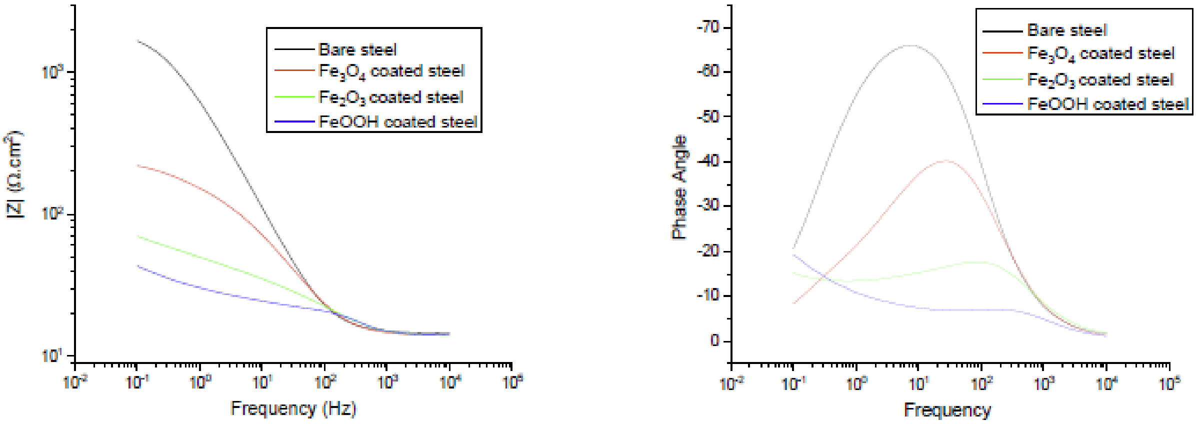

Figure 5.5: Bode plots of (a) impedance and (b) phase angle vs. frequency for specimens covered with different iron oxides (Fe_3O_4, Fe_2O_3 and α-FeOOH) and uncovered after 3 hours of immersion at 40 °C.

The EIS data were analyzed using EC-Lab software and employing the electrical circuit model (Figure 5.6) validated previously for iron oxide deposits over steel substrate [2]. The model shows the solution resistance, the pore resistance and pore capacitance (R_{pore} and CPE_{pore}), charge transfer resistance (R_{ct}), and double layer capacitance of the system (CPE_{dl}). Constant phase element, CPE, was used instead of a pure capacitor C in the model to take into account the deviations from ideal dielectric behavior related to surface heterogeneity, and its impedance at constant phase angle is given by [12,13]:

$$Z_{CPE} = \frac{1}{Z_0(j\omega)^n} \quad \text{(Eq. 5.14)}$$

where n and Z_0 are constant. The capacitance element CPE is a pure capacitor when n = 1 and is a pure resistor when n = 0 [14-15]. The fitted values extracted were consistent with the Bode plot (Figure 5.5 and Table 5.2). A low $\chi 2$ value ($<5\ e^{-2}$) indicated the goodness of the curve fitting for each sample.

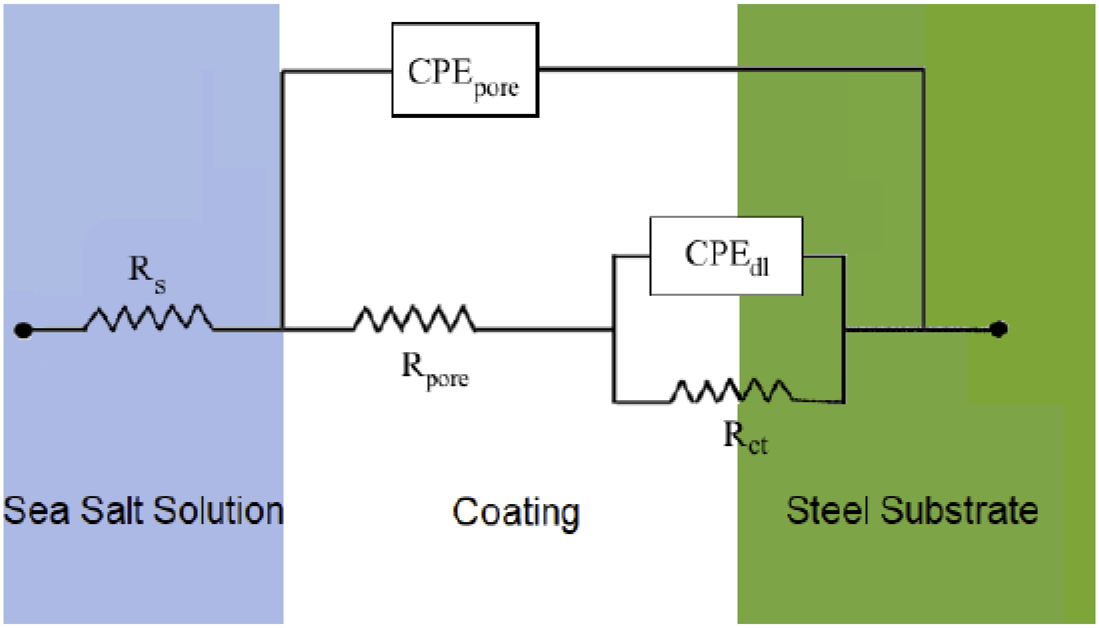

Figure 5.6: Equivalent circuit to fit the electrochemical impedance spectroscopy (EIS) data [1].

R_{film} and R_{ct} decreased for the iron oxide-covered specimens in the following order: α-FeOOH > Fe_2O_3 > Fe_3O_4 > bare. The covered iron oxides had the lower corrosion resistance than bare specimen. Additionally, the n value in the case of α-FeOOH was the lowest, indicating an unstable surface film due to pores and defects on the surface.

Table 5.2: Impedance parameters of bare specimen and iron oxides (Fe_3O_4, Fe_2O_3 and α-FeOOH) covered specimens in the 4.2% sea salt water at 40 °C.

Spaceman	R_s ($\Omega.cm^2$)	R_{flim} ($\Omega.cm^2$)	n	C_{flim} ($mF.s^{n-1}.cm^{-2}$)	R_{ct} ($\Omega.cm^2$)	n	C_{dl} ($mF.s^{n-1}.cm^{-2}$)	χ^2 (10^{-3})
Steel	14.38	944.75	0.87	0.25	1091.82	0.66	3.38	1.11
Fe_3O_4	13.87	57.36	0.84	2.29	192.74	0.47	27.27	1.19
Fe_2O_3	13.74	12.37	0.83	3.25	145.283	0.09	19.46	1.55
α-FeOOH	15.84	6.62	0.79	2.06	140.325	0.39	50.26	1.99

5.4.3 Potentiostatic Tests

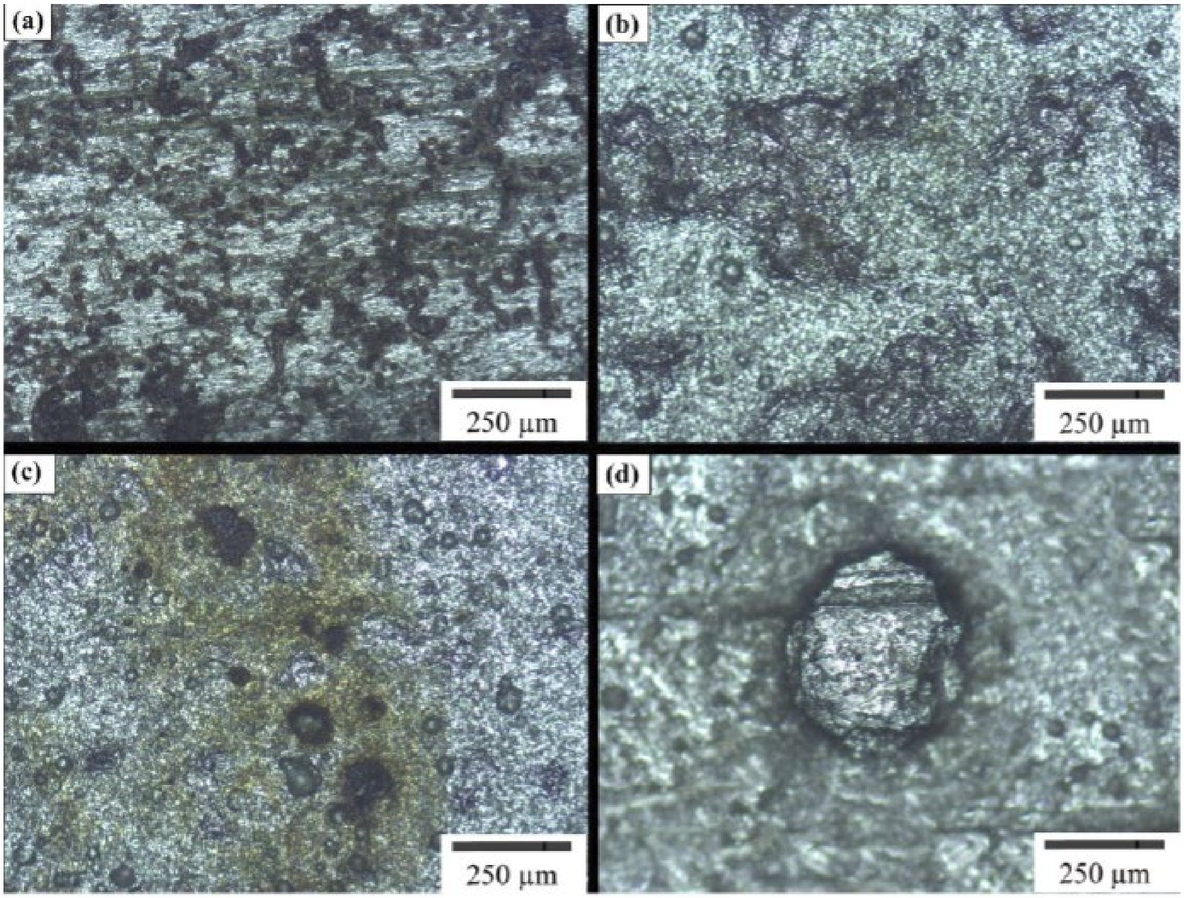

Figure 5.7: Optical microscope images of the specimens covered with (a) bear steel (b) Fe_3O_4, (c) Fe_2O_3 and (d) α-FeOOH iron oxide deposits, after potentiostatic tests under −650 mVSCE for 20 hours in the 4.2% sea salt water at 40 °C.

To speed up the corrosion process, potentiostatic tests were carried out for 20 hours at an applied potential of 0.65 mV_{SCE}, which was slightly higher than the corrosion potential (E_{corr}) of each specimen. Figure 5.7 shows the specimen covered iron oxides after potentiostatic tests. As shown in Figure 5.7(d), significant pitting was observed on the α-FeOOH-covered specimen and the size of the pits ranged from 250 to 300 µm. However, as shown in Figure 5.7(b,c), pitting was not observed on the Fe_3O_4 and Fe_2O_3 covered specimens. This implies that the corrosion behavior was different in the α-FeOOH, Fe_3O_4, and Fe_2O_3 cases.

5.4.4 Surface Characterization

The X-ray diffraction (XRD) patterns of raw iron oxide powders, bare steel and iron oxide coved samples are shown in Figure 5.8 a and b. Fe, α-FeOOH and Fe_3O_4 peaks are visible in XRD spectra of Fe_3O_4 deposited sample, while Fe, Fe_2O_3, and Fe_3O_4 peaks are present in Fe_2O_3 covered spaceman. Similarly, both α -FeOOH and Fe_3O_4 peaks were obtained with high strength in the case of α-FeOOH deposited spaceman. These findings suggest that the final corrosion substance from all of the tests was Fe_3O_4 in the testing conditions, and that α-FeOOH affects the development of the Fe_3O_4 surface film on the steel substrate in comparison to the Fe_2O_3 and Fe_3O_4 examples as others have shown [2].

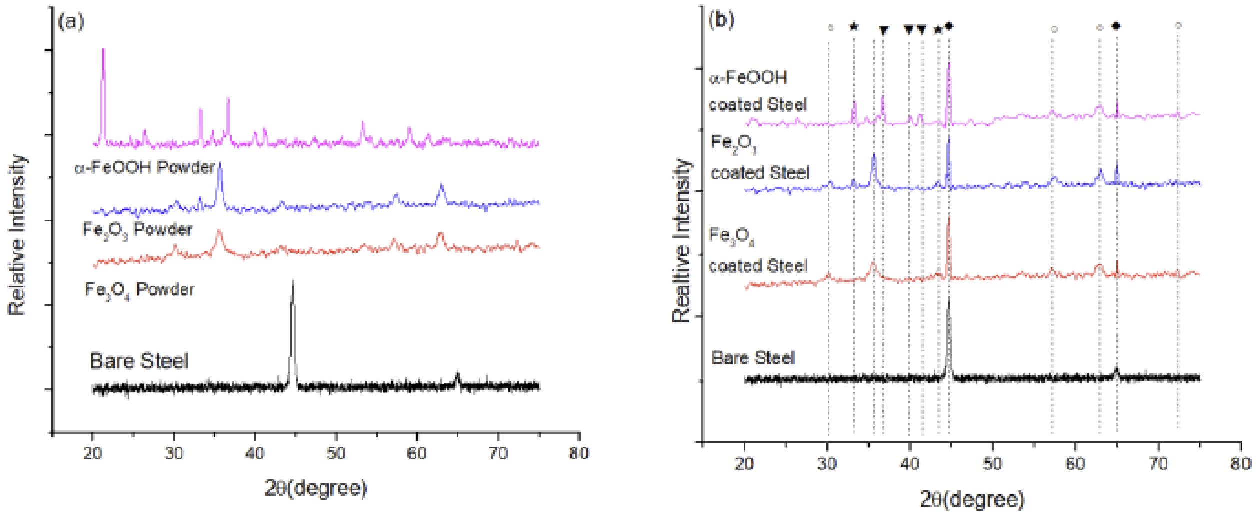

Figure 5.8: XRD data for the (a) raw powders and (b) bare sample and iron oxides deposited samples after immersed in the 4.2% sea salt water at 40 °C (▼: α-FeOOH; ◆: Fe; ○: Fe_3O_4; ★: Fe_2O_3).

5.4.5 Sensor Data from EIS

To establish the viability of real-time monitoring, the uniform corrosion sample (bare steel, Fe_3O_4 and Fe_2O_3) and the pitting corrosion sample (FeOOH) were coated with double layer of epoxy resin embedded with 3% ZnO-PVDF sensor. Then coated samples placed in a corrosion cell to induce corrosion through longer time immersion in 4.2% sea salt water solution. The coated samples were submersed into 4.2% sea salt solution for 10 days to perform EIS testing using Configurations A and B. The Bode magnitude plot associated with Configuration A and B of the topcoat/basecoat system with different sensors are shown in Figure 5.9.

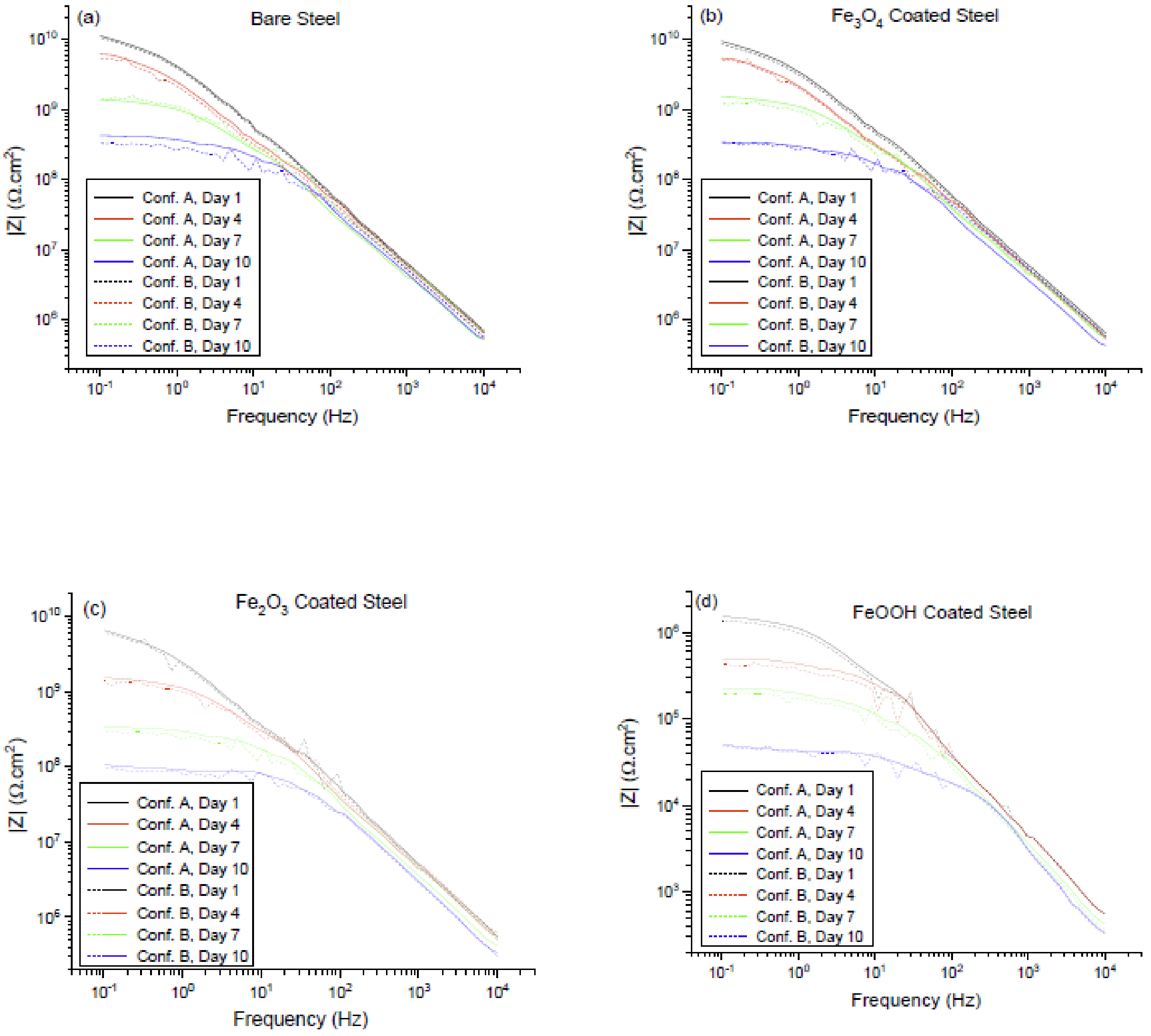

Figure 5.9: Bode plot (instrument (solid lines) and sensor textile (dotted lines)) for (a) bare steel, (b) Fe_3O_4 coated steel, (c) Fe_2O_3 coated steel and (d) FeOOH coated steel.

EIS data of shows a plateau region while transitioning from high to low frequency. This becomes more apparent on day 7 and after. This indicated that corrosion resistance (e.g. pore and charge transfer resistance) of the coating started degrading significantly after four days as the low frequency plateau region suggested the d.c. limit of the coating. The overlay of the Bode plots of Configuration A and B also showed similar trends. Nyquist plots demonstrate partial capacitive semi-circle for all the samples immediately after the coating, showing that all epoxy coatings provide adequate protection against initial corrosion. As the days passed, the diameters of the circle decreased, meaning indicating that the value of the charge transfer resistance and pore resistance are declining.

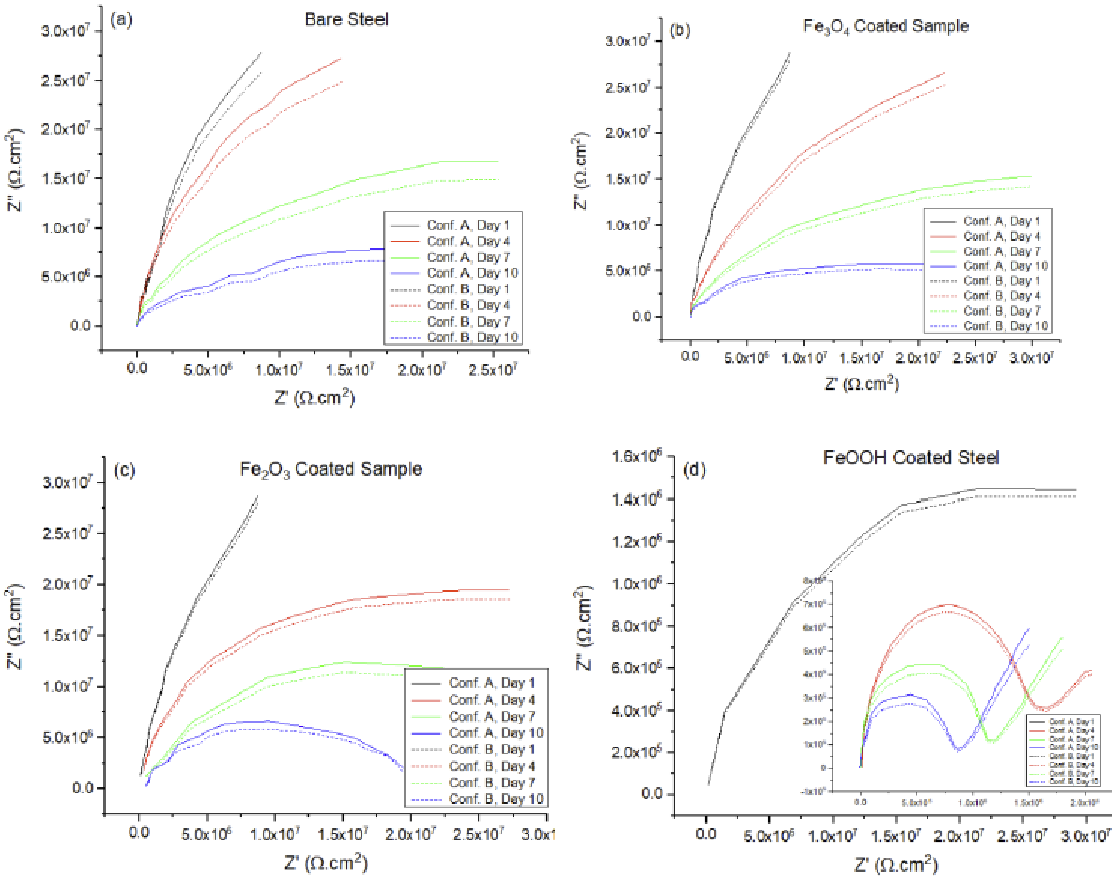

Figure 5.10: Nyquist plots (instrument (solid lines) and sensor textile (dotted lines)) for (a) bare steel, (b) Fe_3O_4 coated steel, (c) Fe_2O_3 coated steel and (d) FeOOH coated steel.

Two differences occurred based on the type of corrosion. For the pitting corrosion samples, Nyquist plots changed into a very different pattern as the days progressed (Figure 5.10(d)). A full semicircle appeared which probably attributed from the pitting corrosion on the surface of the steel substrate [16]. For uniform corrosion, partial capacitive semi-circles persisted. The EIS data associated with Configuration A and B were fitted into EC-Lab software to evaluate and compare the equivalent circuit parameters. R_{pore} was the most vital parameter in this model circuit as R_{pore} was the resistance of ion-conducting paths that developed in the coating after being exposed into 4.2% sea salt solution for a long time. Reduction of R_{pore} indicated that the coating had started degrading. The extracted data of equivalent circuit is listed in Table 5.3. The R_{pore} values obtained from Configuration A and B were consistent with a maximum error of 24.56% on day 10. For day 1 and 4, the error between instrument data in Configuration A and sensor data in Configuration B was less than 10%. This indicates that prior to the corrosive fluid reaching the sensor textile (day 4), the textile provides a higher accuracy.

Another notable thing was the value of R_{ct} of pitted corrosion sample (FeOOH coated sample) and uniformed corroded sample. For the uniformly corroded sample, R_{ct} value remained in the GΩ range for first 4 days whereas R_{ct} of FeOOH coated sample was found in MΩ range from day 1 as shown in Figure 5.11 (b). This indicated that the pitting corrosion had drawn much current hence its resistance was very low compared to other samples which was in agreement from Tafel and EIS data as presented in previous section. This indicated that the pitting corrosion had drawn higher current hence its resistance was very low compared to other samples.

Table 5.3 Electrochemical equivalent circuit parameters at different configurations

Sample	Conf.	χ^2(E^{-2})	R_{pore} (MΩ)	R_{ct} (GΩ)	C_{pore} (pF.s^{n-1}.cm^{-2})	C_{dl} (μF.s^{n-1}.cm^{-2})	Error for R_{pore} (%)	Error for R_{ct} (%)	Error for C_{pore} (%)	Error for C_{ct} (%)
Bare Steel Day 1	A	0.71	8.34±0.56	10.27±0.69	10.97±0.74	6.33±0.43	3.93	4.82	3.20	5.96
	B	0.57	8.01±0.70	9.78±0.26	10.62±0.20	6.08±0.33				
Bare Steel Day 4	A	0.29	5.86±0.45	6.09±0.43	11.16±0.46	6.65±0.31	4.78	2.79	1.34	5.71
	B	3.83	5.58±0.42	5.92±0.17	11.01±0.38	6.27±0.20				
Bare Steel Day 7	A	7.45	2.28±0.26	2.01±0.41	12.62±0.54	7.24±0.47	9.84	9.95	8.56	6.35
	B	10.56	2.01±0.37	1.79±0.21	11.54±0.62	6.78±0.23				
Bare Steel Day 10	A	7.63	1.21±0.32	0.59±0.28	12.89±0.79	7.54±0.49	15.70	18.64	9.46	13.93
	B	12.87	1.02±0.29	0.48±0.41	11.67±0.65	6.49±0.37				
Fe_3O_4 Coated Day 1	A	2.76	7.05±0.29	8.02±0.35	9.68±0.31	5.08±0.42	1.75	3.15	2.80	5.03
	B	1.65	6.93±0.47	7.76±0.53	9.41±0.10	4.82±0.38				
Fe_3O_4 Coated Day 4	A	2.54	5.43±0.28	5.23±0.21	9.89±0.37	5.45±0.26	4.42	3.25	4.55	8.44
	B	2.98	5.19±0.37	5.06±0.35	9.44±0.45	4.26±0.29				
Fe_3O_4 Coated Day 7	A	5.76	1.93±0.09	1.37±0.27	10.81±0.34	6.69±0.52	8.95	8.14	9.16	11.51
	B	9.65	2.18±0.23	1.19±0.31	9.82±0.49	5.92±0.38				
Fe_3O_4 Coated Day 10	A	7.45	0.59±0.24	0.27±0.44	10.98±0.39	7.28±0.36	27.12	22.22	10.66	10.16
	B	13.77	0.43±0.18	0.21±0.32	9.81±0.56	6.54±0.45				
Fe_2O_3 Coated Day 1	A	0.87	5.21±0.55	5.67±0.43	5.21±0.65	5.45±0.68	4.35	3.27	1.88	2.83
	B	0.71	4.98±0.49	5.48±0.61	5.49±0.72	5.29±0.55				
Fe_2O_3 Coated Day 4	A	5.27	2.42±0.36	1.35±0.58	6.01±0.36	5.82±0.72	7.85	6.67	4.16	2.58
	B	9.65	2.23±0.47	1.26±0.34	5.76±0.48	5.67±0.57				

Sample	Conf.	$\chi^2(E^{-2})$	R_{pore} (MΩ)	R_{ct} (GΩ)	C_{pore} (pF.s^{n-1}.cm^{-2})	C_{dl} (μF.s^{n-1}.cm^{-2})	Error for R_{pore} (%)	Error for R_{ct} (%)	Error for C_{pore} (%)	Error for C_{ct} (%)
Fe_2O_3 Coated Day 7	A	6.44	1.23±0.19	0.25±0.15	6.38±0.81	5.97±0.72	7.57	9.70	8.62	4.02
	B	8.53	1.10±0.15	0.22±0.08	6.93±0.49	5.73±0.54				
Fe_2O_3 Coated Day 10	A	12.86	0.05±0.05	0.09±0.15	6.49±0.54	6.25±0.36	21.82	11.11	14.18	20.80
	B	18.25	0.04±0.09	0.08±0.19	7.41±0.49	4.95±0.29				
FeOOH Coated Day 1	A	0.54	2.47±0.17	0.140±0.11	5.92±0.12	2.74±0.16	5.34	6.23	1.08	5.12
	B	2.87	2.34±0.13	0.131±0.14	5.92±0.20	2.60±0.22				
FeOOH Coated Day 4	A	7.69	1.09±0.29	0.041±0.12	6.62±0.17	2.98±0.30	9.33	10.75	8.56	6.37
	B	10.52	1.01±0.17	0.037±0.25	6.28±0.18	2.79±0.13				
FeOOH Coated Day 7	A	15.09	0.28±0.29	0.011±0.27	6.91±0.51	3.15±0.35	17.71	19.09	9.11	9.40
	B	18.66	0.23±0.28	0.009±0.16	6.28±0.38	2.90±0.42				
FeOOH Coated Day 10	A	14.64	0.02±0.05	0.003±0.06	7.11±1.82	3.32±1.49	15.90	19.28	10.13	12.65
	B	21.52	0.01±0.01	0.001±0.01	6.39±1.79	2.90±1.95				

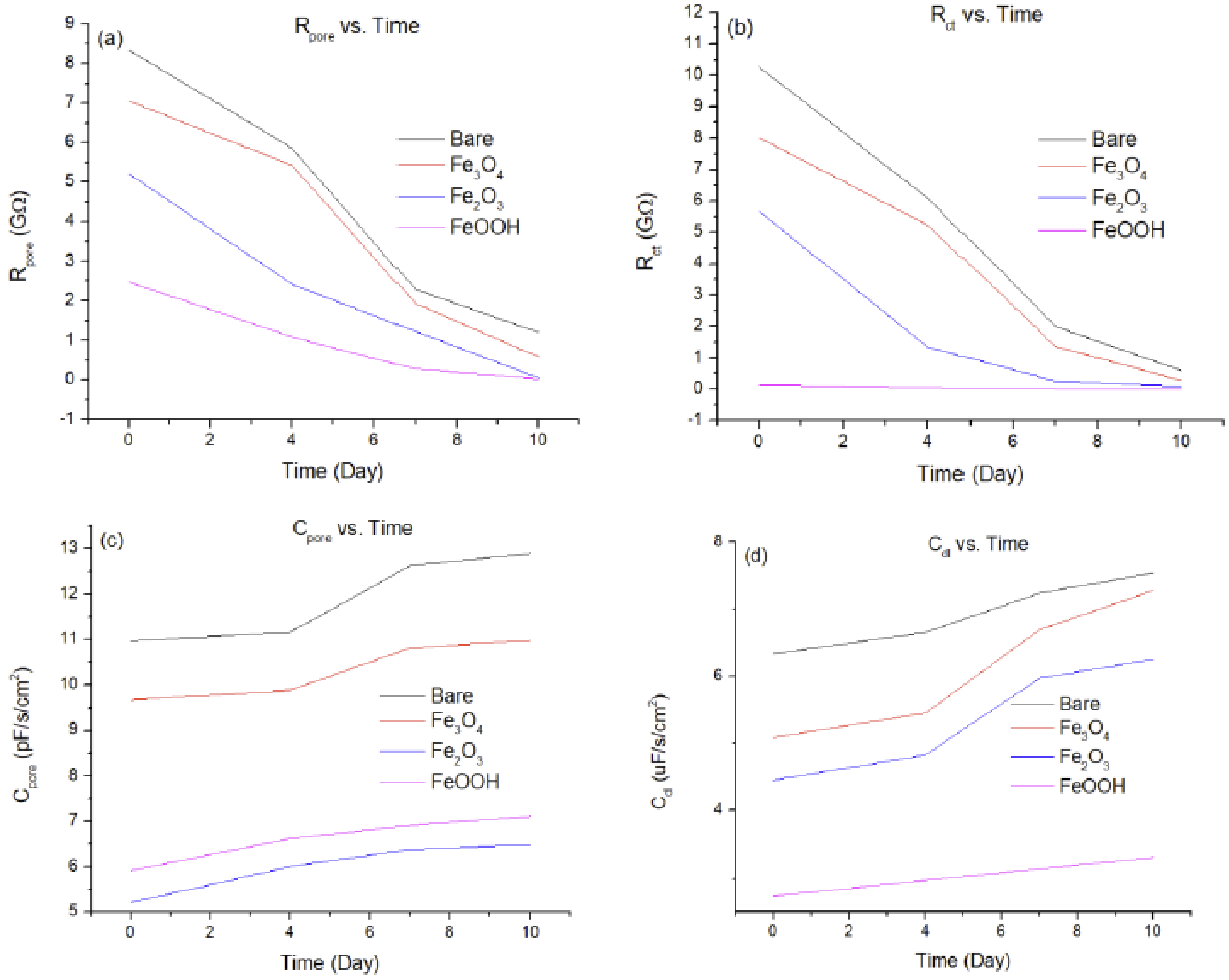

Figure 5.11: Electrochemcial equilavent circuit perameters against time (a) R_{pore}, (b) R_{ct}, (c) C_{pore}, and (d) C_{dl}.

5.5 Conclusion

In this chapter, a sensor textile of electrospun 3% ZnO-PVDF was explored for viability in sensing pitting and uniform corrosion mechanisms. The sensor textiles were placed in a protective epoxy coating in steel pipe. Pitting corrosion and uniform corrosion were accomplished in the bare steel by coating it with various iron oxides (Fe_3O_4, Fe_2O_3, and α-FeOOH) and then immersing it in 4.2% sea saltwater. Anodic and cathodic reactions increased dramatically on the α-FeOOH-covered specimen, resulting in creating voids, ultimately leading to pitting corrosion on the steel structure, while other deposited samples exhibited uniform corrosion. After coating all corroded specimens were tracked for ten days using an electrochemical impedance spectroscope (EIS). The data indicated that pitting corrosion attracted a large amount of current, resulting in a significantly low charge transfer resistance (~10 times lower than bare steel sample for day 1) with a full semi-circle loop while uniformly corroded specimens displayed nearly equal performance with partial semi-circle loop in Nyquist plot. The instrumental EIS data were compared with sensor data and it was found that the actual data and sensor data were consistent with a less than 10% error up to day 4 even for a low resistance in the case of pitting corrosion. When the corrosion rate increased and coating degraded, the sensor data deviated from the actual data significantly. This established the viability of the sensor textile for detecting pitting corrosion as well as uniform corrosion.

5.6 References

1. T. Chowdhury, N. D'Souza, Y.H. Ho, N. Dahotre, I. Mahbub, Embedded Corrosion Sensing with ZnO-PVDF Sensor Textiles, Sensors 20(11) (2020) 3053.

2. Yong-Sang Kim and Jung-Gu Kim “Corrosion Behavior of Pipeline Carbon Steel under Different Iron Oxide Deposits in the District Heating System” Metal, MDPI.

3. Cornell, R.M.; Schwertmann, U. The Iron Oxides: Structure, Properties, Reactions, Occurrences and Uses, 2nd ed.; WILEY-VCH: Weinheim, Germany, 2003; pp. 95–109, 201–217.

4. Fajaroh, F.; Setyawan, H.; Widiyastuti, W.; Winaradi, S. Synthesis of magnetite nanoparticles by surfactant-free electrochemical method in an aqueous system. Adv. Powder Technol. 2012, 23, 328–333.

5. Allanore, A.; Lavelaine, H.; Valentin, G.; Birat, J.P.; Delcroix, P.; Lapicque, F. Observation and modeling of the reduction of hematite particles to metal in alkaline solution by electrolysis. Electrochim. Acta 2010, 55, 4007–4013

6. Tamura, H. The role of rusts in corrosion and corrosion protection of iron and steel. Corros. Sci. 2008, 50, 1872–1883.

7. Mansfeld, F. Tafel slopes and corrosion rates obtained in the pre-Tafel region of polarization curves. Corros. Sci. 2005, 47, 3178–3186.

8. Stern, M.; Geary, A.L. Electrochemical polarization I. A theoretical analysis of the shape of polarization curves. J. Electrochem. Soc. 1957, 104, 56–63.

9. Tromans, D.; Silva, J.C. Behavior of copper in acidic sulfate solution: Comparison with acidic chloride. Corrosion 1997, 53, 171–178.

10. Huang, H.; Shaw, W.J.D. Electrochemical aspects of cold work effect on corrosion of mild steel in sour gas environments. Corrosion 1992, 48, 931–939.

11. Kim, K.H.; Lee, S.H.; Nam, N.D.; Kim, J.G. Effect of cobalt on the corrosion resistance of low alloy steel in sulfuric acid solution. Corros. Sci. 2011, 53, 3576–3587.

12. Lee, D.Y.; Kim, W.C.; Kim, J.G. Effect of nitrite concentration on the corrosion behaviour of carbon steel pipelines in synthetic tap water. Corros. Sci. 2012, 64, 105–114.

13. Moretti, G.; Guidi, F.; Grion, G. Tryptamine as a green iron corrosion inhibitor in 0.5 M deaerated sulphuric acid. Corros. Sci. 2004, 46, 387–403.

14. Mansfeld, F. Recording an analysis of AC impedance data for corrosion studies. Corrosion 1981, 36, 301–307.

15. Tang, F.; Bao, Y.; Chen, Y.; Tang, Y.; Chen, G. Impact and corrosion resistances of duplex epoxy/enamel coated plates. Constr. Build. Mater. 2016, 112, 7–18. Metals 2017, 7, 182 19 of 20

16. Liu, S.; Gu, L.; Zhao, H.; Chen, J.; Yu, H., Corrosion Resistance of Graphene-Reinforced Waterborne Epoxy Coatings. Journal of Materials Science & Technology 2016, 32, (5), 425-431.

CHAPTER 6

CONCLUSION AND FUTURE WORK

This dissertation sought to examine whether an insulative polymer sensor textile can function as a corrosion sensor. Questions examined were:

a) Are embedded sensor textiles functional in corrosion?

b) Is the constituent of the sensor textile via incorporation of nanoparticles vital to improving sensitivity?

c) How does the sensor textile perform over time in terms of reliability?

d) Can the textile function under different corrosion mechanisms?

The results support that sensor textiles are viable corrosion sensors under polymer coatings and their accuracy compared to the instrument was 10% or less while coatings were impermeable.

6.1 Effect of Sensor Constituent Materials

PVDF, a well-known sensor polymer, was modified with ZnO and formed into non-woven fiber meshes using electrospinning to investigate its potential as embedded corrosion sensors in epoxy coatings. The fabrication process of the fiber (electrospinning) made it more electroactive by changing its α crystal phase to β phase. The addition of ZnO further enhanced the β content in the fiber and made the fiber more thermally stable and hydrophobic which eventually increased the efficiency of the fiber in corrosion sensing.

After the addition of ZnO with sensor, coating resistance (R_{pore}) and charge transfer resistance (R_{ct}) increased significantly with ZnO fraction as shown in Table 6.1. R_{pore} value reached to 7.94 GΩ from 0.23 GΩ and R_{ct} value reached to 9.78 GΩ from 0.11 GΩ as the ZnO concentration reached to 5% from 0%. This could be attributed to the contributions of ZnO to the PVDF in increased resistance and capacitance pre-corrosion as well as increased hydrophobicity from the presence of ZnO. The accelerating corrosion testing (thermal cyclic method) data also showed that ZnO increases the accuracy of the sensor textile over the base PVDF while concurrently improving the impedance of the coating itself. 3% ZnO-PVDF sensor was showed the most accurate data over time and temperature.

Table 6.1: Equivalent circuit parameters immediately after coating

Sample	R_s (μΩ)	R_{pore} (MΩ)	CPE_{pore}		R_{ct} (GΩ)	CPE_{dl}		$X^2(E^{-2})$
			C_{pore}(pF)	n_{pore}		C_{dl}(μF)	n_{dl}	
Epoxy coating	3.59	0.23	5.77	0.91	0.11	0.35	0.89	0.29
Coating with PVDF fiber	2.64	2.34	6.24	0.87	1.32	2.96	0.83	4.62
Coating with 1% ZnO-PVDF fiber	3.47	4.73	8.79	0.89	5.15	4.91	0.92	3.45
Coating with 3% ZnO-PVDF fiber	1.85	7.21	9.93	0.90	8.22	5.21	0.90	9.94
Coating with 5% ZnO-PVDF fiber	2.25	7.94	10.45	0.88	9.78	6.03	0.89	5.59

6.2 Reliability of the Sensor Textiles

The pure coating degrades over the time as it exposed to harsh corrosive environment. From the literature we have seen that the epoxy could drop half of its impedance in few weeks under laboratory testing conditions. EIS data for double layer epoxy coating at thermal cyclic conditions is shown in Figure 6.1. It is clear that impedance value decreased with increase in temperature and author was trying to detect it through ZnO-PVDF sensor textile.

The effectiveness of the sensor was established by comparing the sensor as the reference electrode versus the instrument electrode using EIS in two different testing conditions. In the first case, the sample was submerged into the sea salt solution over 10 days to evaluate pre-corrosion and post-corrosion effectiveness. In the second case, an accelerated thermal cycling method was adopted which stimulated the coating failure by exposing the coated panels to cyclic temperature under constant immersion.

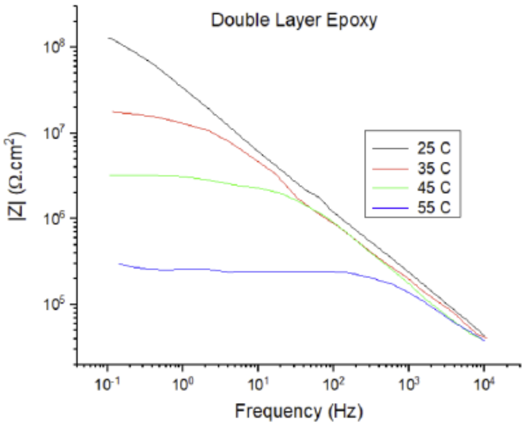

Figure 6.1: Bode impedance data for double layer epoxy at thermal cyclic method.

EIS data of 10 days immersion were compared, and it was found that the actual data and sensor data were consistent with a less than 10% error up to day 4 when the permeation of the fluid through the coating was low. When the corrosion rate increased and coating degraded, the maximum error was recorded as 24.56% on day 10. While accelerated thermal cycling was compared to the long-term degradation results and showed that the error between the sensor textile and coating was <10% for temperatures T_g -10 ˚C and below. As the set temperature of the thermal cycle approached the T_g of the epoxy coating, the barrier property of the coating was damaged significantly and the sensor reading deviated. ZnO played an active role in both cases as its hydrophobic property and thermal stability helped the sensors to sense corrosion more accurately against the harsh corrosive environment. From a vantage point of a sensor textile, the 3% ZnO-PVDF sensor was the most optimum sensor, showing a less than 10% deviation for the longest amount of time in both conditions. Further studies with electrochemical equivalent circuit parameters stated that the damage in coating for 10 days immersion in the first approach was equivalent to the damage of the 7th cycle of the thermal cycling approach. This indicated that the thermal cycling approach had saved 3 days to have the same level of coating degradation that we had in the first approach by submerging the coated panel into the electrolyte for 10 straight days.

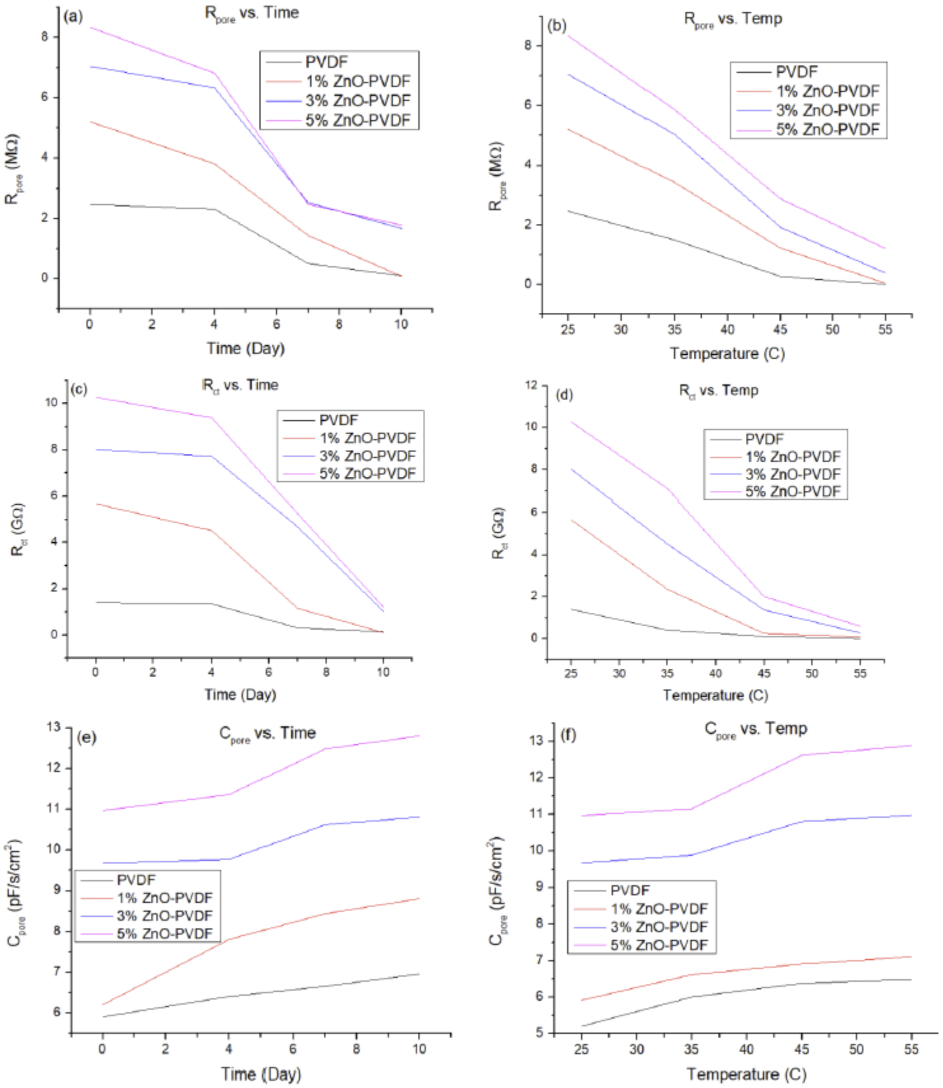

Figure 6.2: Electrochemical equivalent circuit (EEC) parameters vs. time and temperature of (a) and (b) R_{pore}, (c) and (d) R_{ct}, (e) and (f) C_{pore}, (g) and (h) R_{ct},

A comparison of the fitting parameters from temperature versus time, did not show that one approach could replicate the other. The EEC parameters against time data indicated that's the barrier resistance of the coating remained very strong upto 4 days. As the days progressed from 4 to 7, all EEC parameters values changed significantly. However, EEC parameters vs. temperature data depicts a more linear transition in EEC parameters value in thermal cyclic method. This indicated that a gradual decrease in barrier properties of the coating took place in thermal cycling method.

6.3 Mechanism Sensitivity

In the last part of this study, 3% ZnO-PVDF sensor was deployed to detect the type of corrosion (pitting or uniform) underneath the protective coating as it has a profound effect on overall performance and durability of the steel pipe. Pitting corrosion and uniform corrosion were achieved in the bare steel structure by depositing different iron oxides (Fe_3O_4, Fe_2O_3 and α-FeOOH) into it, followed by submerging it in 4.2% sea saltwater. Anodic and cathodic reaction on the α-FeOOH-covered specimen increased significantly which ultimately lead to pitting corrosion on steel substrate while other deposited samples showed uniform corrosion. All the corroded specimens were then coated with epoxy and sensor and its electrochemical properties were monitored using electrochemical impedance spectroscope (EIS) for 10 days. The data suggested that the pitting corrosion drew a lot of currents, hence its resistance was significantly low which was tacked by the sensor accurately whereas the uniformly corroded specimens showed almost identical results which portrayed the sensor's ability to detect pitting corrosion.

6.4 Summary

The overall results established the viability of the sensor textile in corrosion detection under epoxy coating and work as an early alert system. It not only performed well as a corrosion sensor but also improved the corrosion resistance performance of the coating by increasing corrosion impedance while positioning at metal coating interface. It also eliminated the limitation of being corroded by its metal counterpart while producing reliable data in harsh environment with the incorporation of ZnO nanoparticles.

6.5 Future Work

The future studies of this sensor could be making it completely wireless. For this purpose, an electric chip is required to send signal to the fiber mesh and receive it. The chip should be capable of doing a frequency sweep (10 mHz to 10 kHz) while maintaining the constant voltage (10 mV), just as an electrochemical impedance spectroscopy does it for EIS measurement. The chip should also be able to receive response form the sensor, store it and send it back to ground station through wireless communication technology. So, the chip should have a wireless transmitting device in it to send its recorded response to the ground station. Moreover, its size should be small enough to fit itself withing the two layers of the coting over steel pipe.

Another future work for this sensor could be actually setting it to a long pipe system and monitor its capability. Since the sensor worked in very small scale in the lab environment, this work could give us real-time efficiency of the sensor. Moreover, it would also tell us how many sensors are required at what distance in order to cover entire pipeline.